Faculty of Aerospace Engineering

AE3200 - Design Synthesis Exercise

July 2013

T-FLEX
Transonic Flexible Wing Experiment

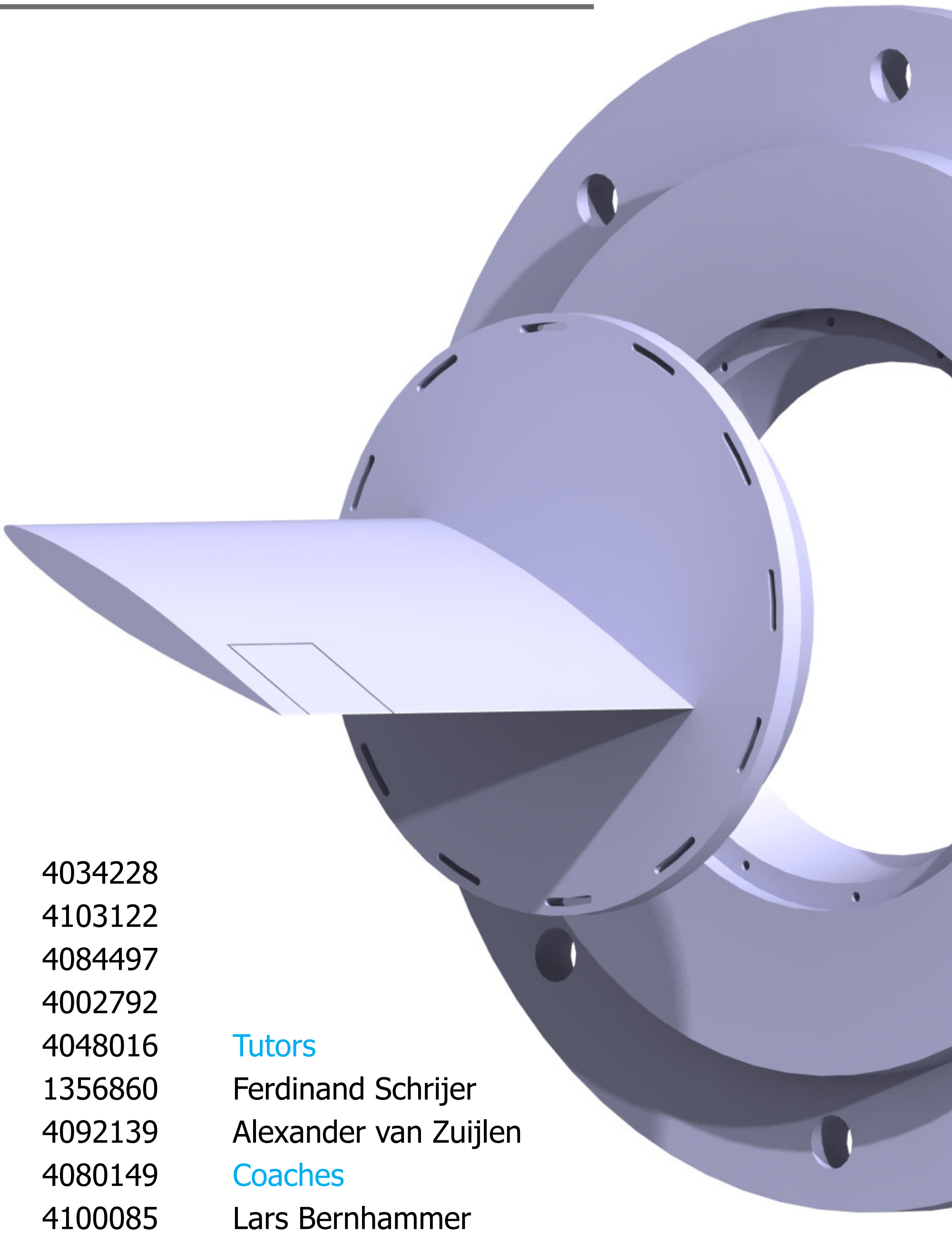

Group 13

Benjamin Caljouw	4034228		
Virgílio Gruppelaar	4103122		
Martin Hartvelt	4084497		
Max Hijne	4002792		
Raphaël Klein	4048016	Tutors	
Dirk van der Laag	1356860	Ferdinand Schrijer	
Remco van de Meerendonk	4092139	Alexander van Zuijlen	
Alexandru Popovici	4080149	Coaches	
Ștefan Scorțescu	4100085	Lars Bernhammer	
Niels Singh	4024036	Daniel Choukroun	

TUDelft

Delft University of Technology

This page is intentionally left blank.

Summary

The presented work aims at designing a transonic flexible wind tunnel experiment that provides high quality validation data for fluid-structure interaction solvers and computational fluid dynamic software validation.

Aeroelasticity, the subject at the heart of the report, is defined as the dynamic interaction between a structure and a flow field. Several phenomena result from aeroelasticity, namely control effectiveness, divergence, flutter and buffeting. Additionally, the transonic region complicates the analysis of aeroelastic phenomena. It introduces the transonic dip, an effect that drastically decreases the flutter speed as the free stream velocity increases.

The wind tunnel chosen for the experiment is the TST-27 located at the TU Delft. The wind tunnel size drove the design of the model mounted within. As the model is scaled down, several parameters come into play to maintain the measurability of the different researched phenomena: the Reynolds number, the airfoil, the model planform, the chord, the sweep, the taper, the structure and the material. A design sequence is established and followed to generate a design. The design is a hollow shell model with a skin thickness of $3mm$, no sweep and a taper ratio of one. It has a length of $230mm$, a chord of $150mm$, a NACA 64A-010 airfoil and is manufactured from chopped roving reinforced polyester.

Several options are considered for the mount, such as a clamped support, a strut support, a sting support, a wire support, a pitch and plunge apparatus mount and a nonlinear aeroelastic differential transformer mount. Following a trade-off, the clamped mount is chosen

To trigger aeroelastic phenomena, an initial excitation is needed. Therefore, an actuation system is designed. Several options are considered and traded off. The flap options is chosen as the most viable option and is detailed further. The flap is a small cut-out of the model that is actuated using a wire mechanism attached between the flap hinge and a servo motor.

The measurement techniques used are also detailed. Three main techniques are used: particle image velocimetry for flow measurements, pressure sensitive paint for airfoil pressure measurements, and videogrammetric model deformation for deformation measurements. All these techniques are used at simultaneously in the experiment.

A performance and sensitivity analysis of the experiment is conducted. In the performance analysis, the time history of the structural and aerodynamic responses are analyzed, with the predicted effects complying to the specified requirements. The fulfillment of the requirement is detailed. The sensitivity analysis details the different changes that can be made to the model and their effects. Changes of model parameters limited to 5% have been found to not have significant impact on the experiment outcome.

The total cost estimation of the experiment is also performed. It details the costs of the different parts and results in a total amount of €30,840. Finally, the risk analysis has concluded that the highest risks of the experiment relate to the mathematical design and manufacturing of the model. Future recommendations for the development of the experiment conclude this work.

Acknowledgments

The authors of this report would like to thank their tutors and coaches Dr.ir. F.F.J. Schrijer, Dr.ir. A.H. van Zuijlen, Dr. D. Choukroun and Ir. L.O. Bernhammer for their help and support throughout the Design Synthesis Exercise. Their support and feedback during the project is greatly appreciated.

The authors are also grateful to Dr.ir. E.W.M Roosenboom‘s valuable information about Pressure Sensitive Paint and Particle Image Velocimetry measurement techniques.

Dr.ir. R. de Breuker is thanked for his valuable suggestions and advice about coupling the aerodynamic and structural model.

Preface

This report is the result of ten students working on the DSE for eleven weeks. The DSE is a project which forms the last part for a student to achieve a bachelor degree in Aerospace Engineering. It allows a student at the TU Delft to demonstrate and improve the skills which they acquired during their study, such as the ability to apply their knowledge in practice, create a conceptual design and work effectively within a team.

The goal of this project is to design a transonic aeroelastic experiment which provides high quality experimental data, aimed at use for validation of numerical FSI solvers. FSI solvers are able to solve coupled problems in which aerodynamic loads cause structural deformations and structural deformations affect aerodynamic loads. An analysis by an FSI solver is computationally expensive, which means that either expensive equipment or long processing time is required. To reduce these costs, more efficient FSI solvers are developed. These, however, need to be validated. The data created by this experiment satisfies this need.

There is a demand for efficient FSI solvers, as they become increasingly more important in the development of new aircraft, allowing these aircraft to be optimised for unsteady loads, in which the interaction of structure and aerodynamics cannot be considered separate. Furthermore, these unsteady loads normally create the largest loads for which aircraft are sized. Thus, FSI solvers play an important role in optimising the performance of aircraft.

This report was preceded by a project plan, a baseline report and a midterm report, but it is created to be read independently from the previous reports. The structure is as follows: first the background of this project is explained, then the design is described which includes the choice of wind tunnel, model, mount, actuation system, measurement techniques and experiment set-up. After the design is described, the following chapters detail the procedure, performance, sensitivity, risk and costs of the experiment.

Contents

Nomenclature

Acronyms

CFD	Computational Fluid Dynamics
DLR	Deutsches Zentrum für Luft- und Raumfahrt
DNW	German-Dutch Wind Tunnels
DSE	Design Synthesis Exercise
FBS	Functional Breakdown Structure
FEM	Finite Element Method
FFD	Functional Flow Diagram
FSI	Fluid Structure Interaction
HST	High Speed Tunnel
ISSI	Innovative Scientific Solutions, Inc.
LCO_2	Liquid Carbon Dioxide
LED	Light Emitting Diode
MNS	Mission Need Statement
NACA	National Advisory Committee for Aeronautics
NASA	National Aeronautics and Space Administration
NATA	Nonlinear Aeroelastic Testbed Apparatus
PAPA	Pitch And Plunge Apparatus
PC-PSP	Polymer/Ceramic Pressure Sensitive Painting
PDV	Planar Doppler Velocimetry
PIV	Particle Image Velocimetry
PMI	Projection Moiré Interferometry
POS	Project Objective Statement
PP	Polypropylene
PSP	Pressure Sensitive Painting
PSV	Particle Shadow Velocimetry
PtTFPP	Platinum Tetra (Pentauorophenyl) Porphyrin
RDT	Requirements Discovery Table
RMS	Root Mean Square
RTM	Resin Transfer Moulding
SMART	Specific, Measurable, Achievable, Realistic and Time-bound
SNR	Signal to Noise Ratio
SRP	Self Reinforced Polypropylene
T-FLEX	Transonic Flexible Wing Experiment
TLC	Thin-layer Chromatography
TST	Transonic Tunnel
UV	Ultraviolet
VMD	Videogrammetric Model Deformation

Greek Symbols

α	Angle of attack	$[rad]$
γ	Adiabatic index	$[-]$
δ	Deflection	$[m]$
ζ	Damping coefficient	$[-]$
θ	Pitch angle	$[rad]$
Λ	Sweep angle	$[rad]$
λ	Taper ratio	$[-]$
λ_k	Structural eigenvalue	$[-]$
μ	Dynamic viscosity	$[kg/m \cdot s]$
ρ	Density	$[kg/m^3]$

σ	Normal stress	$[N/m^2]$
σ_{vm}	von Mises stress	$[N/m^2]$
σ_k	Real part of structural eigenvalue	$[-]$
σ_y	Yield stress	$[N/m^2]$
τ	Shear stress	$[N/m^2]$
ϕ	Mode shape	$[-]$
ϕ_{twist}	Angle of twist	$[rad]$
ω_θ	Uncoupled natural torsion frequency	$[rad/s]$
ω_h	Uncoupled natural bending frequency	$[rad/s]$
ω_k	Imaginary part of structural eigenvalue	$[-]$

Roman Symbols

A	Cross-sectional area	$[m^2]$
A_{amp}	Mode shape amplitude	$[-]$
A_{bl}	Relative wind tunnel area blockage	$[\%]$
A_{test}	Cross-sectional area of the test section	$[m^2]$
A_{t1}	Cross-sectional area of the first throat	$[m^2]$
A_{t2}	Cross-sectional area of the second throat	$[m^2]$
A^*	Cross-sectional area of the wind tunnel throat	$[m^2]$
a	Speed of sound	$[m/s]$
a_n	Bending eigenfrequency mode constant	$[-]$
bf	Buckling reserve factor	$[-]$
C_L	Lift coefficient	$[-]$
C_M	Pitching moment coefficient	$[-]$
C_N	Normal force coefficient	$[-]$
C_{N_α}	Normal force gradient	$[1/rad]$
C_{air}	Sutherland's constant for air	$[K]$
C_d	Drag coefficient for a two-dimensional airfoil	$[-]$
C_l	Lift coefficient for a two-dimensional airfoil	$[-]$
c	Chord length	$[m]$
$\bar{c}$	Mean aerodynamic chord	$[m]$
c_f	Flap chord length	$[m]$
c_p	Pressure coefficient	$[-]$
$c_{p,cr}$	Critical pressure coefficient	$[-]$
d	Maximum deflection fraction of length	$[-]$
E	Young's modulus	$[N/m^2]$
$[E]$, $[F]$	Final aeroelastic system coupling matrices	$[-]$
F_L	Lift force	$[N]$
f	Frequency	$[Hz]$
G	Shear modulus	$[N/m^2]$
g	Gravitational acceleration	$[m/s^2]$
g_θ	Structural damping in pitching motion	$[kg/s]$
g_h	Structural damping in plunging motion	$[kg/s]$
h	Plunge (bending) displacement	$[m]$
$\dot{h}$	Plunging (bending) velocity	$[m/s]$
$\ddot{h}$	Plunging (bending) acceleration	$[m/s^2]$
I	Area moment of inertia	$[m^4]$
I_θ	Polar moment of inertia	$[kg \cdot m^2]$
I_f	Intensity	$[cd]$
$I_{f,ref}$	Reference intensity	$[cd]$
I_{xx}	Second moment of area around the x-axis	$[m^4]$
J	Torsional rigidity of a cross-section	$[m^4]$
L	Length	$[m]$
L_f	Flap length	$[m]$
M	Mach number	$[-]$
M_∞	Free stream Mach number	$[-]$
M_{cr}	Critical Mach number	$[-]$

m	Mass	$[kg]$
$\dot{m}$	Mass flow	$[kg/s]$
p	Pressure	$[N/m^2]$
p_{ref}	Reference pressure	$[N/m^2]$
p_0	Total pressure	$[N/m^2]$
p_{103}	Static pressure upstream of the test section	$[N/m^2]$
Q_θ	Aerodynamic moment	$[N \cdot m]$
Q_h	Aerodynamic force	$[N]$
q	Non-dimensional pitch rate	$[-]$
R	Specific gas constant	$[J/kg \cdot K]$
Re	Reynolds number	$[-]$
S	Surface area	$[m^2]$
S_θ	Static mass moment	$[kg \cdot m^2]$
S_f	Flap surface area	$[m^2]$
s	Distance	$[m]$
T	Temperature	$[K]$
T_0	Total temperature	$[K]$
T_{damp}	Time until response has damped out	$[s]$
T_q	Torque	$[N \cdot m]$
T_{ref}	Reference temperature	$[K]$
t_{skin}	Skin thickness	$[m]$
V	Velocity	$[m/s]$
$V_{flutter}$	Flutter speed	$[m/s]$
w	Distributed load	$[N/m]$
x	Distance in horizontal or x-direction	$[m]$
x_{ac}	Location of aerodynamic centre	$[m]$
y	Distance in vertical or y-direction	$[m]$
$\bar{y}$	Structural state variables vector	$[-]$
Z_l	Polynomial for the contour of the bottom of the airfoil	$[m]$
Z_u	Polynomial for the contour of the top of the airfoil	$[m]$
$\bar{z}$	Aerodynamic state variables vector	$[-]$
z_{n0}	Neutral surface position	$[m]$

Chapter 1 — Introduction

At 07:02 UTC, on the 6th of March 2005, at flight level 350, a loud boom was heard on an Air Transat A310 south of Miami, Florida. It threw the flight attendants on the floor. Shortly after, the aircraft entered a Dutch roll and started gaining altitude. It took several minutes for the pilot to regain control of the aircraft. When he did, he was cleared to land. More than an hour after the loud boom was heard, the aircraft landed safely in Varadero, Cuba. The aircraft taxied to the gate, the passengers were offloaded and a visual inspection was performed on the aircraft. It revealed a startling find: the rudder had been torn off and was missing from the empennage of the A310. It would be discovered later by the investigation, that the rudder panel started fluttering and failed thereafter [74].

Flutter is one of several aeroelastic phenomena that can be encountered on modern aircraft flying in the transonic region. Aeroelasticity, defined as the interaction between aerodynamic forces and flexible structures, needs to be considered, as the structural deformation cannot be decoupled from the aerodynamics in unsteady cases. Cost being a driving factor for the aerospace industry, simulation of aeroelastic phenomena, instead of experimental validation, became a growing need. These phenomena can be simulated using Fluid-Structure Interaction (FSI) solvers. However, the complexity of solving simulations in the transonic regime is much higher than for the subsonic and the supersonic regimes due to their non-linearity. This complexity leads to several challenges, one of which is to validate the solvers used.

The goal of this report is to design an experiment that provides experimental data for the validation of FSI solvers in the transonic regime. Furthermore, this report looks into the feasibility of such an experiment in the TU Delft facilities. The experiment provides data on the dynamic response of the model that will be designed. Due to the fact that this experiment is performed in the transonic regime, shock waves are expected to be observed. Therefore, along with the data on the dynamic response of the wing, data on the motion of the shock waves over the wing is provided for. This report gives an overview of the experiment, its set-up, its strengths and its predicted shortcomings. It assesses the feasibility of such an experiment, while predicting what and how much experimental data can be provided.

This report has the following structure: Chapter 1 continues with an introduction to the field of aeroelasticity, to transonic effects, to FSI solvers, to the validation data, to the design approach and to the requirements. Chapter 2 present the different wind tunnel options before detailing the chosen wind tunnel and the calculation of the Reynolds number. Chapter 3 details the model design. First the airfoil is chosen then the model planform, followed by the structure and the materials. The chapter ends with the presentation of the aeroelastic model and the final design. Chapter 4 presents the different mount options, their trade-off and finally the detailed mount design. Chapter 5 demonstrates the different possible actuation systems before selecting one actuation method and detailing it. In Chapter 6, different measurement techniques are outlined. They are followed by a detailed description of the three chosen measurement techniques and a section on how to combine them. Chapter 7 presents the model production followed by the measurement campaign. Chapter 8 elaborates on the sensitivity and performance analysis of both the model and the measurement devices. In Chapter 9, the costs of the experiment are outlined. The risks are then detailed for the model, the aeroelastic model, the mount, the actuation and the measurement techniques. Finally, Chapter 10 concludes this report and presents final recommendations for further research.

1.1 Aeroelasticity

Aeroelasticity is a wide field of study that outlines the interaction of a structure with a flow field. Aeroelastic phenomena are at the centre of forces characteristic to the aerodynamic flows, the elastic structures and the inertial properties. The field of aeroelasticity is highly relevant to aerospace engineering due of the tendency of modern aircraft to be more and more slender and lightweight. These two tendencies combine to render aircraft structures flexible. Several phenomena can result from this interaction of aerodynamics, elasticity and inertia. Understanding them is essential for the design of a flexible wing, that allows studying them. In the following, a short overview of aeroelastic phenomena is given, based on [6].

First, static aeroelastic phenomena are explained, namely control effectiveness and divergence. Control effectiveness is the influence of elastic deformations of the structure on the controllability of an aircraft. This influence can result in control system reversal - a condition occurring at the control reversal speed, at which the intended effects of displacing a component of the control system are cancelled by elastic deformations.

The principle of divergence lays in the increase in angle of attack, lift force and pitch angle caused by a perturbation increase in angle of attack. The resistance to the increase in lift force is expressed in the torsional spring stiffness. The stiffness being constant, as the aerodynamic forces increase with increase in dynamic pressure, there is a speed where the aerodynamic moment balances the spring moment. This point is called the divergence speed. Beyond this speed, the pitch angle will increase without bound in response to perturbations. However, as explained in Section 1.2, since the transonic regime introduces particular computational difficulties for the dynamic phenomena only, and since this experiment will focus on the transonic regime, static phenomena will not be studied.

Second, dynamic aeroelastic phenomena are explained, namely dynamic response, flutter and buffeting. Dynamic response phenomena display cyclical influence of aerodynamic forces on structural deformations and consequently of structural deformations on aerodynamic forces. In flight, dynamic response can occur from the translational or rotational motion of the aircraft as a rigid body, but more interestingly, from rapidly applied external forces such as gusts. They can be studied after a known forced excitation is given to a certain structure.

Flutter is defined as an unstable dynamic response occurring in an aircraft in flight, where the elasticity of the structure plays an essential part. In simple terms, flutter is caused by the pitch and plunge motion of the structure. The speed at which flutter occurs is called flutter speed. At this speed, the structural damping is insufficient to damp out the motions which are increasing due to aerodynamic energy being added to the structure. This vibration can cause structural failure. However, structural failure is not desirable in an experiment if repeatability and cost effectiveness are expected. Therefore, a study of flutter is necessary to prevent such failure.

Buffeting is defined in [6] as transient vibrations of aircraft structural components due to aerodynamic impulses produced by the wake behind wings, nacelles, fuselage pods, or other components of the aircraft. The study of buffeting is therefore an implicit part of the study of dynamic responses. However, this phenomenon is different in that it is focused on the characteristics of the flows generated by some aircraft parts affecting other aircraft parts. These flows generate forces that are not affected by the motion of the former parts and would be present even if the structure were infinitely rigid.

The design of modern transonic aircraft relies heavily on the computational modelling of the aerodynamic and structural behaviour, as well as the behaviour resulting from their interactions, namely aeroelasticity. Studying the phenomena described above is necessary for the validation of such computational models. However, the transonic regime introduces some particularities to these phenomena. These particularities are explained in the following section.

1.2 Transonic Effects

Two major effects occur in the transonic regime. These are the shock waves and the transonic dip. These effects are briefly explained in this section.

In the transonic regime, shock waves occur. Their appearances over an airfoil is driven by the shape

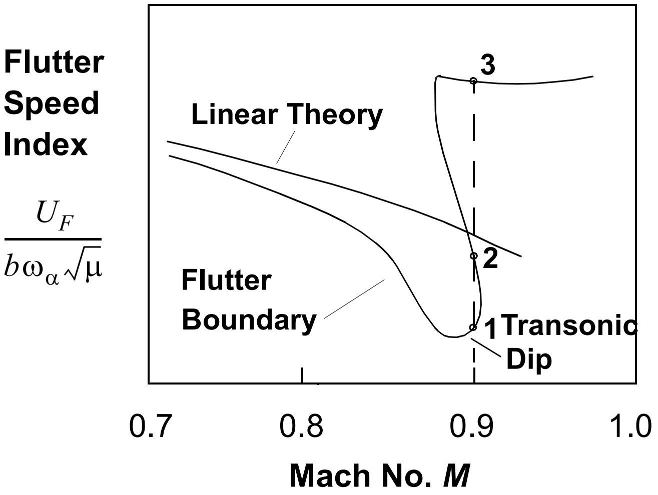

Figure 1.1: Illustration of transonic dip [5]

of the airfoil, the velocity of the free-stream and the angle of attack. For a certain free-stream velocity, there exists a location on the airfoil where sonic conditions are achieved. When sonic conditions are attained, the free-stream Mach number is called the critical Mach number. When increasing the free-stream velocity, a supersonic bubble appears over the airfoil. This region grows as the free-stream Mach Number increases. As this region appears, a weak shock wave is created. Similarly, the more the free-stream velocity is increased, the stronger the shock wave becomes.

Across the location of the shock wave, the density, the pressure and the temperature of the flow change abruptly. This affects the loading of the wing which in turn induces twist into the wing. This twist changes the location of the shock wave which then again affects the loading on the wing. This cycle can continue infinitely as long as the shock is sufficiently strong.

The transonic dip is a second important phenomenon that results from the transonic regime. It is associated with the decrease of the flutter speed as the free-stream velocity approaches Mach 1. The transonic dip cannot be predicted by steady aerodynamics models. The reason is due to the fact that steady aerodynamics do not take into account the shock wave motion, the flow separation, the vorticity dynamics, the viscosity and the change in aerodynamic centre. Figure 1.1 clearly shows the difference between linear models (steady aerodynamics model) and experimental data. It can be seen that the transonic dip is not predicted by the linear theory. In the figure, the flutter index on the flutter boundary at a given Mach number represents the velocity of the fluid at which an airfoil of unit mass ratio, semi-chord length, and uncoupled natural frequency in pitch, flutters. The frequency at which it flutters is called the flutter frequency.

However, new models have been developed to predict the transonic dip. Figure 1.2 shows different simulations of the transonic dip using three different methods. Note that in Figure 1.2 the flutter index is referred to with ”fi”. The first method, which is illustrated by line A, is a method which assumes potential flow about infinitesimal thin lifting surfaces. This method does not account for viscous effects or the impact of a transonic flow field on the geometry of the airfoil. This method only properly simulates the subsonic part of the flutter boundary. When reaching the transonic regime, this method becomes inaccurate. The second method, illustrated by line B, is based on Euler or potential equations with the assumption that all viscous effects are neglected. Using this method, the decreasing side of the transonic dip can be simulated. However, this method does not allow the simulation of the increasing side of the flutter boundary. The third method is based on the full Euler or potential equations. The last method simulates the transonic dip, accurately taking into account the viscous and inviscid interaction.

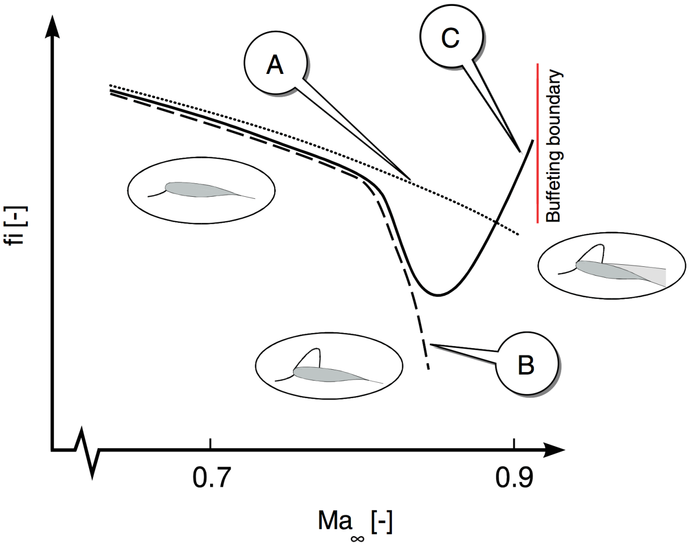

Figure 1.2: Transonic dip simulations [19]

1.3 FSI Solvers

It was shown in the previous section that it is possible to accurately predict and simulate the flutter boundary. However, this simulation needs to be linked to the structural simulation to obtain a complete FSI simulation. In this section, some of the issues that FSI analysts have encountered are mentioned. These issues are the fluid-structure coupling, the time synchronisation and the code validation.

Fluid-structure coupling is one of the challenges that researchers are facing. Implementing a correct fluid-structure boundary condition is of paramount importance to achieve stability in the calculations. Spatial and time synchronisation requirements must be met. In order to avoid mistakes, separate software modules are usually used to discretise and time march the fluid and the structure equations as shown in Figure 1.3. Since aeroelasticity codes use loosely coupled schemes, coupling is then accomplished in an approximate manner. This method, however simple, can lead to local violations of conservation laws at the fluid-structure boundary. For transonic flutter, which is a highly non-linear problem, the coupling becomes harder and convergence can become an issue. Because there is a need for strict boundary conditions, the experiment that is mapped out in this report has to provide very accurate boundary data. The boundary in the case of this experiment is the airfoil surface. If accurate data is provided for this region, then the validation process becomes easier.

For FSI validation, it is also important to know how the shock wave behaves. This has to be provided by pressure distribution on the airfoil. An example is shown in Figure 1.4. The figure clearly shows the normal meshing in the top figure around an airfoil. However, in the transonic regime, it is important to know what happens around a shock wave. Knowing the shock wave location, it is possible to refine the mesh at that location (see bottom picture). In order to obtain an appropriate model, it is therefore important to provide accurate data for the location of the shock wave.

The time synchronisation is the biggest and most important challenge encountered so far. This is due to the fact that a badly coupled aeroelastic code can be made to converge to a wrong solution. Furthermore, introducing a time delay in the equation, as is done for bending-torsion problems, increases the number of solutions from four complex conjugates roots to an infinite number of complex roots which has a destabilising effect on the solution.

The validation challenge is the challenge that the experiment explained in this report aims at tackling.

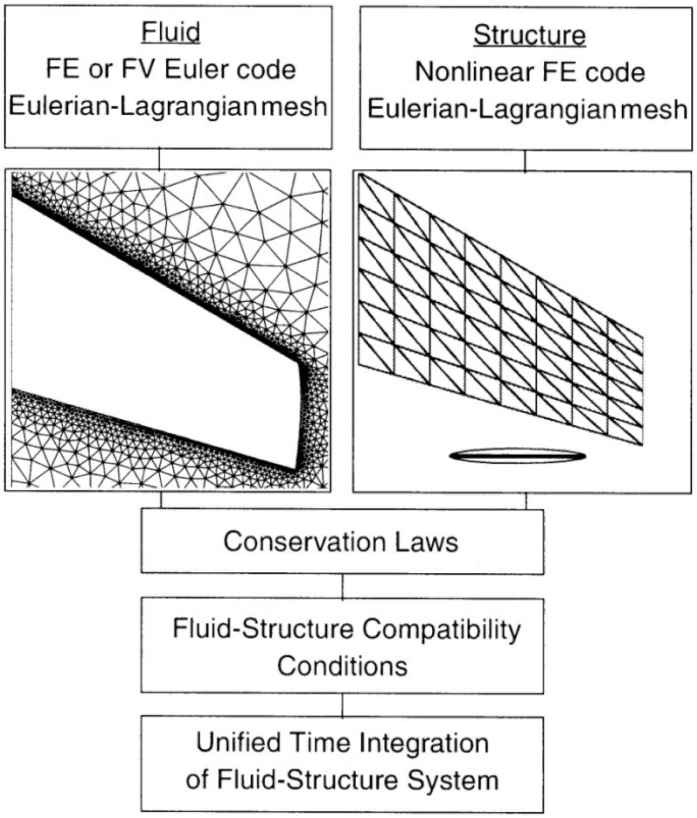

Figure 1.3: Method used to solve FSI problems [5]

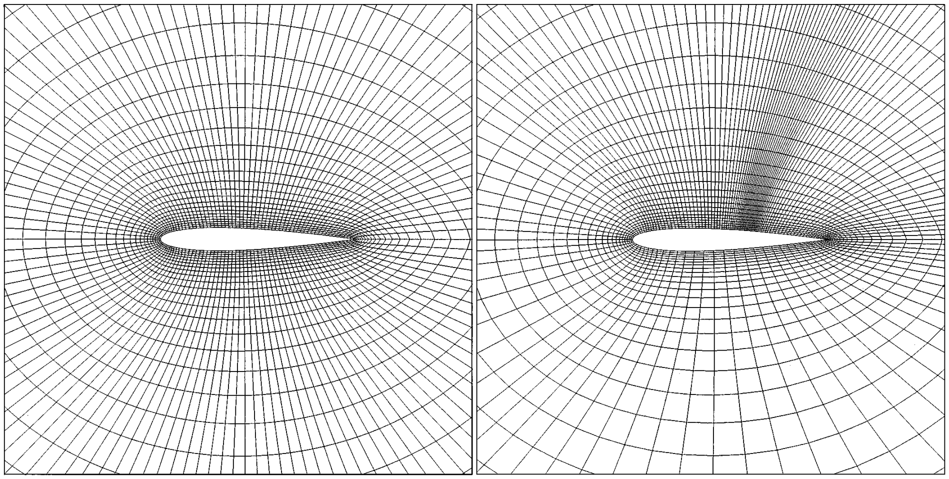

Figure 1.4: Meshing grid around an airfoil [12]

1.4 Validation Data

Obtaining high quality validation data for numerical FSI solvers poses a number of significant challenges for the experiment design. In static experiments, the model does not deform in time and measurements can be taken after a certain settling period when it is certain that the measured values reached a steady state. However, in dynamic experiments the aerodynamic loading influences the structural deformation, which in turn influences the aerodynamic loading. Therefore, for validation of the FSI solvers, all measured parameters need to be time-varying. Furthermore, the need for time-dependent validation data stems from the fact that the boundary conditions will change continuously on the surface of the model during unsteady phenomena, like buffeting and shock wave motion.

Ideally, a complete aeroelastic validation set contains the following measurement data [18]:

- Unsteady pressure measurement on the model surface
- Deformation measurement of the model
- Flow visualization measurement in the wind tunnel
- Load measurement on the model
- High quality definition of the geometry of the model

The validation data which must be provided by the experiment is divided in two different levels of importance. Level zero validation data is the most important level. For the experiment to be successful, all the validation data from level zero must be provided. Level one validation data contains data that is useful for validation, but is not necessarily required.

1.4.1 Level Zero Validation Data

As mentioned above, the level zero validation data contains the minimum data that is required for the experiment. The level zero validation data contains wind tunnel boundary conditions, pressure on the model surface, deformation of the model and data about the wind tunnel model geometry and characteristics.

Wind Tunnel Boundary Conditions To provide for the wind tunnel boundary conditions, the entire wind tunnel geometry is provided to the FSI solver. Additionally, the conditions in the settling chamber can be provided accurately. This is enough for the FSI solver to determine the conditions within the entire wind tunnel.

Pressure on the Model Surface To validate the Computational Fluid Dynamics (CFD) side of the FSI solvers, the pressure of the air on the surface of the model can be used to reconstruct the pressure distribution of the flow around the model. Furthermore, the pressure on the model surface can be used to locate laminar to turbulent transition and shock wave position. Pressure on the surface of the model is also the main source of finding aerodynamic loads.

Deformation of the Model The deformation of the model can be used to validate the structural side of the FSI solver. The deformation of the model can also be used to determine the natural mode of the structure, which can be used as a reference for the measurement devices.

Model Geometry and Characteristics To model the experiment in the FSI solver, the geometry and the characteristics of the model must be provided. This data set consists of surface roughness, material properties, model dimensions and position of the measurement divices.

1.4.2 Level One Validation Data

Level one validation data contains data that is useful for validation, but is not necessarily required. Once the level zero validation data is obtained, the experiment has enough validation data to be successful. However, to improve the quality of the set of validation data, the level one validation data can be used. The level one validation data contains model-mount interaction boundary condition, the pressure in the wind tunnel test section and the flow velocity in the test section.

Model-Mount Interaction Boundary Condition The shape of the mount has an influence on the flow around the model. To know the influence of the mount on the flow around the model, the boundary conditions in this area must be known. Knowledge of these boundary conditions can be used to determine whether data near the root of the model can be used for validation, since the mount could disturb the flow too much.

Pressure around the Model The pressure of the air around the model can be used to detect the shock wave position and strength. The position and strength of the shock wave can be found from the flow velocity measurements. However, to obtain the pressure from the flow velocity, the density must be known at each point. Since the density will change significantly near the shock wave due to compressibility effects, the shock wave position and strength can be found.

Flow Velocity in the Test Section Another means to validate the CFD side of the FSI solvers is to measure the flow velocity in the test section. The flow velocity in the test section provides additional data on the velocity field. Also, with flow visualization, the position of the shock wave can be validated.

1.5 Design Approach

The method followed throughout the report to establish a final design of the experiment is presented in this section. It is presented in the form of a N2 chart shown in Figure 1.5. The chart is constructed using eight different levels. These levels constitute the building blocks of the experiment design. Most of these basic buildings block are related to the others in some way. This outlines the fact that the design of the experiment is an iterative process.

The first building block contains the ”Aeroelastic Phenomena”. This block has one main output: the ”Desired Effects”. Depending on the aeroelastic phenomenon that needs to be studied, the design is altered. This affects the model, the mount, the measurement techniques and the actuation system. The only input is the mission goal of the project.

The second building block is the ”Wind Tunnel”. The wind tunnel has several outputs used for the different levels of the design. The most important output is the range of natural frequencies (f) obtainable from the wind tunnel, considering the impact of the test section on the model structural vibrations. These frequencies affect the entire model design. Additional outputs are the Reynolds number, the blockage area requirement, the wind tunnel width, the range of Mach numbers, the temperature of the air (T), the density of the air (ρ_{air}), the allowable size of the mount and the allowable size of the actuation system. The shape of the mount, the type of PIV particles and the type of actuator used also have an impact on the wind tunnel.

The third building block is the ”Wing planform”. The wing planform is affected by the requirements and several inputs like the natural frequency, the Reynolds number, the blockage area, the width of the wind tunnel and the Mach number. From the wing planform, it is possible to obtain an updated frequency, the chord length (c), the airfoil choice, the length (L), the sweep and the taper of the model. The wing planform also has inputs from the next building blocks such as the structure, the updated frequency and the size of the actuator.

The fourth building block is the ”Aerodynamic Loads”. They are obtained from the aeroelastic code developed throughout the project. The input for the aerodynamic loads are the natural frequencies, the chord length, the airfoil characteristics (aerodynamic centre and C_{N_α} as a function of the Mach

Mission Goal	Requirements	Requirements		Requirements		Requirements	
Aeroelastic Pheomena	Desired Effects			Desired Effects	Desired Effects	Desired Effects	Desired Effects
	Wind Tunnel	f, Re, Blockage, WT Width, M	f, T, ρ_{air}	f, Blockage	f, Blockage, Size of Mount		Size of Actuator
		Wing Planform	f, c, Airfoil, L, Sweep, Taper	f, c, L, Sweep, Taper	f, c, L	f, c, L, Sweep, Taper	c, L
		f	**Aerodynamic Loads**	f, Loads, Twist, Flutter Limit, Damping	f, Loads	f	Loads
		f, Structure	f, Twist, Flutter Limit, Damping, Shear Centre, I, m	**Model Design**	f, A, Structure, I, E, ρ	f, A, Structure, Material	A, Structure, I
	Shape of Mount			f, I, E, ρ	**Mount**	f, Type of Mount	Mount Shape
	Type of PIV Particles	f	f, Skin Friction Coefficient	f	f, Shape of Mount	**Measurement Techniques**	MT Dimension, MT Location
	Type of Actuator	Size of Actuator	Shape of Actuator	Size of Actuator	Size of Actuator	Size of Actuator	**Actuation system**

Figure 1.5: Design approach N2 chart

number). The outputs are of the loads, the natural frequency, the twist, the flutter speed limit and the damping.

The fifth building block is the "Model Design". The model design is closely related to the aerodynamic loads and the wing planform blocks. These three blocks encounter many more iterations than the rest of the blocks. The inputs for the model design are the desired effects, the natural frequency, the blockage area, the length of the model, the taper, the sweep angle, the chord length, the aerodynamic loads, the twist angle, the flutter limit and the damping coefficient. Its outputs are the natural frequency, the cross-sectional area (A), the internal structure of the model, the mass moment of inertia (I), Young's modulus (E), and the material density (ρ). On the other hand, the feedback inputs for the model design mostly come from the mount with the frequency, the length of the model, Young's modulus, the moment of inertia and the density of the material.

The sixth building block is the "Mount". The inputs for the mount are all the outputs from the model design except for the material. The mount has as outputs the type of mount, the shape, the natural frequency, the mass moment of inertia, Young's modulus and the density of the material. Through feedback loops, the mount is also influenced by the size of the actuator and the natural frequency required by the measurement techniques.

The seventh building block is the "Measurement Techniques". The Measurement Techniques, in the figure referred to with "MT", inputs are the natural frequency, the type of mount, the structure, the material and the cross sectional area. Additionally, the outputs from the wing planform are also required to properly estimate the placement of each of the devices. The outputs of the measurement techniques are their placement and their dimensions. These have an influence on the actuation system and its positioning within the model.

The eighth basic building block is the "Actuation System." The inputs for the actuation system are the parameters related to the spacing within the model, the loads and the wind tunnel space allowance. The actuator has some impact on all previous building blocks through the feedback loop affected by its size on the model.

1.6 Experiment Requirements

The designed experiment must meet a defined set of requirements. A preliminary set is defined using the Functional Flow Diagram (FFD) and the Functional Breakdown Structure (FBS). The FFD and FBS are presented in Appendix C and Appendix D respectively. All requirements have to be made Specific, Measurable, Achievable, Realistic and Time-bound (SMART). Additionally, new requirements are continuously added throughout the design page, based on new information and insights, just as some may be removed if they are not relevant anymore. The design of the final set is an iterative process during the entire experiment design. The influences of the requirements on the project are illustrated in Figure 1.6. Finally, the success of the project is evaluated by testing the compliance of the experiment with the requirements, which is presented in Section 8.3.

The requirements are divided into four groups: Data measurement (starting with D), Experiment (starting with E), Model (starting with M) and Resources (starting with R). The data measurement, experimental and model groups contain technical requirements, whereas the resources group contains the constraints. This grouping is illustrated in Figure 1.7. All requirements are given an identification, based on the grouping and the level of specification. The letter of the Id. refers to the group, whereas the numbers specify the requirement. For example, D1.1.4 means the requirement describes a part of the data measurement and is the fourth part of the specification of D1.1, which of course is again a specification of D1. Some requirements are marked with a "*d*." This attribution means that the requirement and its specifications are driving requirements. The Requirements Discovery Table (RDT) is shown in Table 1.1.

Requirements on Data Measurement The requirements on data measurement are split into D1, D2 and D3, which represent the data accuracy, what data is to be measured and the processing of the data respectively.

Table 1.1: Requirements compliance table

Id.	*d*	*Requirement*
D		**Requirements pertaining to the data measurement**
D1		The experiment shall provide accurate data on pressure and model deformation.
D1.1	d	The obtained data must have a sufficient resolution for validation of the desired phenomena.
D1.1.1		The measured pressure data must have a minimum sampling resolution of 14 dots per cm.
D1.1.2		The pressure measurements must have a temporal resolution of at least 10 times the oscillation frequency.
D1.1.3		The deformation measurements must have a temporal resolution of at least 10 times the oscillation frequency.
D1.1.4		The pressure measurements must have a spatial resolution of at most $0.75mm$.
D1.1.5		The deformation measurements must have a spatial resolution of at most $4mm$.
D1.2	d	The employed measurement techniques must have a low systematic error.
D1.2.1		The measurement bias of the pressure data based on amplitude must be less than $230Pa$.
D1.2.2		The measurement bias of the deformation data based on amplitude must be less than $0.05mm$.
D1.4		The data must be processed accurately.
D1.4.1		The dataset must be processed with a confidence interval of 95%.
D1.4.2		The processed experimental data must have a SNR of at least $40dB$.
D1.5		The employed measurement techniques must have a high enough sensitivity.
D1.5.1		The pressure must be measured with a sensitivity of at least $230Pa$.
D1.5.2		The deformation must be measured with a sensitivity of at least $0.05mm$.
D2	d	The experiment shall provide relevant measurement data and boundary conditions for numeric FSI solvers.
D2.2		The experiment must measure the deformation of the model.
D2.2.1		The experiment must measure the twist of the model.
D2.2.2		The experiment must measure the model deflection.
D2.3		The experiment must measure the frequency of at least the first bending mode and the first torsion mode of the structure.
D2.4		The experiment must measure the position of shock waves along the chord and in span-wise directions.
D2.5		The experiment must measure the pressure distribution along the chord and in span-wise directions.
D2.6		The boundary conditions provided by the experiment must be reproducible in computational models.
D2.7		The running time of the experiment must allow for the completion of an entire measurement set.
D3		The measured data must be provided in a format that allows for its input into computational solvers.
E		**Requirements pertaining to the experiment**
E1		Free stream flow conditions (pressure, temperature, density) must be constant during the experiment.
E1.1		In case of required repeatability, the deformation and a boundary condition at a reference point may not differ by more than 1%.
E1.2		The flow in the wind tunnel test section must be steady.
E2	d	The experiment must take place in transonic conditions, at a Mach number between 0.5 and 1.
E3	d	The experiment must take place at a Reynolds number of at least 10^6.
E5		The experiment description must be clear, correct and follow a logical sequence.
E5.1		The parameters in the data set must be clearly labeled and explained.
E5.2		Any possible source of error must be documented.
E6	d	The experiment must provide data that is relevant for transonic transport aircraft.
M		**Requirements pertaining to the model**
M2	d	The model and the mount must fit in the test section of the selected wind tunnel.
M3		The surface roughness of the finished model must be at the most $0.20\mu m$.
M4		The manufactured model must have tolerances no larger than $0.1mm$.
M5		The area blockage in the wind tunnel due to the model may not be more than 5% of the tunnel section concerned.
M6		The amplitude of the models tip deflection must have a maximum of 10% of the model length ($23mm$).
M7		The model must have a buckling factor of at least 2.
R		**Constraints and requirements on resources**
R1		The safety of all personnel must be guaranteed during the experiment.
R2	d	The wind tunnel integrity must be maintained.
R3	d	The budget for the experiment shall not exceed €50,000.
R4	d	The experiment must be performed at the TU Delft.

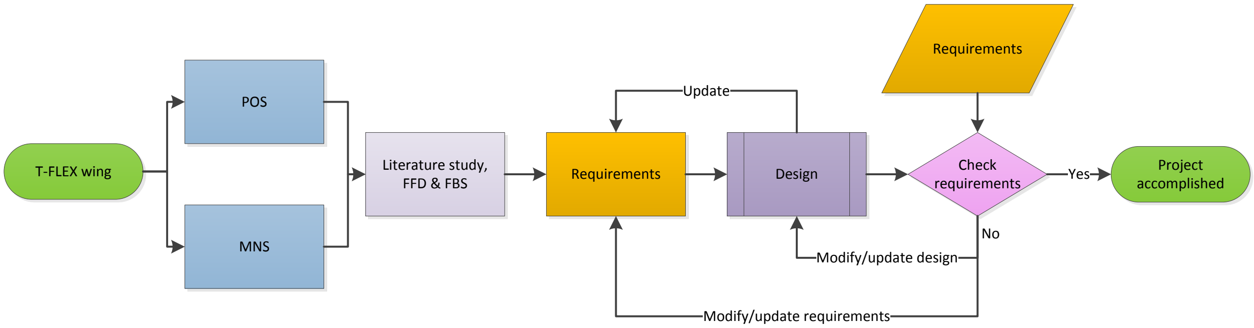

Figure 1.6: Influence of requirements on project

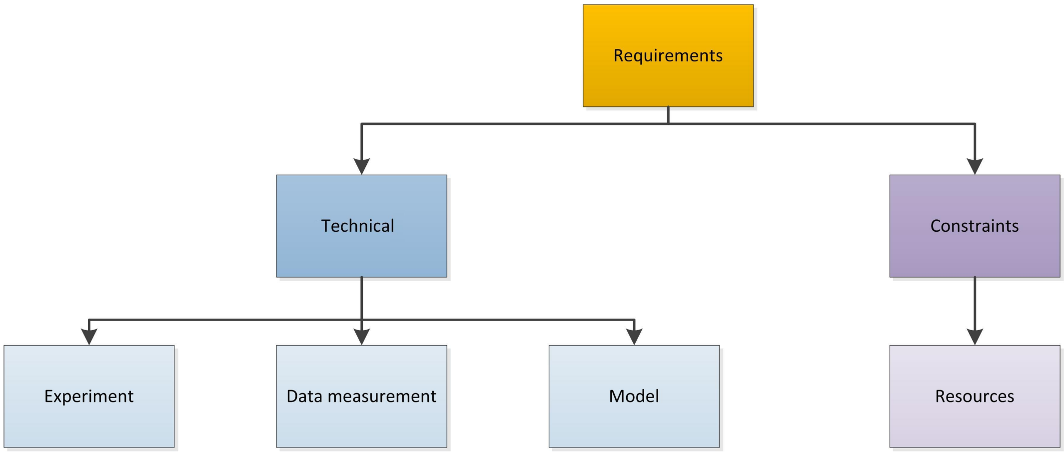

Figure 1.7: Requirement groups

The accuracy is introduced to describe the measurement uncertainty and contains the sampling, temporal and spatial resolutions (D1.1), the systematic error (D1.2) and the random error in the data processing (D1.4). The allowed measurement uncertainty follows from typical CFD code errors. CFD codes are usually designed to compute at a spatial resolution of 0.5% of the chord length and modelling errors of FSI-solvers, which are typically between 1% and 5% of the data values. For separate requirements an error of 1% is used for the FSI solver.

For the deformation measurements, convenient points are chosen to perform measurements, so no sampling resolution is defined. However, pressure data is required over the entire flow field. The sampling is based on the CFD code accuracy. A data point is needed on every 0.5% of the chord length. The spatial resolution is in this case directly related to this same accuracy. The spatial resolution for the deformation measurement may be larger to stay within the 1% accuracy. The average value of a data point may not vary more than 1% of the deflection at the edge of the sample. The minimum deflection used for this requirement is the deflection in the first bending mode at half the model span. The half span point is chosen, because the deformation closer to the wind tunnel wall at the root is very small. Additionally, interference might occur between the flow, the model and the mount closer to the root.

The systematic error consists of a deviation in the mean signal, as well as the systematic error in the amplitude of the signal. Since the data is used for validation, the mean error is not relevant, assuming the error is small. The measurement bias based on the amplitude of the data signal must be smaller than the typical modelling errors for CFD codes and FSI solvers.

During the entire experiment and the processing of the data, noise is added. The noise may not influence the signal by more than 1% of its amplitude, so the signal to noise ratio (SNR) must be more than $10\log(100/1)^2 = 40dB$. During the processing of the data, faulty data is filtered. To remove this data, a confidence interval is set at 95%. This value is set, as it is widely used in data processing of experiments.

Finally, the sensitivity of the measurement techniques used is set to be within 1% of the expected data. For pressure measurements this value becomes 1% of the difference between the static pressure at $M = 0.7$ in the wind tunnel and $M = 1$ over the model at its critical angle of attack. For the deformation, this percentage is used over the maximum deflection of the model at half its span when in its first bending mode.

The data to be measured is described in D2.2 up to D2.7. Since the data must provide relevant measurement data for an FSI solver, aeroelastic behaviour needs to be measured. Therefore, the deflection and twist of the model are required in an oscillation of at least of the first pitching and plunging motion eigenfrequencies. Additionally, the shock wave motion is measured, since knowledge on its position is required. To get information on the strength of the shock wave, the pressure distribution over the model is required as well.

Requirements on Experiment The requirements pertaining to the experiment describe what is represented by the experiment and the required flow conditions. The experiment's scope is to provide data, relevant for transonic transport aircraft. From this, the required Mach and Reynolds numbers are defined [77]. The flow conditions also describe the required quality in case of repeatability. Finally the experiment handling and quality is defined.

Requirements on Model The requirements in the model group give structural constraints. They describe the allowed surface roughness [78] and manufacturing tolerances [44] as well as the maximum tip deflection of the model. This deflection is based on the assumption that when the deflection is smaller than 10% of the model length, the lift distribution can still be modelled upward in the original coordinate system, not rotating with the model. Additionally, shortening behaviour of the model does not have to be taken into account.

Requirements on Resources Finally, the requirements on the resources are given constraints for the project. The budget for the experiment and the location are dictated by the assignment [77]. Furthermore, the safety of all personnel and the integrity of the wind tunnel have to be guaranteed.

Chapter 2 — Wind Tunnel

The first step in the design process of the experiment is to choose the wind tunnel in which the experiment is performed. The decision on the wind tunnel dictates the Reynolds number range, the model size, the measurement technique possibilities and the actuation allowed. Some requirements were already established for the choice of the wind tunnel. The wind tunnel has to operate in the transonic regime to perform the experiment. Another requirement indirectly linked to the wind tunnel is the budget. The price of operation of the wind tunnel must remain the lowest possible to allow for other expenses.

2.1 Wind Tunnel Choice

An important first step is to establish a base of background knowledge of transonic wind tunnels. They are a special class of wind tunnels due to the nature of the flow. Just below Mach 1 (between Mach 0.7 and Mach 1) in a wind tunnel, introducing a model in the flow leads to the blockage of this flow. The model can therefore act as a throat, effectively choking the flow. To avoid this problem, wind tunnels have slotted walls. These are small openings in the walls around the test section that can artificially increase the area of the test section. This way, introducing the model does not block the flow.

A major disadvantage stems from using slotted walls. The boundary conditions of the wind tunnels become hard to determine. This means that it is hard to validate any numerical code using data produced in an experiment set-up that uses slotted walls. This becomes a problem for this project as obtaining validation data is the main goal stemming from the mission statement. It is therefore needed to find an experimental set-up where there is no need for the slotted walls, while still obtaining transonic behaviour.

There are numerous wind tunnels around the world that can perform in the transonic regime. Some have much larger cross sections than others, such as the one operated by NASA Ames in the United States. This wind tunnel has a cross section of $3.35m$ by $3.35m$ and can reach Reynolds number of 32 million per meter. However, using such a wind tunnel is too costly. Another transonic wind tunnel located in Cologne can reach a Reynolds number of 50 million per meter by using a cryogenically cooled flow.

Due to the budget restrictions, only wind tunnels in the Netherlands are looked at. There are two facilities that can be used for transonic measurements: the DNW-HST wind tunnel in Amsterdam and the TST-27 located in Delft. The different important parameters of the two wind tunnels are presented in Table 2.1 and they are presented hereon.

As can be seen, the DNW-HST wind tunnel has more advantages than the TST-27. The Reynolds

Table 2.1: Wind tunnel description

	TST-27	**DNW-HST**
Location	Delft	Amsterdam
Speed range (M) [-]	0.5-2.8	0.15-1.35
Reynolds number 10^6	38-130 [1/m]	9
Height [m]	0.27	1.8
Width [m]	0.28	2
Type	Blow down	Closed
Price [euro]	Free	€50,000+

number in the DNW-HST can reach much higher values. The test section allows for larger models, increasing the fidelity to real life aircraft and decreasing the complexity of the model due to downsizing. Finally, the type of wind tunnel leads to a higher efficiency in DNW-HST, as an experiment can be run non-stop, which is not the case in the TST-27. In the TST-27, the time available for experiment per day is limited to five minutes.

However, several issues also arise with the use of the DNW-HST in Amsterdam. The first one is the costs. It is assumed that the costs at the DNW-HST is higher than the allowed budget. Furthermore, this project is a feasibility study on whether a FSI solver validation experiment can be made in a Delft facility (which can only be the TST-27). Therefore the experiment is performed in the TU Delft facilities.

2.2 TST-27 Description

As mentioned in the previous section, the wind tunnel that is chosen for the experiment is the TST-27 located in Delft. In this section, some of its aspects are described.

The TST-27 can operate in the subsonic, the transonic and the supersonic regimes. For transonic experiments in the TST-27, a set-up of the wind tunnel is used in which the flow is accelerated to transonic speeds at the first throat, which then arrives in the test section at a slightly lower speed. In order to prevent the propagation of disturbances upstream of the flow, a second throat is placed downstream of the test section, in which the Mach number is one. In this way, the test section is protected from any unwanted disturbances that occur downstream of the second throat. In addition, having a second throat enables an easier and more precise manipulation of the Mach number than varying the area of the first throat. The reason for this is that the blockage of the second throat can be altered by the use of eight rods for which the part that is submerged in the flow is variable. In addition, a small wing model in the second throat is used for the fine tuning of the area and therefore of the Mach number in the test section.

Figure 2.1 shows a schematic view of the TST-27 wind tunnel. In Figure 2.2, the area control system of the second throat, with the eight rods and the wing are shown. In order to perform the experiment at transonic conditions, the Mach number in the test section needs to be controlled.

As stated before, in the TST-27, Mach number control is realised by altering the area of the second throat of the wind tunnel. However, the exact ratio $\frac{A_{test}}{A_{t2}} = \frac{A_{test}}{A^*}$ is not known. That is, instead of having knowledge about the exact area of the second throat, a static pressure port, called p_{103} is placed upstream of the test section, where no reflected pressure fronts from the model can interfere with the walls of the wind tunnel where the static pressure port is positioned. The ratio $\frac{p_{103}}{p_0}$ has been obtained for a wide range of Mach numbers in the test section. Therefore, the basic procedure for obtaining a desired Mach number is to alter the area of the second throat, until the already obtained value for the $\frac{p_{103}}{p_0}$ ratio corresponds to the desired Mach number in the test section.[76]

In order to achieve a relatively high Mach number in the test section area, the test section and the second throat areas have similar values. However, once a model is placed in the test section, its frontal area causes a blockage of the test section area, reducing the effective test section area. Even though the static pressure ratio is set for a certain value of the Mach number as described above, the placing of the model influences the flow in the test section. That is, the Mach number has a larger value. Since slotted walls have been deemed unfavourable for the purpose of validation, and solid walls are used, a limitation on the model frontal area is imposed to prevent wall interference. In order to avoid this, the design is based on a maximum of 5% area blockage and a Mach number of 0.7.

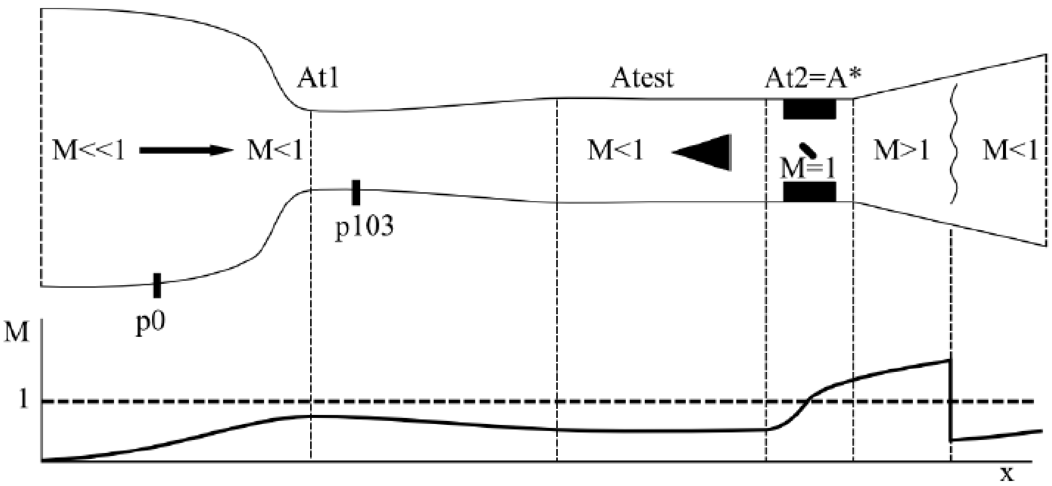

Figure 2.1: TST-27 Wind Tunnel facilitiy at the TU Delft [76]

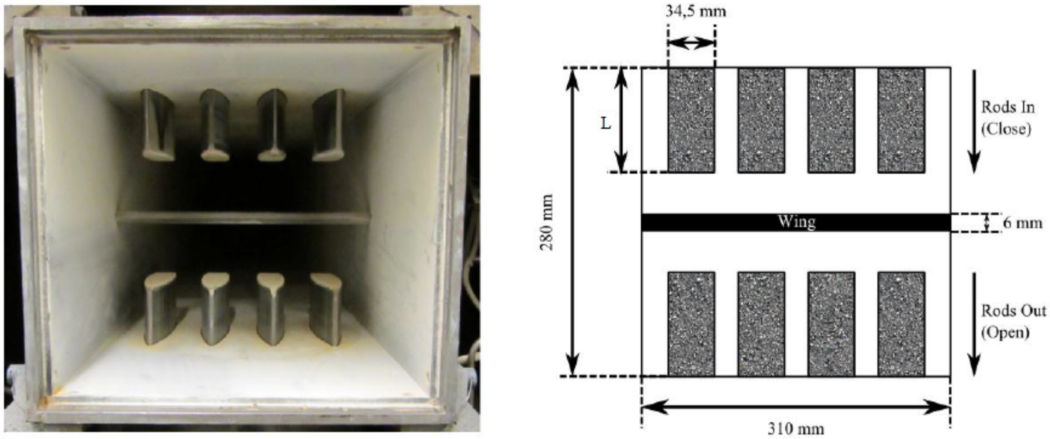

Figure 2.2: Area Control System in the Second Throat [76]

2.3 Reynolds Number Calculation

The requirements dictate a minimum Reynolds number of 10^6 (requirement E3) and a Mach number between 0.5 and 1 (requirement E2). The tunnel operates in this Mach region, at a Mach number of $M = 0.7$, a total temperature of $T_0 = 285K$ and a mass flow of $\dot{m} = 40kg/s$. Equation 2.1 shows the equation used to determine the Reynolds number from these wind tunnel properties.

$$Re = \frac{\rho V \bar{c}}{\mu} \tag{2.1}$$

Here, V is the free stream velocity, ρ is the free stream density, $\bar{c}$ is the mean aerodynamic chord and μ is the dynamic viscosity of the air.

At first, the isentropic relation in Equation 2.2 is used to calculate the static temperature T. Using this temperature, the speed of sound can be calculated. The speed of sound and the Mach number are used to calculate the free-stream velocity. Using the velocity, the known cross-sectional area of the

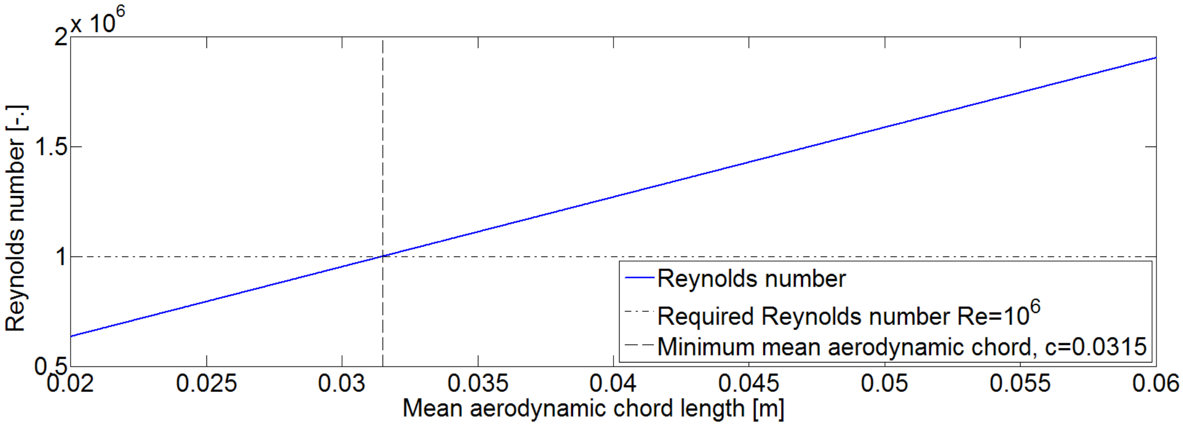

Figure 2.3: Reynolds number, Re, based on the mean aerodynamic chord, $\bar{c}$.

wind tunnel and the given mass flow, the density inside the tunnel is calculated using Equation 2.3.

$$\frac{T_0}{T} = 1 + \frac{\gamma - 1}{2} M^2 \tag{2.2}$$

$$\dot{m} = \rho A V \tag{2.3}$$

Finally, the dynamic viscosity μ is calculated using Equation 2.4, where μ_0, T_{ref} and C_{air} are the reference viscosity, reference temperature and Sutherland's constant for air respectively.

$$\mu = \mu_0 \frac{T_{ref} + C_{air}}{T + C_{air}} \left(\frac{T}{T_{ref}} \right)^{3/2} \tag{2.4}$$

The remaining flow parameters (ρ_0, p and p_0) in the wind tunnel are calculated using the other isentropic relations in Equation 2.5 and the equation of state in Equation 2.6. In the equation, R represents the specific gas constant for air.

$$\begin{aligned} \tfrac{T_0}{T} &= 1 + \tfrac{\gamma-1}{2} M^2 \\ \tfrac{\rho_0}{\rho} &= \left(1 + \tfrac{\gamma-1}{2} M^2\right)^{\frac{1}{\gamma-1}} \\ \tfrac{p_0}{p} &= \left(1 + \tfrac{\gamma-1}{2} M^2\right)^{\frac{\gamma}{\gamma-1}} \end{aligned} \tag{2.5}$$

$$p = \rho R T \tag{2.6}$$

Based on the requirement of $Re_{min} = 10^6$, the minimum mean aerodynamic chord length can be calculated. The calculated values are stated below and the Reynolds number based on the mean aerodynamic chord is plotted in Figure 2.3.

$$\begin{array}{rll} \dot{m} & = 40 & kg/s \\ M & = 0.7 & - \\ A_{test} & = 0.27 \cdot 0.28 & m^2 \\ V & = 226.12 & m/s \\ \mu & = 1.6659 \cdot 10^{-5} & kg/m\ s \\ \bar{c}_{min} & = 0.0315 & m \end{array} \qquad \begin{array}{rll} T_0 & = 285 & K \\ T & = 259.56 & K \\ \rho_0 & = 2.9560 & kg/m^3 \\ \rho & = 2.3399 & kg/m^3 \\ p_0 & = 241.910 & kPa \\ p & = 174.400 & kPa \end{array}$$

Chapter 3 — Model

In this chapter, the design considerations related to the model placed in the test section are presented. First, the geometry space is defined, including the length, chord, sweep and taper of the model. Next, based on requirements, the optimal material space is outlined. A verification of the performance of different possible configurations with different materials is conducted, followed by an explanation of the two-dimensional aeroelastic code used to estimate the time history of the behaviour of the model, together with its flutter performance. The chapter ends with the selection of the final geometry and material for the model.

3.1 Airfoil Selection

The selection of an airfoil is a key factor in the design of the model. In this case, the airfoil choice is fixed in an early stage of the project, since it can be considered relatively independent of the iterative nature of the design process. The choice of an airfoil influences other characteristics such as the possible chord lengths (from thickness limitations, as explained Section 3.3.1), the angle of attack, the flutter speed and the natural frequencies, but this influence can be compensated for by changing other factors, making it possible to take the airfoil selection as the first step.

It is worth noting that a large number of airfoils satisfy the criteria presented in this section, since many airfoils share similar properties. Therefore, in order to decide on the airfoil, a high-level trade-off is performed. This trade-off focuses mostly on the choice between a supercritical and a conventional airfoil shape. The selection is based on three key factors: the simplicity, the availability of test data and the behaviour in the transonic regime.

For simplicity, a symmetric airfoil is optimal, as it does not provide any significant additional challenges for modelling and production, when compared to more complex shapes such as a supercritical airfoil.

In terms of the availability of data, it is essential for the design to be able to predict properties such as the pressures on the airfoil, the lift and moment coefficients, the critical Mach number and the position of the aerodynamic center. A great benefit of using airfoils designed by the National Advisory Committee for Aeronautics (NACA) airfoils is the extensive wind tunnel testing performed by this committee. For NACA 6-series airfoils, test data is compiled in a number of technical reports such as [70]. This makes an airfoil of this series an ideal choice for the model, as significant knowledge exists of its properties, reducing the uncertainties in the design process.

Since the purpose of the experiment is to provide validation data in the transonic regime, it is essential to know the behaviour of the model in these conditions. More specifically, it is very important to have knowledge about the critical Mach number, at which shock waves begin to occur on the airfoil. A supercritical airfoil delays the appearance of these effects. As described in Chapter 2, the Mach number at which the experiment takes place is 0.7. Therefore, it is necessary to select an airfoil which can provide the desired transonic effects at this speed, and an increase of the critical Mach number is undesired.

Using the pressure coefficient data for various angles of attack and Mach numbers, given in [70], and the critical pressure coefficient found from Equation 3.1 [66], it is possible to compute the critical Mach number for every angle of attack. In Figure 3.1, this critical pressure coefficient is plotted along with the pressure coefficients at four locations along the chord (2.9%, 15.1%, 24.9% and 30.1%, as indicated by the subscripts in the plot legend), for an angle of attack of 2.2°. The intersection at the lowest pressure coefficient, $c_{p,min}$, with the critical pressure coefficient gives the critical Mach number.

Then, the data from the available angles of attack is interpolated, as shown in Figure 3.2. The angle of attack for which the critical Mach number of the NACA 64-010 is 0.7 (Section 2.2) is 1.89°,

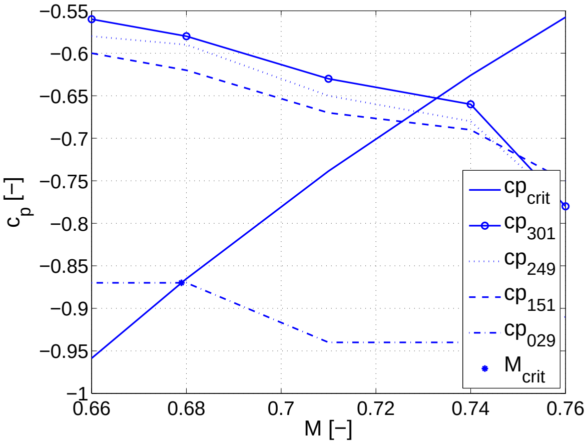

Figure 3.1: Pressure coefficients and critical Mach number for a NACA 64A-010 airfoil at $\alpha = 2.2°$

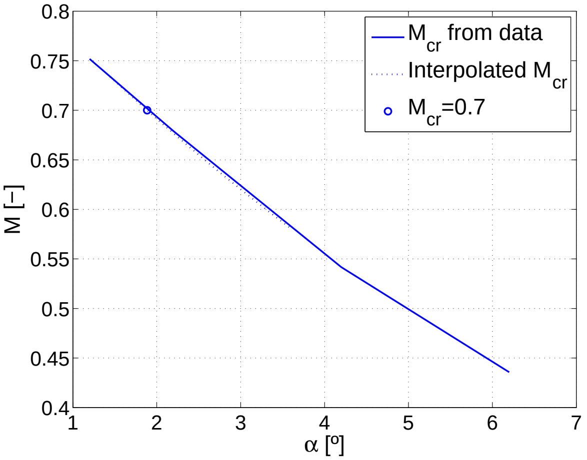

Figure 3.2: Critical Mach number change with angle of attack for a NACA 64A-010 airfoil

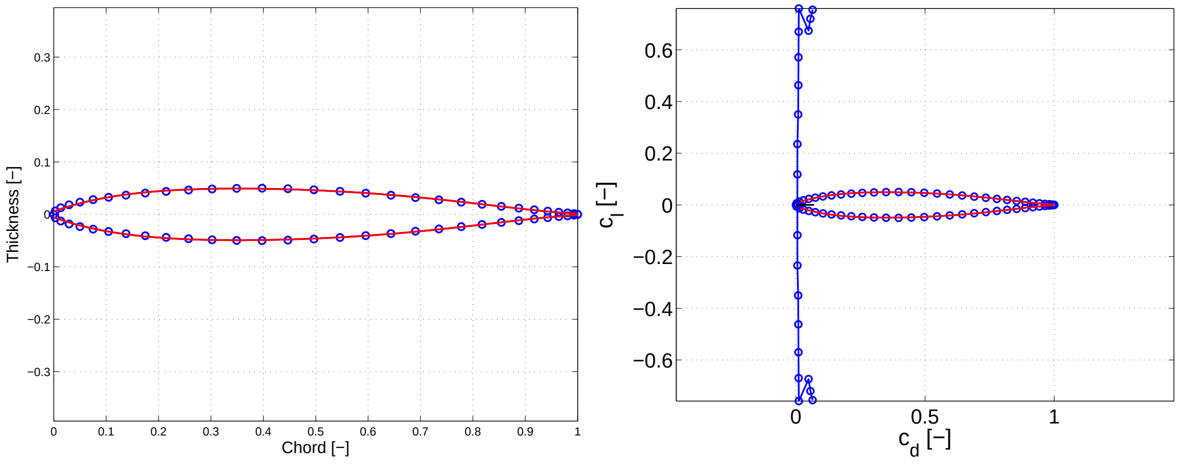

(a) Airfoil shape (polynomial approximation) [70]

(b) Lift-drag polar at $Re = 10^6$ [22]

Figure 3.3: NACA 64A-010 airfoil

which is comfortably achievable during the test, posing no area blockage problems.

$$C_{p,cr} = \frac{2}{\gamma M^2}\left(\left[\frac{1+\frac{\gamma-1}{2}M^2}{\frac{\gamma+1}{2}}\right]^{\frac{\gamma}{\gamma-1}} - 1\right) \tag{3.1}$$

Due to these three main reasons, the NACA 64A-010 airfoil, shown in Figure 3.3a, is selected for use in this experiment. This airfoil's lift-drag polar is shown in Figure 3.3b, for a Reynolds number of 10^6, as stated in Requirement E3.

3.2 Model Planform

Once the airfoil is selected, it can be extended to three dimensions by the sizing of the planform. In this section, the methods used to obtain the length, the chord, the sweep and the taper of the model are described.

3.2.1 Length

The length of the model is strictly constrained by the space available in the wind tunnel test section, which is $28cm$ wide. Equation 3.2 [40] shows that for a beam with every other parameter left constant, the natural frequency decreases with an increase in length. This decrease improves measurability, since the cameras provide an upper limit on what frequency can be measured, as detailed in Chapter 6. However, when the length increases and the model is close to the wall, two factors need to be taken into account: the aerodynamic interference and the wind tunnel integrity.

$$f = \frac{a_n^2}{2\pi}\sqrt{\frac{EI}{\rho A L^4}} \tag{3.2}$$

The wind tunnel size provides limitations for the length of the model in two ways:

Firstly, close to the wall, the flow field is effectively blocked between the model tip and the wall. This leads to high inacurracies in the measurement of velocities and pressures. Therefore, for the accuracy of the values measured at the tip, it is ideal to be as far away from the wall as possible [20]. At a distance of approximately 20% of the wind tunnel width from the wall, these effects are greatly reduced [37]. In this case, the distance to the wall corresponding to 20% is $5.6cm$.

Secondly, the wing must not touch the top or bottom of the wind tunnel when deflecting. Requirement M6 ensures that the model does not deflect more than 10% of its length. When this is met, the model never impacts the walls of the tunnel. In addition, if the model breaks off, it must not impact the side window of the tunnel. However, it is very difficult to predict the path of the model after failure, and therefore a safety factor must be set.

In order to reduce the natural frequency while taking into account these limitations, the model design uses a safety margin of $5cm$ from the wind tunnel wall. In consequence, the model length is set at $23cm$.

3.2.2 Chord

The chord of the airfoil has a significant influence on the model's parameters, and is an integral part of the iterative design process. In this section, limits are set for the chord length, whereas the final chord length is defined at the end of the design phase.

The airfoil selection is made in Section 3.1, and the selected airfoil has a thickness-to-chord ratio of 0.1. This means that the model's thickness is set by the chord, being 10% of its value. This allows minimum and maximum limits for the chord length to be set. In order for the pressure transducers described in Section 6.4 to fit in the model, their length of $9.5mm$ needs to be considered. Therefore, a minimum chord length of $10cm$ is selected. Requirement M5 states the maximum area blockage of the wind tunnel to be 5%. The area blockage, A_{bl}, is calculated in Equation 3.3, where c is the chord length, L is the model length and A_{test} is the test section area. For a chord length of $15cm$, the area blockage is 4.6%, at the maximum static angle of attack of the experiment of 3.6°, meeting this requirement. The maximum chord length is therefore set to be $15cm$.

$$A_{bl} = \frac{0.1cL}{A_{test}} \cdot 100 \tag{3.3}$$

The chord also partly determines the Reynolds number, as shown in Section 2.3. However, requirement E3, which sets the minimum Reynolds number to be 10^6, is met by the minimum limit of 10cm set above, and therefore is not considered further in this discussion.

In addition, the chord partly determines the aerodynamic loading on the model, as shown in Equation 3.4. Here, $C_{L_{max}}$ is the maximum lift coefficient achieved during the experiment, obtained from the maximum angle of attack described in Chapter 7 and the airfoil data available in [70]. The air density, ρ_{air}, and the free steam velocity, V, are determined in Section 2.3. Finally, the area is defined as $S = c \cdot L$. From this, it is clear to see that as the chord increases, the lift load on the model increases linearly.

$$F_L = \frac{1}{2} C_{L_{max}} \rho_{air} V^2 S \tag{3.4}$$

Another very important parameter that is influenced by the chord length is the natural frequency of oscillation of the model. This is analyzed in detail in Section 3.3.3.

Considering all these limitations and influences, the chord length is found after an iterative process, and the result is described in Section 3.5.

3.2.3 Sweep

Sweep is a defining feature of most modern transonic transport aircraft. Since the experiment in question focuses on validating fluid structure interaction solvers in the transonic conditions, it seems logical to include an angle of sweep in the model, giving the experiment additional relevance to actual flight.

One of the main effects of an angle of sweep is a decrease of the local flow velocity of the wing. This causes the appearance of supersonic flow over the wing to be delayed until higher Mach numbers. In this experiment, transonic effects caused by local supersonic flow are one of the desired phenomena to be measured. For the chosen airfoil it is not convenient to delay the critical Mach number further. Therefore, sweep is not desired.

The specific effects of forward sweep on aeroelastic divergence are well known: wings of this type have a large problem with destructive divergence [28], as the bending moment increases towards the tip. This happens because the effective angle of attack increases as the wing bends up [48]. Since divergence is not part of the phenomena to be studied in this experiment, the model does not have forward sweep.

In addition, a model with sweep has a higher degree of coupling between the bending and torsional oscillation modes [79]. This makes the analysis and prediction of the effects of the aeroelastic loads much more difficult, and this is an additional reason not to include an angle of sweep in the model.

In conclusion, the negative consequences of adding an angle of sweep in terms of the complexity of the design and the occurrence of the phenomena desired outweigh the added relevance of a swept design. Therefore, the model has a 0° sweep angle.

3.2.4 Taper

Another characteristic of wings in transonic aircraft is the presence of taper. Once again, the inclusion of this feature in the model provides an increase in relevance to real flight.

One of the main disadvantages of the use of a taper ratio below one in this experiment is the increase in both bending and torsional frequency, caused by a reduction of mass and chord at the tip of the wing. A taper ratio larger than one has the opposite effect, but brings with it a significant decrease in the flutter speed [80].

In addition, a planform with a taper ratio different to one is considerably more complex to analyze and manufacture, which introduces more uncertainties and risks to the design.

Due to this, similarly to the decision made for the sweep angle, the frequency and flutter speed changes are not considered beneficial to the experiment when compared to the additional complexity a tapered wing generates. Therefore the taper ratio of the model is $\lambda = 1$.

3.3 Structural Sizing and Material Selection

In this section, the methodology leading to the final structure, dimensions and material selection for the model is described. Figure 3.4 shows the procedure followed in order to find this final selection, divided into two main stages.

The first stage, described in Section 3.3.1 and corresponding to the non-coloured part of Figure 3.4, starts with requirement M1.1, where the maximum allowable deflection is set to 10% of the length of the model. From this, a necessary bending stiffness can be found. Then, taking into account possible shapes, chord lengths, thicknesses and reinforcements, the moment of inertia possibilities are found. Finally, simplified criteria are set up in order to prevent yield failure of the model. These three inputs form the base of a selection of ranges for the material's Young's modulus and its yield strength, leading to a material selection space including all the materials that are options for the design.

Then, the behaviour of different material choices is then analyzed for different aspects, such as frequency response, material properties at operating temperatures, material processability, flutter boundary limits and skin buckling. This corresponds to the shaded part of Figure 3.4. This procedure is iterated for the different options in the material space, and for the various chord length and thickness combinations considered. The best performing configuration with respect to these criteria is then selected.

Finally, a summarized description of the final selection can be found in Section 3.5.

3.3.1 Design Space Set-up

The process used to set up Young's modulus and yield strength bounds for materials is described in this section. It is broadly divided into three parts: the deflection requirement, the moment of inertia possibilities and the failure prevention.

Deflection Based on requirement M6, the maximum allowable deflection is set to 10% of the length of the model. This ensures that no nonlinear effects occur when a load is acting on the model. That is, the length of the model can be assumed constant as it bends, and no shortening or warping effects need to be considered. In addition, when the model does not deflect more than 10%, the lift distribution can be assumed to act entirely in the vertical direction with regard to the wind tunnel wall, and does not rotate with the model deflection towards the tip. Furthermore, the chord length remains constant, as described in Section 3.2.2. Considering these factors, Equation 3.5 shows the relation between the deflection obtained when a uniformly distributed load is applied, where w is the distributed load, L is the length of the model, E is the Young's modulus of the material, I is the cross sectional moment of inertia and k is ratio between the deflection and the length of the model. As explained, the maximum deflection is 10% of the length, and therefore d has a value of 0.1.

$$\delta = \frac{wL^4}{8EI} = dL \tag{3.5}$$

The distributed load comes from the lift acting on the model per unit length, at the maximum static angle of attack in the experiment ($\alpha = 3.6^\circ$ and $C_L = 0.5$) and is given by Equation 3.6, where

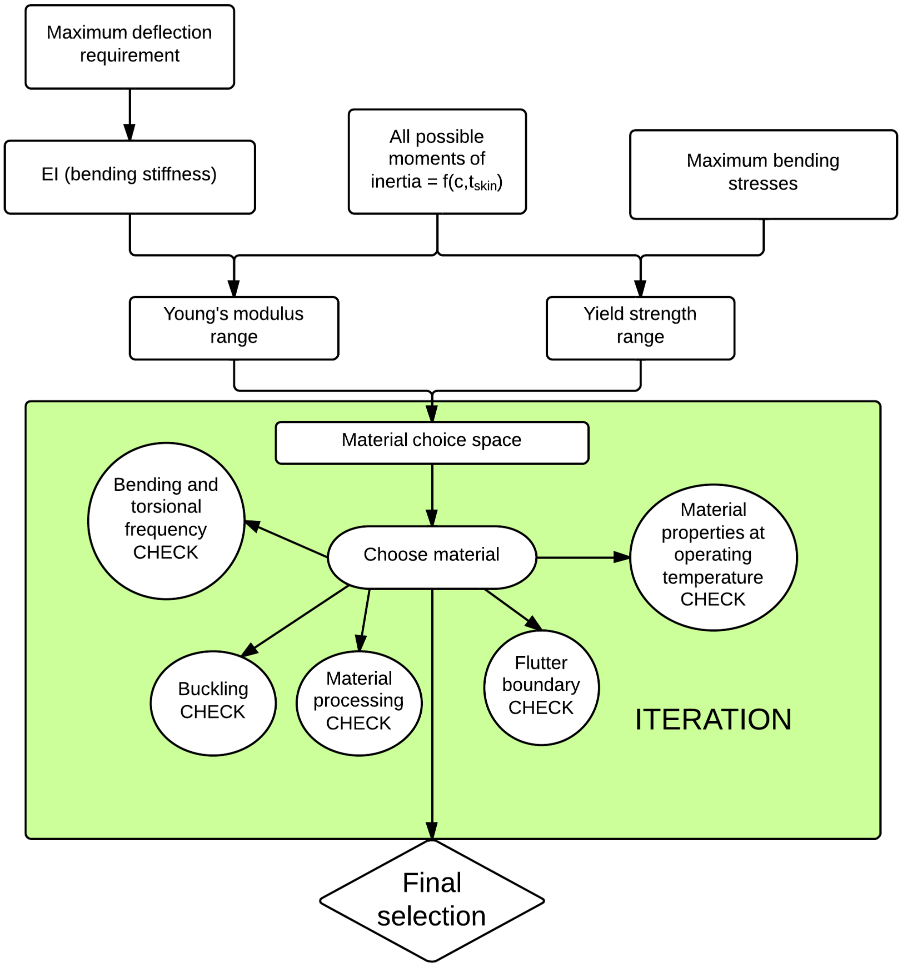

Figure 3.4: Description of the structure and material selection process

ρ is the density of the air in the test section, assumed constant, $\bar{c}$ is the chord length of the model and V is the free stream velocity in the test section. The values for ρ and V are determined in Section 2.3.

$$w = \frac{1}{2} C_L \rho V^2 \bar{c} \tag{3.6}$$

At this stage of the analysis, using Equation 3.5, the required bending stiffness EI can be obtained, as a function of the chord length. The chord length is determined, in Section 3.2.2, to vary between $10cm$ and $15cm$. To calculate EI, a discrete number of chord lengths covering this interval, with a spacing of $0.1cm$ are used. Finally, this results in 51 different values of required EI.

Moment of Inertia Due to shape and manufacturability restrictions, not all of the necessary moments of inertia calculated above are feasible for the model. The airfoil shape is set in Section 3.1, and together with the chord length range from Section 3.2.2, they set the thickness of the model.

There are a variety of possible internal structures in order to achieve the required inertia. In order to not introduce any additional complexities in terms of design analysis and manufacturing, a hollow airfoil section is chosen, as shown in Figure 3.5. The iterative process is then followed, and in the case that this choice does not meet the requirements in terms of frequency, strength or flutter boundary,

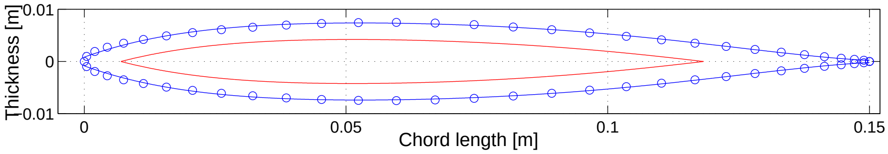

Figure 3.5: Hollow airfoil approximated with polynomials and datapoints

reinforcements can be added. As can be seen from the result of the iterative process in Section 3.5, this proves to not be necessary.

For the hollow model, the moment of inertia depends primarily on the skin thickness. For this, a lower and upper bound are set. The minimum thickness is set at $2mm$, for manufacturability and skin buckling concerns. The maximum limit is set at $5mm$, which constitutes a solid airfoil section. In order to calculate the moment of inertia, the airfoil shape data points found in [70] are implemented in MATLAB. A polynomial is fitted over this data for the top, $Z_u(x)$, as well as for the bottom contour, $Z_l(x)$. Using these polynomials, the cross-sectional area, A, the neutral surface position, z_{n0}, and the second moment of area about the x-axis, I_{xx}, can be computed. These three variables are shown in Equation 3.7, Equation 3.8 and Equation 3.9, respectively. The required moment of intertia for a hollow airfoil is calculated by subtracting the inner shape from the outer shape. The minimum and maximum chord used in this iteration follow from Section 3.2.2.

$$A = \int_0^c \left[Z_u - Z_l\right] \mathrm{d}x \tag{3.7}$$

$$\bar{z} = \frac{1}{A} \int_0^c \frac{1}{2} \left[Z_u^2 - Z_l^2\right] \mathrm{d}x \tag{3.8}$$

$$I_{xx} = \frac{1}{A} \int_0^c \frac{1}{3} \left[(Z_u - z_{n0})^3 - (Z_l - z_{n0})^3\right] \mathrm{d}x \tag{3.9}$$

Equation 3.9 gives a range of possible moments of inertia. Taking the maximum and minimum values, and combining with the EI resulting from the previous section, it is possible to set requirements on the minimum and the maximum Young's modulus and set up a range of possible materials, as shown in Equation 3.10.

$$E_{min} = \frac{EI}{I_{max}} \quad \text{and} \quad E_{max} = \frac{EI}{I_{min}} \tag{3.10}$$

This range, taking into account materials possible for all chord lengths, is from $3.6GPa$ to $22GPa$.

Failure Prevention A second constraint on the material choice is the yield strength. Here, a first order analysis is performed to prevent failure in bending. Later a more thorough numerical check is performed in Section 3.3.5. The maximum second moment of area is used to determine the minimum required yield strength of the model for it to just fail, found using Equation 3.11. In this equation M is the maximum bending moment on the model, derived from Equation 3.6, to which a safety factor of 2 is applied, y is half the maximum thickness of the airfoil, $y = 0.05c$, with the chord varying from $10cm$ to $15cm$.

$$\sigma_{yield,min} = \frac{M \cdot y}{I_{max}} \tag{3.11}$$

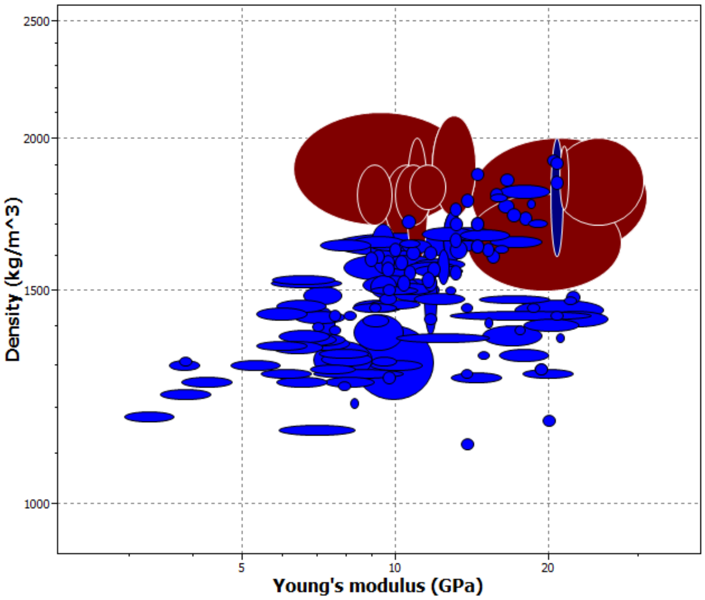

Figure 3.6: Material selection range, Young's moduls against density

The minimum yield strength found is $94MPa$, which is used to further restrict the material selection space.

Design Space With the criteria described above in place, the material selection process is started. The calculated information on the minimum and maximum Young's modulus and the minimum yield strength is inserted in the CES EduPack [10] material selection software. This software picks the materials that meet the requirements and plots the desired properties against each other. Figure 3.6 shows such a graph, where the density is plotted against the Young's modulus. These two characteristics are chosen since they directly influence the modal oscillation frequency of the model, as shown in Equation 3.12. Materials with the lowest ratio E/ρ, in the top left corner, provide the lowest eigenfrequencies, within the defined range. In this graph, only the options that satisfy the set requirements are plotted.

From this range, a suitable material is selected, and its density, Young's modulus and yield strength are used as input data. The required bending stiffness EI is obtained as described above. This is divided by the material's Young's modulus to obtain the required moment of inertia. This is then compared to the obtainable moments if inertia, and the closest match is selected, within the ranges.

From the requirements, it is found that the first bending mode and torsion modes must be measurable by the Particle Image Velocimetry (PIV) camera, as described in Section 6.2. In order to verify whether the camera is able to measure the bending and torsion natural frequencies, the bending and torsion frequencies must be calculated. The natural frequencies for bending can be calculated analytically, while the natural frequency for torsion is too complex to calculate analytically. Therefore, the torsional frequency is calculated numerically and used as a confirmation along with numerical calculations of the bending frequency, as described in Section 3.3.3.

In order to calculate the natural frequencies for bending, the model is approached as a cantilever beam. For a cantilever beam, the eigenfrequency can be calculated with Equation 3.12, in which α_n, for the first three natural frequencies, is 1.875, 4.694 and 7.885 respectively.

$$f_n = \frac{\alpha_n^2}{2\pi}\sqrt{\frac{EI}{\rho A L^4}} \tag{3.12}$$

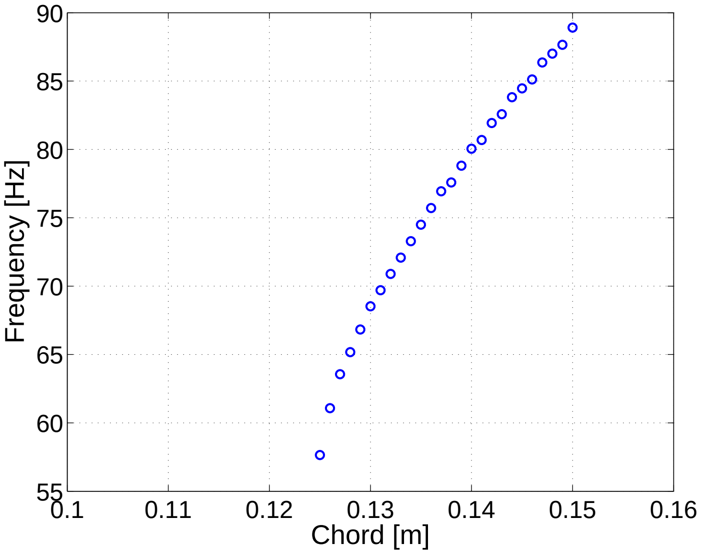

Figure 3.7: Frequency against chord length for chopped roving reinforced polyester

Table 3.1: Material properties of the three chosen materials

Material	ρ $[kg/m^3]$	**E** $[GPa]$	σ_{yield} $[MPa]$
PP42	1200	9.42	211
SRP	1200	13.8	193
Polyester	2100	6.3	166

Once the first bending mode frequency is calculated analytically, it is verified if any of the values, varying with the chord, fall within the acceptable range defined by the cameras in Section 6.2. If not, another material is chosen. If acceptable frequencies are found, a primary check for yield failure is performed and the chord lengths that fail are eliminated. The procedure results in a set of design points for each material. An example plot of these design points is shown in Figure 3.7, for the chopped roving reinforced polyester material.

Once the design space has been chosen, the next step is to evaluate the different choices in terms of their natural frequencies. Every configuration has different characteristics in terms of flutter behaviour, skin buckling, failure behaviour, material processing and material properties at the operating temperature of the wind tunnel, and these all need to be analyzed. Some aspects, such as natural torsion frequency, skin buckling and the flutter boundary, are difficult to predict analytically. Thus, after narrowing the design space, an additional analysis is needed for such parameters, for which the prediction was not possible analytically.

The materials in the design space are subjected to the initial frequency and failure tests described in this section. Then, from the materials that give the best results, a preliminary selection is made. Over the next sections, the necessary checks are explained and detailed, for the three best materials resulting from this primary selection. These materials are presented in Table 3.1, along with their most important material properties.

- Self Reinforced Polypropylene (SRP)
- Polypropylene, reinforced with 42% directionalized glass fiber (PP42)
- Chopped roving (glass fiber) reinforced polyester (Polyester)

3.3.2 Flutter Boundary

As explained in Section 3.4.2, for each material choice the model is investigated structurally. It is verified that the structure can withstand the applied loads and that it does not exceed the maximum allowable deflection. Following, an analysis of the flutter boundary is performed, using the aeroelastic model implemented in MATLAB is performed. This is necessary in order to ensure that none of the bending and torsion modes, or the coupling between the two, diverge at the operating velocity and Mach number in the wind tunnel. Thus, in Figure 3.8, the wind tunnel velocity line (solid) must be below the flutter velocity line (circles). It is important to mention that, even when the operating velocity is below the flutter boundary, sufficient tolerance with respect to a small change in the Mach number has to be achieved. This is due to the fact that the presence of the model in the test section can have an influence on the actual Mach number. A more detailed analysis of this aspect is presented in Section 8.1.2.

In Figure 3.8, Figure 3.9 and Figure 3.10 the flutter speeds for the three chosen materials, described in Section 3.3.1, are shown and plotted in the same graph as the free stream velocity in the wind tunnel, represented by the solid line. In order for the model to stay clear of destructive flutter, the data points for the chosen material must be above this line. When this is not the case, the oscillations of the model leads to a very rapid failure, with no time for intervention. Therefore, it is crucial to leave a safety margin to this boundary to deal with unforeseen changes in the Mach number or the model's properties. The goal is to achieve a sufficient measurement time, while staying within safe flutter boundary limits. This means that the model should be as close to the flutter speed as possible at the experiment Mach number of 0.7, while not reaching it with a small change in Mach number. This is explained in more detail in Section 8.1.2.

The figures are grouped by skin thickness, and for every skin thickness three chord lengths and three different materials are analyzed. The thicknesses chosen are $2mm$, $3mm$ and $4mm$, the chords are $130mm$, $140mm$ and $150mm$, while the materials are SRP, PP42 and glass fibre reinforced polyester.

From Figure 3.8, it is clear to see that, for a thickness of $2mm$, only PP42 does not flutter at $M = 0.7$. However, when the Mach number increases even slightly, or any factor affects the flutter speed, the model is at high risk of flutter. Figure 3.9 shows that, at a thickness of $3mm$, all three materials do not induce flutter in the model at $M = 0.7$. PP42 and SRP are above the boundary for any Mach number, and therefore safe. Polyester only has an acceptable margin for a chord length of $150mm$, but is at an ideal distance from the flutter boundary considering the measurement time. In Figure 3.10 it is shown that at a thickness of $4mm$, all materials fall withing the acceptable range for flutter speed.

In conclusion, it can be stated that as the thickness increases, so does the flutter speed. An increase in chord length also increases the flutter speed, but only very slightly in comparison. The polyester model with a thickness of $3mm$ and a chord of $150mm$ provides a good compromise between safety for the flutter speed and measurement time.

3.3.3 Natural Frequency

The natural bending frequency can be obtained analytically for each material and for each skin thickness that prevents the model from failing under the applied loads. However, the natural torsion frequency is obtained through Patran/Nastran. In Section 3.2.1, it is shown that a longer model length is more beneficial with respect to the bending frequency. In Section 6.2, limitations imposed by the cameras used to measure the frequencies are presented. The frequency at which the camera can measure and entire oscillation with ten data points is $270Hz$. Thus, at least the first bending mode and the first torsional mode have to fall under these limitations. The frequencies obtained for each of the three materials analyzed in detail are presented in Figure 3.11.

Analyzing Figure 3.11a, it is clear that, leaving the thickness constant, the chord length does not influence the torsional frequency. In addition, it only has a small effect on the bending frequency, slightly increasing it with an increase in chord. For the thickness, as shown by Figure 3.11b, an

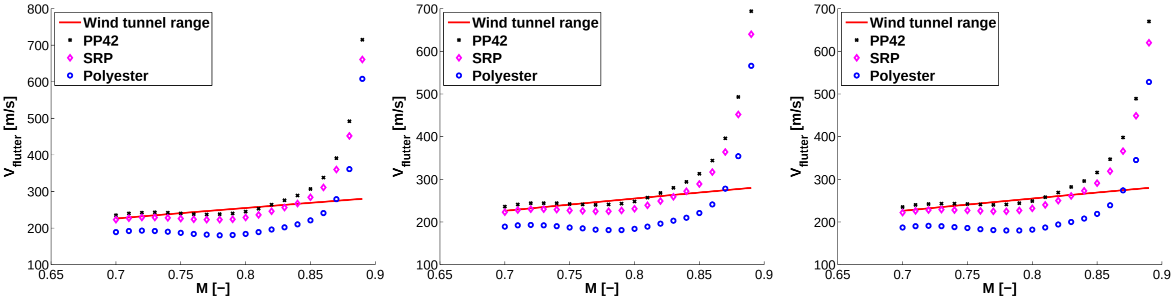

(a) 130mm chord length (b) 140mm chord length (c) 150mm chord length

Figure 3.8: Flutter speed for 2mm skin thickness

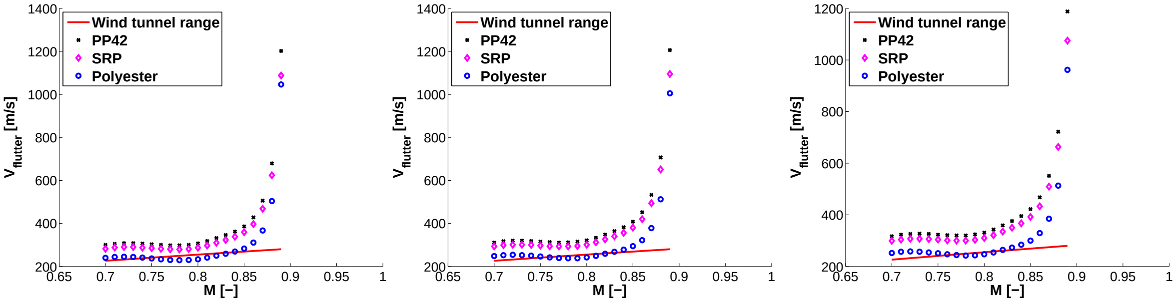

(a) 130mm chord length (b) 140mm chord length (c) 150mm chord length

Figure 3.9: Flutter speed for 3mm skin thickness

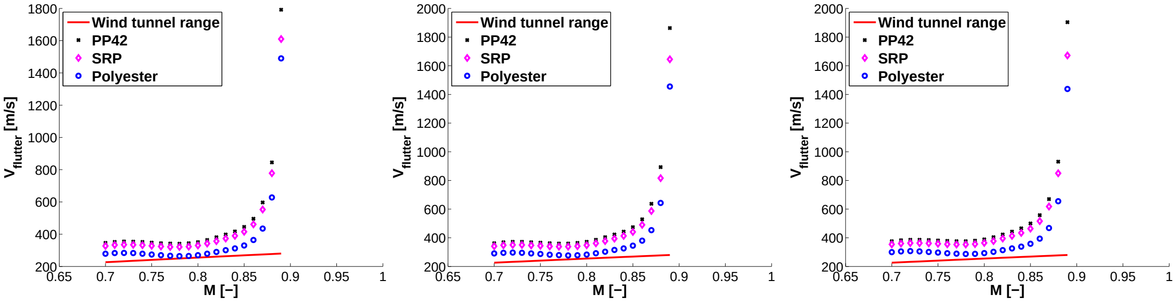

(a) 130mm chord length (b) 140mm chord length (c) 150mm chord length

Figure 3.10: Flutter speed for 4mm skin thickness

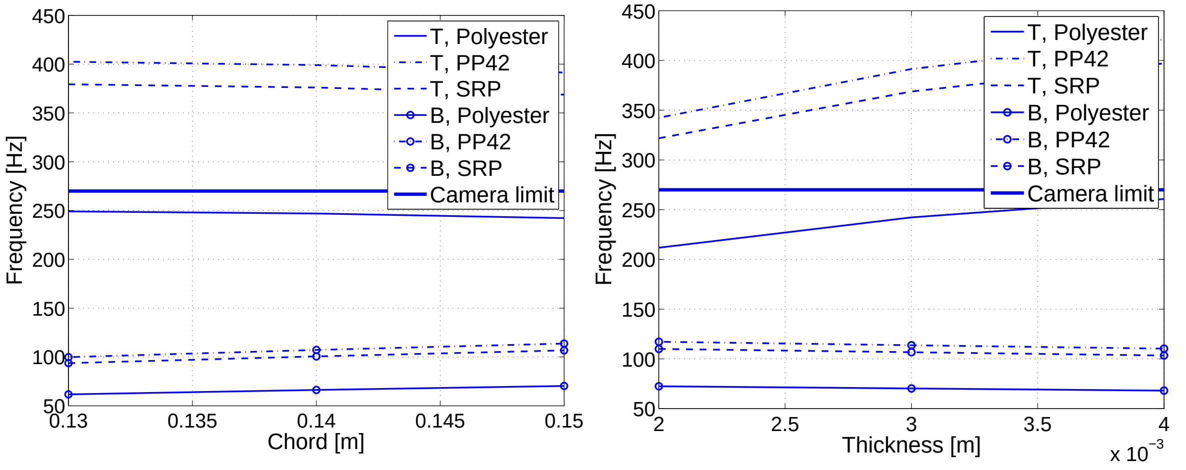

(a) Variable chord, t=3mm

(b) Variable thickness, c=0.15m

Figure 3.11: Variation of frequency for three materials

increased thickness does not affect the bending frequency significantly, but it does cause a large increase in the torsional frequency. From both figures it is also clear that for the material choice, the glass fibre reinforced polyester has by far the best torsional frequency properties, staying constantly under the camera limit over the entire thickness range. In addition, it also has the lowest bending frequency.

In Figure 3.11, it was shown that the chord length does not influence the torsional frequency when the thickness is left constant. However, a larger chord length allows the same moments of inertia to be achieved with a lower thickness, which means that it is possible to benefit from the frequency effects of a reduced thickness, while not losing bending stiffness. This is shown in Figure 3.12, where the thickness is minimized for every chord length, with regards to failure criteria and deflection requirements. As can be seen, a larger chord is highly beneficial in terms of torsional frequency, while performing only slightly worse in terms of the bending frequency.

3.3.4 Buckling

There are several ways in which a structure can fail due to buckling. For a wing, the most common buckling type is skin buckling. When the wing is loaded, it deforms upwards, causing the top skin to be in compression and the lower skin to be in tension, as displayed in Figure 3.13. For each geometry there is a critical buckling force, meaning that for each planform and skin thickness the skin buckles at a certain applied loading. Therefore, the model should be designed in such a way that the loading of the model is lower than the critical buckling loading in order to prevent buckling.

Calculating the critical buckling factor analytically is inaccurate due to the airfoil shape and the complex loading of the model. Therefore, the model is analyzed using Patran/Nastran. With this software, the airfoil is modelled as a shell with a certain thickness and a uniform pressure. The analysis runs for different planforms, thicknesses and materials and can therefore be part of the iterative process of determining the final model design. From the analysis, a critical buckling factor is calculated by Nastran. In order to prevent buckling, the critical buckling factor must be higher than one. However, in order to prevent any unexpected effects, a safety factor of two is introduced, as described by Requirement M7. To design the model for buckling, it is important to know how the buckling factor changes with changes in certain parameters. Therefore, the effects of changing the chord length, the model length, the thickness and the elastic modulus are analyzed. The results of this analysis can be found in Figure 3.14. For this analysis, the model is modelled as a shell, with an applied uniformly distributed pressure load of 10kPa, and a material with a density of 1000$kg \cdot m^{-3}$, an elastic modulus of 10GPa and a Poisson's ratio of 0.3.

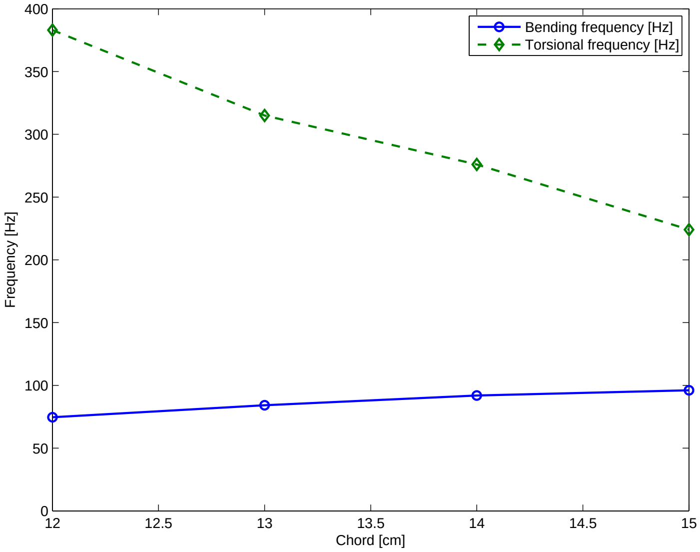

Figure 3.12: Variation of frequency with chord, variable thickness

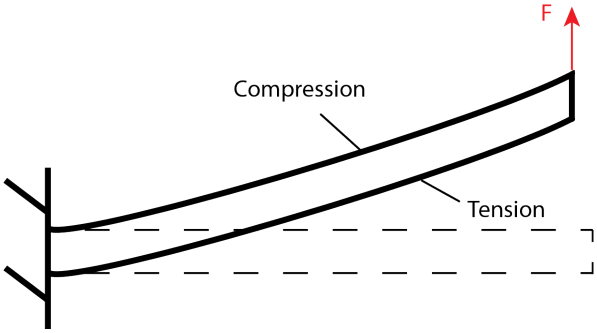

Figure 3.13: Compression and tension on the skin due to a loading on the tip

Influence of Chord From Figure 3.14a, the relation between the chord length and the buckling factor can be found. For the first analysis, the planform has a thickness of $2mm$, a chord of $130mm$ and a length of $224mm$. For the chord length of $130mm$, the model has a buckling factor of 2.53, which means that the model starts to buckle if the load increases by a factor of 2.53. To see the influence of chord length on the buckling factor, the chord is increased by four steps of $10mm$. From these five data points, the relation between the chord and the buckling factor can be determined. As can be seen from Figure 3.14a, the buckling factor does not change significantly with changes in chord length.

Influence of Length The influence of changing the length of the model on the buckling factor can be found in Figure 3.14b. For this analysis, the same thickness of $2mm$ is used as for the analysis of the chord. The chord length is set to $112mm$ and the length is varied to see the relation between the length and the buckling factor. The length of the model is varied from $90mm$ to $250mm$ in four steps of $40mm$. The relation between the length of the model and the buckling factor is found to be approximately quadratic.

Influence of Thickness The influence of changing the thickness of the model on the buckling factor can be found in Figure 3.14c. The model that is used for this analysis is the same as for previous

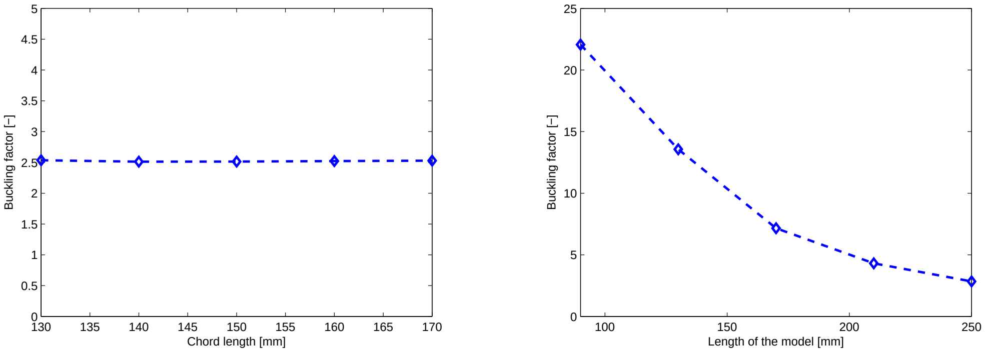

(a) Buckling factor as a function of chord length (b) Buckling factor as a function of length

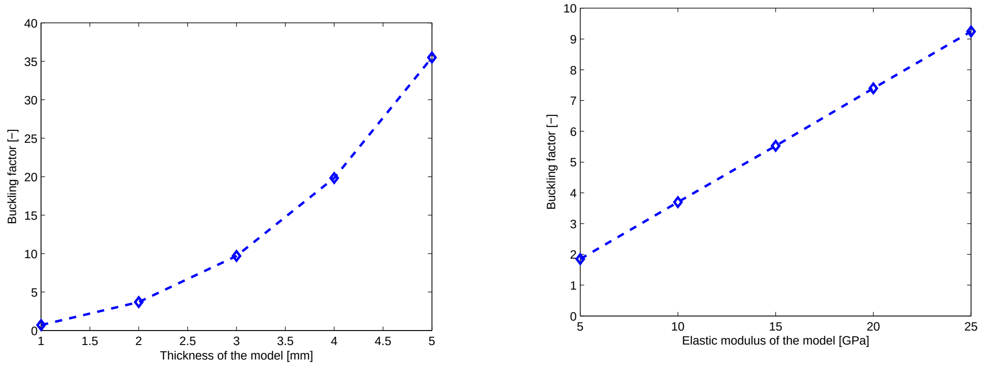

(c) Buckling factor as a function of skin thickness (d) Buckling factor as a function of Young's modulus

Figure 3.14: Influence of design paramters on the buckling factor

analysis, with a chord of $112mm$ and a length of $224mm$. However, the thickness is varied from $1mm$ to $5mm$ with steps of $1mm$. From Figure 3.14c, it can be found that the buckling factor increases quadratically with an increase in thickness.

Influence of Young's Modulus Now that the influence of the geometric variables are covered, the influence of the material properties are described. Since the density of the material does not change the buckling factor, only the influence of the elastic modulus is covered. The model that is used for the analysis is the same as for the previous analysis. However, the thickness is kept to $2mm$ and the elastic modulus is varied from $5GPa$ to $25GPa$ in steps of $5GPa$. From the results in Figure 3.14d, it can be found that the buckling factor increases linearly with an increase in elastic modulus.

Results From the four above mentioned analysis, the following conclusions can be drawn with respect to the influence of variables on the buckling factor:

- The chord length and density do not have a significant influence on the buckling factor
- The buckling factor decreases quadratically with an increase in length
- The buckling factor increases quadratically with an increase in thickness
- The buckling factor increases linearly with an increase in elastic modulus

From these results it can be concluded that the model should be as short and thick as possible and should have a material with a high elastic modulus to prevent buckling. Since skin buckling can

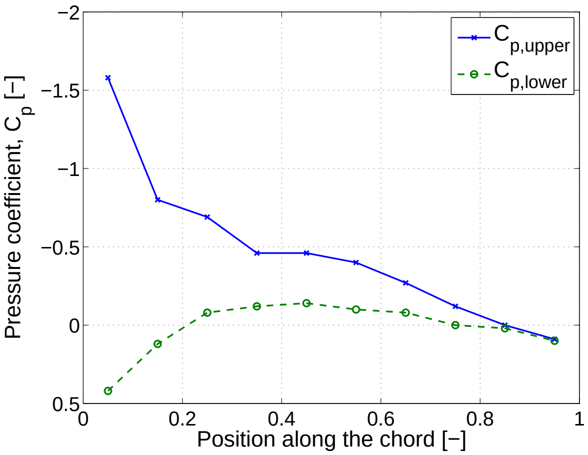

Figure 3.15: Pressure coefficient distribution along the chord of the model

be a serious problem for thin wind tunnel models, Requirement M7 sets the necessary buckling factor of two. However, if the buckling factor of two is not achievable by varying the parameters described above, there are other ways to prevent buckling. For instance, adding a spar to the model significantly increases the buckling factor.

Final Choice For the final design choice, the wing loading is changed from a uniformly distributed pressure load to a distributed loading along the chord, to obtain more accurate results for the buckling factor and the stress. To get a good representation of the loading of the model, the pressure distribution for the NACA 64A-010 airfoil at 4.2° is used [70], as is presented in Figure 3.15. For this analysis, the wing is split up in ten sections along the chord length, for which each section has its own pressure loading according to the pressure coefficient.

Figure 3.16 shows the variation of the buckling factor for the three materials considered for more detailed analysis, as a function of chord and thickness. From Figure 3.16a it is clear that the chord length has no influence on the buckling properties of the structure. Figure 3.16b shows clearly that as the thickness increases, the buckling factor improves.

In terms of materials, PP42 has the best properties, followed by SRP and finally polyester is the material with the lowest buckling factor. However, even for this material, a buckling factor of two is achievable for a chord length of $15cm$ and a thickness of $3mm$.

3.3.5 Stress Failure

A second failure mode for the model is stress failure. Failure due to stress means that the maximum stress of the model reaches the fracture point. Before this fracture point, the model deforms plastically. The stress at which the material begins to deform plastically is called the yield strength of the material. Since plastic deformation alters the shape of the model and thus influence the validation data from the experiment, plastic deformations are not allowed during the experiment. Therefore, the model must be made from a material that has a yield strength above the maximum stress. To account for uncertainties, a safety factor of 2 is required for the yield stress.

To design the model for yield stress, the maximum stress on the model must be known. Calculating the stress on the model can be done both analytically and numerically. Analytically, only the bending stress is considered since this is the main contributor to the stress. Numerically, the normal and shear stresses in all directions is considered and the von Misses stress is used to verify the analytical stress calculation and to design the model for stress. Note that the numerically calculated stress is slightly higher, since the shear stresses are also taken into account in this analysis.

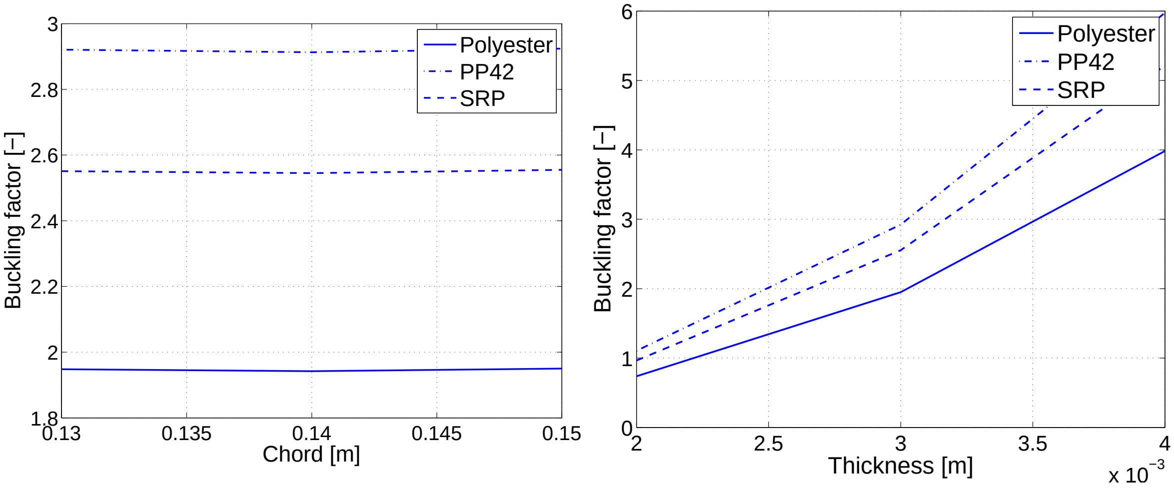

(a) Variable chord, t=3mm

(b) Variable thickness, c=0.15m

Figure 3.16: Variation of buckling factor for three materials

The bending stress can be found analytically using Equation 3.13. In this equation, the loading comes from a uniformly distributed load which results in a moment. The moment is maximum at the root of the model, which is where the maximum bending stress occur. The maximum stress occur at the maximum thickness position of the airfoil, since this has the highest distance from the neutral axis.

$$\sigma = \frac{M \cdot y}{I_{xx}} \tag{3.13}$$

The stress can be found numerically using Patran/Nastran. The software calculates the von Mises stress, using Equation 3.14, which includes normal stresses and shear stresses in all directions and makes it more accurate than the simple bending stress analysis performed in Section 3.3.1. The von Mises stresses found with an example analysis were found to be about 20% higher than the analytically calculated bending stress. For a safe design, a material must be chosen with a yield strength that is at least twice as high as the maximum von Mises stress, which is found numerically.

$$\sigma_{vm} = \frac{1}{\sqrt{2}}\sqrt{(\sigma_{xx}-\sigma_{yy})^2+(\sigma_{yy}-\sigma_{zz})^2+(\sigma_{zz}-\sigma_{xx})^2+6\tau_{xy}^2+6\tau_{yz}^2+6\tau_{zx}^2} \tag{3.14}$$

The von Mises stress is not considerably influenced by the choice of material, and therefore in Figure 3.17 it is taken as independent of the material. In this figure, the von Mises stress is plotted against thickness and chord, and the yield strength of the three materials is also shown. Figure 3.17a shows that the von Mises stress decreases as the chord length of the model increases. In addition, for this thickness, all three materials have a safety factor larger than 2 for yield failure. In Figure 3.17b it can be seen that, similarly to the chord, the von Mises stress decreases with the thickness. When decreasing the thickness to 2mm, the yield safety factor of the polyester model falls to below 2, which is not acceptable. However, at higher thicknesses the polyester material poses no problems in terms of yield strength.

3.3.6 Material Processing and Properties

An import aspect during the material choice, is determining whether the design can be manufactured using a certain material. For this experiment it is important to consider whether a manufacturing technique can be used in which only a small number of products can be produced in a cost-effective way. Furthermore, since the test section of the TST-27 is expected to reach temperatures as low as

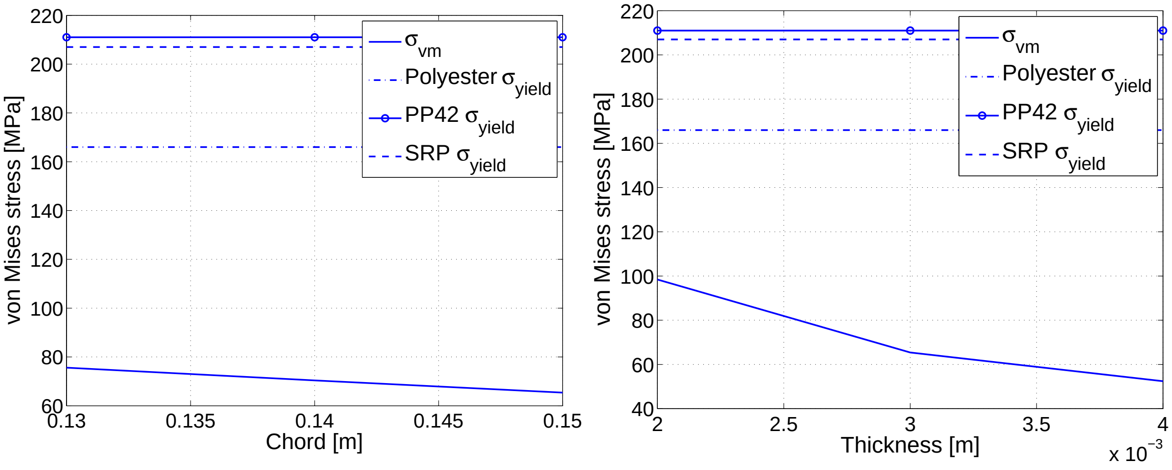

(a) Variable chord, t=3mm

(b) Variable thickness, c=0.15m

Figure 3.17: Variation of von Mises stress

$260K$, or $-13°C$, it is important to consider whether this has any detrimental effect on the material properties.

Polypropylene Polypropylene (PP) reinforced with glass fibre is suitable for compression moulding, injection moulding and closed die forging. Of these options, forging is the only suitable option as it can be used to create a single unique product at a low cost [10]. The downside of this method is that it is not able to offer small tolerances, which means that this material either requires expensive processing after moulding or a more expensive manufacturing technique is required. Not only is PP difficult to process, but it is also not suitable for use with low temperatures. At $-3°C$ PP becomes brittle, therefore this material is unsuitable for an experiment in the TST-27 wind tunnel for which flexibility is required.

Self reinforced polymer SRP products are created using injection moulding and compression moulding, however both processes are only suitable for high volume production. Since SRP contains no fibre reinforcements and is a thermoplastic, it can be considered for three-dimensional printing [26]. Three-dimensional printing reduces the costs of processing, since it does not require a mould and depends less on the skill of human operators. Not only is SRP suitable for creating the model, it also retains its material properties at cryogenic temperatures [58].

Chopped Roving Reinforced Polyester A reinforcement of chopped rovings allows for wet lay-up, spray-up, Resin Transfer Moulding (RTM) and compression moulding. The first three options are suitable for creating a single product, which means that this material is suitable for manufacturing [38]. Polyester can be used to temperatures up to $-47°C$, which means that this material is suitable for use at low temperatures as well. Furthermore, based on [61], it can be assumed that the mechanical properties at high frequencies remains the same.

3.4 Aeroelastic Model

In this section, a numerical method for predicting the aeroelastic behaviour of the model in transonic flight is presented. First, the aeroelasticity for the transonic regime is explained. Next, the theory that is used is explained, together with its required input, advantages and limitations and assumptions. Finally, the model response is explained together with what can be obtained from this response.

The goal of this project is to provide validation data for transonic flight. Under transonic flow conditions, small displacements of the airfoil section will produce large changes in the aerodynamic forces and pitching moments about the elastic axis. Furthermore, under time-dependent conditions, considerable phase differences can exist between the airfoil motion and the resultant loads. These unsteady and transonic effects have a major influence on the flutter speed and should therefore be implemented.

The theory from Theodorsen [73] is well known for its unsteady aerodynamic effects, but it only covers subsonic speed regimes and incompressible effects, and is therefore not valid for transonic speeds. The theory from Crouse and Leishman, described in [30] deals with transonic and unsteady effects. The downside is that neither of the methods take three-dimensional effects into account. It is chosen to use the theory from [30] to predict and describe the flutter behaviour because of its transonic and unsteady implementations, and its relative simplicity.

3.4.1 Theory

The theory in [30] describes the aeroelastic effects using state space representations containing the first order differential equations describing the unsteady aerodynamics. Those equations can then be coupled with the structural response equations governing a two degree of freedom airfoil motion.

There are some advantages regarding the use of a state space representation. First of all, the use of a multiple input - multiple output system can be easily implemented. That is, the time response analysis of different outputs can be obtained with small changes in the implementation. Moreover, the use of a state system representation is attractive due to the possibility of analyzing the stability of the system either by eigenanalysis or by time integration of the state variables. The main goal is therefore to perform a flutter analysis in order to verify that the model remains within safe flutter limits during the operation of the wind tunnel. The two following state space systems can be identified: aerodynamic model and aeroelastic model.

In transonic flow conditions, the governing aerodynamic equations become inherently non linear. These non linearities are caused by the change in the airfoil pressure distribution through the shock waves. To implement these phenomena in the aeroelastic model, the aerodynamic centre and the normal force slope as a function of Mach number are needed. Then, both parts of the model are explained. Finally, the complete unsteady aeroelastic model that combines the aerodynamic and the aeroelastic models is explained.

Required Input To describe the aeroelastic behaviour in the transonic flight regime, the loads involved in this regime have to be known. To calculate the normal force and pitching moment, the normal force curve slope (C_{N_α}) and the aerodynamic centre (x_{ac}) have to be known as a function of Mach number. The normal force is the integration of the pressure distribution along the chord and the aerodynamic centre is the place where the resultant normal force acts on the wing. For low and high Mach numbers the pressure coefficient is proportional to the Mach number. As a result, the normal force coefficient is also proportional to the Mach number. In Figure 3.18, the relation between the pressure coefficient and the Mach number is given.

From Figure 3.18, it can be seen that an asymptote is present when the Mach number equals one. To predict the aeroelastic phenomena and the structural response in the transonic flight regime, it is important to have accurate data for both the normal force curve slope and the aerodynamic centre. Since the existing software is not highly accurate in this flight regime for the normal force curve slope and even less accurate in predicting the aerodynamic centre as a function of Mach number, it is preferred to use experimental data. The NACA 64A-010 is a well known and studied airfoil for which experimental data is available. The experimental data used is generated by the Ames Aeronautical Laboratory and the data can be found in [70]. The data obtained from this work for the transonic flight regime is given in Figure 3.19.

Since only five data points were available for the normal force slope and six for the aerodynamic centre for the NACA 64A-010 in [70], a cubic spline interpolation is made to know the corresponding

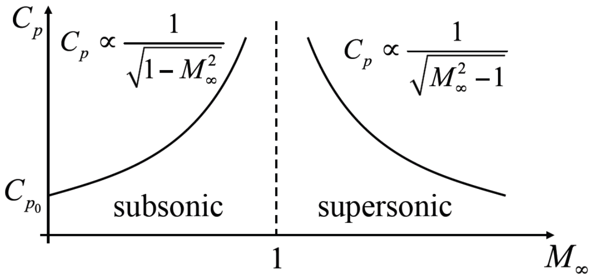

Figure 3.18: Relation of the pressure coefficient with Mach number [66]

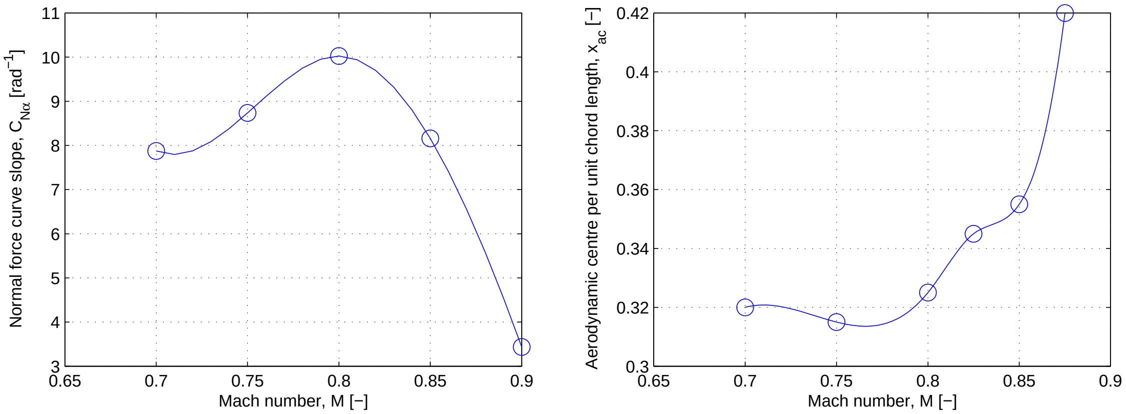

(a) Normal force slope as function of Mach number (b) Aerodynamic centre as function of Mach number

Figure 3.19: NACA 64A-010 aerodynamic properties

value for all Mach numbers.

Besides the normal force coefficient and the aerodynamic centre as function of Mach number, also the total temperature and the total density at stagnation conditions have to be known. These values are necessary to obtain the density and temperature for each Mach number, from which the sonic velocity can be calculated. The total temperature and the total density at stagnation conditions are obtained from the wind tunnel properties which can be found in Section 2.3.

Aerodynamic Model The theory used for the aerodynamic model is the unsteady aerodynamic theory acting on a two-dimensional airfoil in a compressible flow from [34]. The indicial lift force is described following Theodorsen's theory [73], as a combination of two contributions: a non-circulatory and a circulatory term. The non-circulatory lift contribution represents the lift force produced due to the acceleration of the fluid over the airfoil. It is a time independent term and it only depends on the instantaneous acceleration of the fluid around the airfoil. In simpler terms, it represents the effect of the angular position of the airfoil. The circulatory term is time dependent, since the circulation around the airfoil changes with time. The vorticity that arises in the wake is created by the pitching velocity of the airfoil during the plunge motion.

In order to implement the transonic part for the forces, the normal force slope, and the location of the aerodynamic centre are given as a function of Mach number. This function is based on a spline and can be seen in Figure 3.19. The temperature and density for each Mach number are calculated by isentropic relations, which can be found in Section 2.3. The final aerodynamic model can be expressed in terms of a two-input, two-output system where the inputs are the angle of attack and the pitch rate $[\alpha, q]$ and the outputs are the unsteady normal force and the pitching moment coefficients $[C_N, C_M]$.

$$\dot{\bar{x}} = A\bar{x} + B \begin{Bmatrix} \alpha \\ q \end{Bmatrix} \tag{3.15}$$

$$\begin{Bmatrix} C_N \\ C_M \end{Bmatrix} = C\bar{x} + D \begin{Bmatrix} \alpha \\ q \end{Bmatrix} \tag{3.16}$$

A is a diagonal 8x8 matrix, B is a 8x2 matrix, C is a 2x8 matrix and D is a 2x2 matrix. All coefficients can be found in [30] and [34]. The $\bar{x}$ vector consists of eight state variables. These are the aerodynamic states that provide the information required at a given instant in time to allow the determination of future airloads, given future inputs in the airfoil motion [30].

Assumptions The assumptions implemented in the aerodynamic model are:

- The model is linear
- Elastic axis lies at a quarter chord point
- Tip vortices effects are negligible

Since the model that is used is a linearized model, it is only valid for small angles of attack. To provide a first order approximation of the aeroelastic behaviour of the model, the elastic axis is assumed to lie at a quarter chord. In addition, since the model does not account for wing tip vortices, their influence is neglected.

Aeroelastic Model The aerodynamic equations can be coupled to the equations of motion of an airfoil section with two degrees of freedom, using Equation 3.17 and Equation 3.18.

$$m\ddot{h} + S_\theta\ddot{\theta} + g_h\dot{h} + m\omega_h^2 = Q_h \tag{3.17}$$

$$S_\theta\ddot{h} + I_\theta\ddot{\theta} + g_\theta\dot{\theta} + I_\theta\omega_\theta^2\theta = Q_\theta \tag{3.18}$$

In the relations above, m is the mass, S_θ is the static mass moment, g_h and g_θ are respectively the structural damping in plunging and pitching, ω_h and ω_θ are respectively the uncoupled natural bending and torsion frequency and I_θ is the polar moment of inertia. Q_h and Q_θ represent the aerodynamic load and moment and are given in Equation 3.19. Finally, h is the plunging motion and θ is the pitch motion.

$$\begin{bmatrix} Q_h \\ Q_\theta \end{bmatrix} = \frac{1}{2}\rho V^2 \begin{bmatrix} -c & 0 \\ 0 & c^2 \end{bmatrix} \begin{Bmatrix} C_N \\ C_M \end{Bmatrix} \tag{3.19}$$

In this matrix, c is representing the local chord. To transform the second order differential equation into a first order differential equation, needed for the state space representation, the following z-states are defined that describe the structural behaviour.

$$z_1 = h, z_2 = \theta, z_3 = \dot{h}, z_4 = \dot{\theta}$$

The final equations of the coupled unsteady aerodynamics and the structural equations are:

$$[E] \begin{Bmatrix} \dot{\bar{z}} \\ \dot{\bar{x}} \end{Bmatrix} = [F] \begin{Bmatrix} \bar{z} \\ \bar{x} \end{Bmatrix} \tag{3.20}$$

The matrices $[E]$ and $[F]$ can be derived from the equations stated in [30].

Assumptions The assumptions implemented in the aeroelastic model are:

- No structural damping
- The uncoupled bending and torsional frequency obtained from Patran/Nastran are representative for the aeroelastic model

For a first order approximation of the response and stability of the model the structural damping of the model is assumed to be zero. This is done because it is difficult to describe and predict the structural damping of the model and can best be done experimentally. However, the model already accounts for structural damping as input and if the structural damping is known it can be added. The uncoupled bending and torsional frequency obtained by the simulation run in Patran/Nastran are assumed to be representative frequencies. Next, these frequencies are used to couple the structure and aerodynamic loads in the aeroelastic model.

3.4.2 Model Response

To determine the response of the model to a given input and its stability, the following three aspects are studied: structural response, flutter boundary and damping ratio.

The structural response to a given input is modelled. From this response, the time until the motion is damped out can be obtained, as well as the number of cycles until it damps out.

From the flutter boundary, the goal is to find the stability region for a range of Mach numbers. This is important because in the transonic flight regime, a so called transonic dip is present. The transonic dip is a local dip in flutter speed around Mach number of 0.8, which is caused by transonic effects. This can lead to an undamped oscillation (flutter). In order to perform a check of the stability of the model, the wind tunnel range, a range of velocities for different Mach numbers, is compared with the flutter boundary. To guarantee stability, the flutter boundary has to stay above the wind tunnel range.

Finally, from the damping ratio the behaviour and the influence of the stability of the modes can be foung. If the damping ratio of one of the eigenmodes become negative the model diverges.

To study these three aspects, the aerodynamic and the aeroelastic model are integrated. The integration of the aerodynamic and the aeroelastic model is illustrated in Figure 3.20. The inputs for the aerodynamic model are the Mach number, the velocity and the time, together with the initial angle of attack and the pitch rate. The aerodynamic model calculates the normal force and moment coefficients. To couple the aerodynamic forces with the structure in the aeroelastic model, some structural inputs are required. The structural inputs for the aeroelastic model are the mass, the static mass moment, the polar moment of inertia, the structural damping in both plunge and pitch, and the uncoupled bending and torsion frequency. The aeroelastic model calculates the plunge motion, the pitch angle and both their derivatives. Using Equation 3.21, the outputs of the aeroelastic model are converted into new inputs for the aerodynamic model.

$$\begin{bmatrix} \alpha \\ q \end{bmatrix} = \begin{bmatrix} \theta + \frac{\dot{h}}{V} \\ \dot{\theta}\frac{c}{V} \end{bmatrix} \tag{3.21}$$

Figure 3.20 represents how the aeroelastic model is build to obtain the response of the model. In the following paragraphs Figure 3.20 is explained.

Structural Response To model the structural response for a given Mach number, equation Equation 3.20 can be written into Equation 3.22.

$$\begin{Bmatrix} \dot{\bar{z}} \\ \dot{\bar{x}} \end{Bmatrix} = \left[E\right]^{-1} \left[F\right] \begin{Bmatrix} \bar{z} \\ \bar{x} \end{Bmatrix} \tag{3.22}$$

For the initial conditions, this equation can be directly integrated with respect to time using a standard ordinary differential equation (ODE) solver. The initial conditions can be an initial plunge

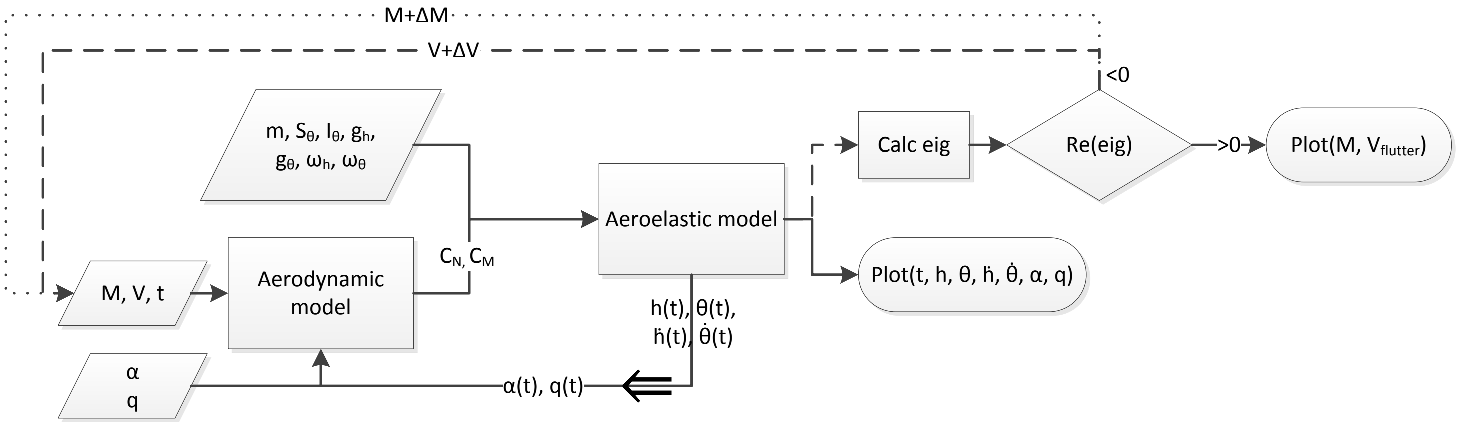

Figure 3.20: Flow block diagram of the aerodynamic and aeroelastic model

displacement (h), an initial pitch angle (θ), an initial plunge velocity ($\dot{h}$) and an initial pitch rate ($\dot{\theta}$), or a combination thereof. More details on how to actuate these input values can be found in Chapter 5, where the actuation system is explained. Since at initial conditions, the model is assumed to be fixed by the actuation system, there is no interaction between the airfoil motion and the aerodynamic loads. Therefore it is assumed that the aerodynamic state variables, $\bar{x}$, are zero. Summarized:

$$\begin{aligned} \bar{x}_0 &= [h_0\ \theta_0\ \dot{h}_0\ \dot{\theta}_0]^T \\ \bar{z}_0 &= [0\ 0\ 0\ 0\ 0\ 0\ 0\ 0]^T \end{aligned} \tag{3.23}$$

In Figure 3.20 the coupling of the aerodynamic model with the structures is illustrated by the feedback loop of $\alpha(t)$ and q(t) of the aeroelastic model back to the aerodynamic model. The final outputs to describe the structural response are the plunge motion (h), the pitch angle (θ), the plunge derivative ($\dot{h}$), the pitch angle derivative ($\dot{\theta}$), the angle of attack (α) and the pitch rate (q). The sign convention is that assuming that the flow comes from the left, the pitch motion is upwards and the pitch angle clockwise.

Flutter Boundary The speed where the system becomes unstable is the flutter speed. The flutter boundary is a curve connecting all flutter speeds, at which a damped oscillation transitions to an undamped oscillation. The flutter boundary can be found by analysing the eigenvalues of the final coupled state-space system representation, see Equation 3.23. If the real part of one of the eigenvalues is higher than zero the system becomes unstable. In Figure 3.20, it is illustrated how to obtain the flutter boundary.

To find the flutter boundary, the initial velocity and Mach number are taken as zero. The eigenvalues of the final coupled state-space system representation given in Equation 3.23 are calculated with $eig(\left[E\right]^{-1}\left[F\right])$. The eigenvalues have the form of: $\lambda_k = \sigma_k + i\omega_k$. If all real parts of the eigenvalues (σ_k) are smaller than zero, the velocity is increased by ΔV and the eigenvalues are calculated again. This continues until one real part of the eigenvalue is larger than zero. This point is the flutter speed. If the flutter speed is found, the Mach number is increased by ΔM and the velocity is set to zero again. The procedure is repeated for the new Mach number. The Mach number is increased until a specified value. Finally the flutter boundary is obtained and plotted.

Next, in the same graph, the wind tunnel range is plotted. This is the range of velocities that the wind tunnel can achieve for different Mach number. The wind tunnel range is obtained by making the temperature dependent on the Mach number and the total temperature. The total temperature can be found in Section 2.3. Finally, Equation 3.24 is used to calculate the velocity range that the wind tunnel can achieve.

$$V = M\sqrt{\gamma R \frac{T_0}{1+\frac{\gamma-1}{2}M^2}} \tag{3.24}$$

To obtain stability, the flutter boundary must stay above the wind tunnel range. The point at which the system becomes unstable is when the flutter boundary moves below the wind tunnel range. This point is called the Mach number at flutter speed.

Damping Ratio The damping ratio for a certain Mach number can be calculated from the eigenvalues that correspond to the final coupled state-space system given in Equation 3.23. The corresponding damping ratio associated with each aeroelastic mode is given by Equation 3.25.

$$\zeta_k = -\sigma_k/\sqrt{\sigma_k^2+\omega_k^2} \tag{3.25}$$

As can be seen from Equation 3.25, for a positive real eigenvalue the damping ratio becomes negative. This results in an undamped oscillation. If the eigenvalue only consists of a negative real part, the damping ratio is one. If the eigenvalue consists of both a negative real part and imaginary part, the damping ratio is between zero and one. In general, twelve eigenvalues are found. Six of these eigenvalues consist only of a real part. The other six eigenvalues consist of one complex pair that has a low frequency and is highly damped. This is the torsional mode that is coupled with the unsteady aerodynamics. The other of two complex pairs contain the structural modes: bending and torsion modes. The bending mode has in general a lower frequency than the torsion mode and is also less damped. Often the bending mode is the mode that becomes unstable.

3.4.3 Aeroelasticity Interference

To provide the experimental data for the FSI solvers in the transonic regime, it is important to relate the structural parameters to the aeroelasticity. One of the phenomena related to the interference is called flutter. Also, specific for the transonic regime, a transonic dip is present. This transonic dip, causes a dip in the flutter boundary and therefore constraints the operating velocity range. The procedure to obtain the flutter boundary can be found in Section 3.4.2. When flutter occurs, the model before any intervention is possible. Therefore, this phenomenon must be avoided.

In this section, the relation and interference between the structure and the aeroelasticity is explained. This is done by qualitative relations. The approach is based on a 'ceteris paribus' approach. This means that one input variable is changed and the rest of the input variables remain fixed.

In Equation 3.26 until Equation 3.30, the relations and interference of the structure with the aeroelasticity are given. All relations start with a structural input parameter that is varied. By varying the structural input parameters, the five parameters related to the structure of the model decrease or increase. The first two parameters are the first natural frequency for bending and torsion. The remaining three parameters are the buckling factor, the deflection as percentage of the length and the von Mises stress. All these parameters are obtained by a simulation run by Patran/Nastran. The first natural frequency for bending and torsion are inputs for the aeroelastic model. By applying the updated varied structural input parameters, the first natural bending and frequency in the aeroelastic model, the behaviour of the system can be observed. These parameters are the time until the response is damped out and the stability of the model. The time until the system is damped out until the response is within 1% of its final steady state value, can be obtained from the response of the model. The stability of the model is directly related to the flutter boundary. When the flutter boundary of the model increases with respect to the wind tunnel range limit, the system becomes more stable, see

Table 3.2: Parameter clarification

	Symbol	Name	Unit
Varying Structural input parameters	t_{skin}	Skin thickness	$[m]$
	c	Chord	$[m]$
	L	Length	$[m]$
	$\rho_{material}$	Density structural material	$[kg/m^3]$
	E	Young's modulus	$[GPa]$
Structural parameters	ω_h	First natural bending frequency	$[Hz]$
	ω_θ	First natural torsional frequency	$[Hz]$
	bf	Buckling factor	$[-]$
	δ	Deflection as percentage of length	$[\%]$
	σ_{vm}	von Mises stress	$[MPa]$
Model response	T_{damp}	Time until response is damped out	$[m]$
	Stability	Stability of the model (flutter boundary)	$[-]$

Section 3.4.2. In short, if the stability increases, the Mach number at which flutter occurs, increases. In Table 3.2, all the parameters are given.

$$t_{skin} \uparrow \Rightarrow \omega_h \downarrow , \ \omega_\theta \uparrow , \ bf \uparrow , \ \delta \downarrow , \quad \sigma_{vm} \downarrow \quad \Rightarrow T_{damp} \downarrow , \ Stability \uparrow \tag{3.26}$$

$$c \uparrow \Rightarrow \omega_h \uparrow , \ \omega_\theta \downarrow , \ bf \uparrow , \ \delta \downarrow , \quad \sigma_{vm} \downarrow \quad \Rightarrow T_{damp} \downarrow , \ Stability \uparrow \tag{3.27}$$

$$L \uparrow \Rightarrow \omega_h \downarrow , \ \omega_\theta \downarrow , \ bf \downarrow , \ \delta \uparrow , \quad \sigma_{vm} \uparrow \quad \Rightarrow T_{damp} \uparrow , \ Stability \downarrow \tag{3.28}$$

$$\rho \uparrow \Rightarrow \omega_h \downarrow , \ \omega_\theta \downarrow , \ bf \downarrow , \ \delta[-] , \ \sigma_{vm}[-] \quad \Rightarrow T_{damp} \uparrow , \ Stability \downarrow \tag{3.29}$$

$$E \uparrow \Rightarrow \omega_h \uparrow , \ \omega_\theta \uparrow , \ bf \uparrow , \ \delta \downarrow , \quad \sigma_{vm} \downarrow \quad \Rightarrow T_{damp} \downarrow , \ Stability \uparrow \tag{3.30}$$

In Equation 3.26 until Equation 3.30, the upward arrows indicate if the parameter increases or decreases. When a [-] is given, this parameter remains unchanged. The right pointing double arrows split the three groups, given in Table 3.2. The first right pointing double arrow is put after the varied structural parameter that is either decreased or increased. After this arrow, all structural parameters are given. Next, the second double arrow is given, after which the parameters for the model response is given. Based on these qualitative analysis, a better understanding of the interference between the structures and the aeroelasticity is obtained and will have an impact on the final design.

3.5 Final Design

After the procedure described in the previous sections is followed to its conclusion, a final design is achieved for the model. In Table 3.3, the properties of the design are listed. Table 3.4 displays the chosen material's characteristics and mechanical properties. In Appendix B, a CAD-drawing of the model is presented, and Figure 3.21 shows a render of the final shape, with the tip left open to show the interior shape of the model.

The airfoil is chosen in Section 3.1. The structural shape follows from the discussion in Section 3.3.1, and since it is the most simple shape to manufacture and it provides the necessary structural properties, a hollow shell is chosen. The length is defined by wind tunnel integrity and flow interference factors, described in Section 3.2.1. The sweep and taper are picked for the reasons described in Section 3.2.3 and 3.2.4, respectively. Finally, from the iterative process followed for the design, shown in Section 3.3, the opimal chord length, skin thickness and material are found.

Table 3.3: Final model design

Airfoil	NACA 64A-010
Structural shape	Hollow shell
Length	$0.23m$
Sweep angle	$0°$
Taper ratio	1
Chord	$0.15m$
Model thickness	$0.015m$
Skin thickness	$0.003m$
Material	Chopped roving (glass fibre) reinforced polyester
Manufacturing process	Molded spray-up laminate
Mass	$0.409kg$
1st bending frequency	$70.29Hz$
2nd bending frequency	$294.02Hz$
1st torsional frequency	$242.25Hz$
Max. deflection at max. load	7.7% of length, $0.018m$
Max. von Mises stress	$63.7MPa$
Buckling margin factor	2.0352
Flutter margin	9.431%
Time to damp oscillation ($\theta_0 = 3.6°$)	$0.026s$

Table 3.4: Material properties

Base (resin)	Unsatured polyester (thermoset plastic)
Filler	Glass fibre
Fibre volume content	50%
Density	$2,100kg/m^3$
Young's modulus	$6.3GPa$
Poisson's ratio	0.342
Yield strength	$166MPa$
Minimum service temperature	$246K$

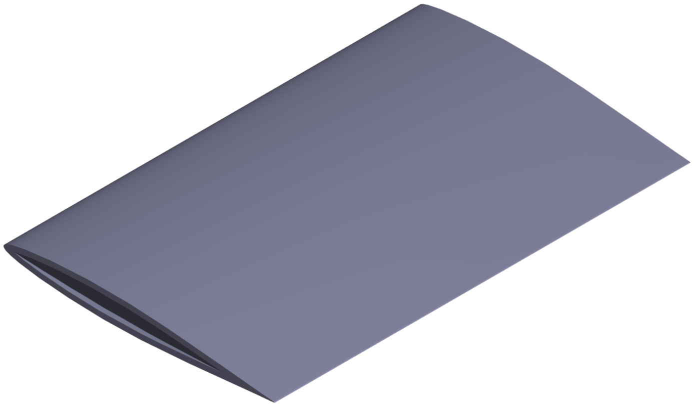

Figure 3.21: Render of the final model

3.6 Model Production

The model is manufactured in three main steps. The first step is to create the required parts of the model. The second step is further processing of the parts to meet the requirements. The last step is the assembly of the model from the finished parts.

3.6.1 Manufacturing Technique

The model is made of polyester with chopped glass fibre rovings as a means for reinforcement. For this material, several types of manufacturing procedures are available, all suitable for the creation of a single model instead of mass production. These techniques are wet lay-up, spray-up, the use of a vacuum or pressure bag and RTM [10].

These methods are limited to producing one side of the model, as they cannot be used to create hollow models. This means that the model needs to be created in three parts. The first two parts are the upper and lower skins, which at a later stage are combined to form the complete skin of the model. The last part is a flat plate which is used to seal off the tip of the model, thereby creating a closed structure. This flat plate is manufactured individually as sharp edges are difficult to manufacture and the mould is more difficult to create.

Wet Lay-up Wet lay-up, also known as hand lay-up, uses an open mould, rollers and a spray gun. The process is started by applying a gelcoat on the mould and letting it cure, which forms a smooth surface finish. This smooth surface is required on the outside of the model to meet requirement M3, describing the surface roughness, as stated in Table 1.1. Therefore a female mould is used, as this means that the gelcoat is on the outside surface of the model. After this preparation, the resin is applied on the mould. Next, the reinforcement is added using a spray gun, which chops the glass fibre rovings and sprays it over the resin in the mould. After the reinforcement is added, a roller is used to squeeze out excess resin and to ensure the resin is distributed evenly throughout the reinforcement. The process of adding a layer of resin, spraying on the reinforcement and rolling can be repeated until the desired thickness is achieved. After this, the moulded part is left to cure, which can be done without any applied pressure or heat [38].

The advantages of this method are that it requires a limited amount of equipment, it is inexpensive and it is economically suitable for the creation of a small number of products. The disadvantages are that the process is labour-intensive, the tolerances depend on the skill of the operator and there are health concerns, since this process uses an open mould.

Spray-up The spray-up process is similar to wet lay-up, as it also requires an open mould, rollers and a spray gun. The main difference is that the resin and the reinforcement are sprayed on the mould at the same time. A second difference is that this process is used exclusively for chopped rovings, whereas for wet lay-up it is just one of the available options, as generally woven fabrics are used. A female mould is used for the same reasons as for wet lay-up. The spray-up process is started by applying a gelcoat on the mould. After the gelcoat has cured, both the resin and reinforcement are applied at the same time by using a spray gun. This spray gun chops the rovings to the desired length and mixes the chopped rovings and resin within its spray. The spraying is interspersed by rolling out the resin, to ensure evenly distributed material and to remove any excess resin. The spraying and rolling is continued until the desired thickness is achieved.

The advantages of this process are that it requires a limited amount of equipment, it is inexpensive, it is suitable for the creation of a small number of products and it creates a product with uniform properties. The disadvantages are that the tolerances depend heavily on the skill of the operator, the ratio between resin and reinforcement is difficult to control and there are health concerns, because of the use of an open mould.

Vacuum or Pressure Bag Wet lay-up and spray-up can both be expanded by the use of a vacuum or pressure bag. This process is identical to the original process until the point where the moulded part is left to cure. At this point a bag is laid over the mould. In case of a vacuum bag, the air is pumped from underneath the bag. In case of a pressure bag, the bag is pressurised by air. Both methods apply pressure during the curing and both methods require a pump as an additional tool.

The advantages of using this process are that the curing takes less time due to the higher pressure, the moulded part is denser as this method reduces the amount of trapped air and it ensures that the moulded part retains the shape of the mould during curing. The disadvantages are that more labour is required for implementing this process and that the costs are slightly higher.

Resin Transfer Moulding RTM requires a preform, which shapes the reinforcement in the desired shape. This preform is created by using a similar process as spray-up, but a binder instead of a resin is used. There is a need for a preform in RTM, as in the following step resin flows through the mould cavity. If no binder is used, the resin flow aligns and moves the glass fibre strands, creating non-homogeneous material properties. Once the preform is created, it can be used for RTM. This process requires both a male and a female mould. The preform is clamped in the mould cavity. Pressure and heat is applied when the resin is injected through multiple ports. The model is left to cure under pressure.

There are several advantages to this process. The mould itself can be created inexpensively, since the process requires low pressure compared to other closed mould processes. The use of two moulds also allows for having a smooth surface on both sides of the product, adding more detail, like ribs or holes, and for smaller tolerances. This reduces the costs of the manufacturing at a later stage. Another advantage is that less health risks are present during the manufacturing, since the mould is closed. There are also several disadvantages. This process requires additional equipment, such as a press and a system to inject the resin. Furthermore, the entire moulded part needs to be evenly impregnated by the resin, which requires a detailed design of the number and the locations of the injection ports in the mould.

3.6.2 Trade-off for Manufacturing Process

The three criteria which are used to select a manufacturing method are: cost, complexity and tolerances of the moulded part.

Requirement M4, as stated in Table 1.1, requires the model to be manufactured with a tolerance of at most $0.1mm$. RTM is able to achieve lower tolerances than spray-up and wet lay-up, however, the skin thickness tolerance of $0.2mm$ means RTM is not able to meet this requirement directly after moulding. Both spray-up and wet lay-up are able to achieve a skin thickness of $0.51mm$. This means that all processes require further refining of the moulded part. Effectively, this means the effect of the lower achievable tolerance for RTM is not as large as expected. Furthermore, the technique is significantly more complex, since it requires detailed modelling of the resin flow. Lastly, the costs are higher, since it requires a more expensive mould. Therefore, this process is not used. Spray-up and wet lay-up are similar processes, since the costs, complexity and achievable tolerances are almost identical. The main difference is that spray-up requires less time and creates more homogeneous properties in the moulded part. Furthermore, since the achievable tolerances depend heavily on the skill of the operator, it is preferred not to use wet lay-up, which is generally used with woven fibres instead of chopped fibres. Therefore, spray-up is used to manufacture the model. Since a vacuum or pressure bag offers important benefits, such as a denser material and the moulded part deforms less during curing, the choice is made to make use of this technique.

3.6.3 Manufacturing of the Mould

The mould is created from an inexpensive material which can be machined to the dimensions required for the model, such as wood. The manufactured model must have tolerances of less than $0.1mm$, as stated by requirement M4 in Table 1.1. Therefore, the mould needs to be checked extensively to ensure that the model meets this requirement. It is important that the surface is as smooth as possible, as any imperfections of the mould transfer directly to the part that is created. The mould is used twice, as both halves of the model are identical, thus it is important to apply a coating to the mould to ensure that the surface of the mould suffers no damage during manufacturing.

3.6.4 Processing

After both halves of the model are created, further processing is required. A set of holes needs to be drilled to place the pressure transducers. During the drilling of these holes, the cutting speed must not be too high to prevent reaching the temperature at which the polyester disintegrates.

Requirement M3 states that the surface roughness needs to be at most $0.20\mu m$. This requirement cannot be achieved directly by the mould, therefore, the surface roughness needs to be decreased afterwards. For this a lapping film is used, which is able to lower the roughness to the desired value. Even though lapping film is generally used for polishing optical fibre connections, lapping films that can be used for composites are also available.

Requirement M4 states that the manufactured model must have tolerances less than $0.1mm$. However, using spray-up the thickness tolerance is $0.51mm$. Therefore, the inside of the model needs to be machined to achieve this skin thickness tolerance. However, this is a labour-intensive process. The outside dimensions of the model depend on the mould and therefore meet the requirement.

3.6.5 Assembly

The last step in the manufacturing process of the model is the assembly. For the assembly of the two halves of the model, an adhesive is used. For the chosen material, the most suitable adhesives are acrylic, polyurethane, epoxy and polyester. The drawbacks of acrylic adhesives are that these need to be cured by use of heat or light and they are normally only used for high-volume production. Polyurethane is used for glass fibre reinforced plastics, but it is not used in parts where a high strength is required. Epoxy and polyester adhesives do not suffer from these drawbacks and are therefore the remaining options. The properties of polyester and epoxy are similar. Epoxy generally provides a higher strength, whereas polyester generally is less expensive and more flexible. The properties depend heavily on the composition of the adhesive, which is why no choice between polyester and epoxy is made [57].

The surfaces must be clean and dry to ensure proper bonding of the two parts. When this is the case, the adhesive is applied. Care must be taken so that the adhesive forms an air-tight seal to prevent any interference during the experiment. The adhesive is then left to cure.

Chapter 4 — Mount

In order to attach the model to the wind tunnel, a mount is required. The mount is designed to meet the requirements defined in the RDT in Table 1.1. The requirements that have an effect on the mount or are affected by the mount are listed below and grouped into three sets.

The first three requirements (D1.1.2, D1.1.3 and D2.3) influence the mount, by describing the different structural eigenfrequencies required. Due to the downsizing of the model in the wind tunnel, the eigenfrequencies increase. Nevertheless, the measurement techniques must be able to measure the behaviour of the model in combination with the mount.

The next set of requirements (D2, D2.2.1, D2.2.2, E6 and M6) describes the aeroelastic effects that need to be present and the required behaviour of the structure. The occurrence of certain phenomena can be triggered and controlled by the mount by optimizing it. Also, the maximum deflection can be controlled by sizing of the mount.

Finally, the last set of requirements (D2.6, E1.2, M2 and M5) describes the effect of the structure on the flow in the wind tunnel. Since this dataset will be used to validate FSI solvers, it is important to be able to model the experiment in the solver. This is also taken into account when choosing a mount option. Lastly, the interaction of the mount with the model and the airflow is an important part of the sizing of the mount.

4.1 Design Options

The first step in the design of the mount is the selection of the mount type. The mounts that are considered for the wind tunnel experiment are listed below. In this section, all of these options are briefly discussed.

- Clamped support
- One or multiple strut supports
- Sting support
- Wire support
- Pitch and Plunge Apparatus (PAPA)
- Nonlinear Aeroelastic Testbed Apparatus (NATA)

Clamped Support Clamping the model in the wind tunnel wall restrains the model from moving in all six degrees of freedom. The advantage of this mount is that it is very easy to produce and it contains no moving parts. Having no movement, the simple structure allows for wiring to run from the model, inside the tunnel, to the outside of the tunnel. Additionally, the flow disturbance due to the mount is small and the mount does not induce any blockage effect, since it does not have any structural parts in the wind tunnel. However, the downside is the lack of flexibility in the design of the mount. The mount cannot be used to influence any eigenfrequency of the model and it does not have any influence on the maximum tip deflection.

Strut Support A strut support containing one or multiple struts allows a complete structure to be mounted inside the tunnel. The advantage of this support is the easy control of the angle of attack. However, since struts introduce a large blockage area, this mount type will not be considered.

Sting Support A sting support mounts the model inside the tunnel using a structure downstream of the model. Just like a strut support, this introduces a blockage in the test section. However, since the mount is behind the model, this does not affect the test section and does not add up to the blockage of the model. The advantage of a sting over a clamp is the ability to mount a complete model in the

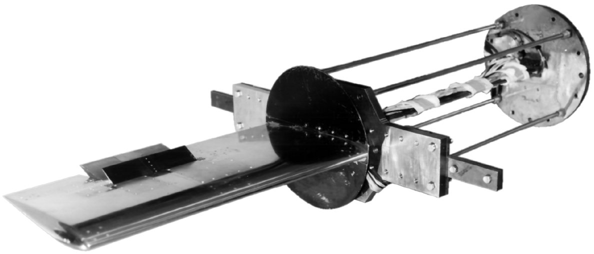

Figure 4.1: Pitch And Plunge Apparatus mount [67]

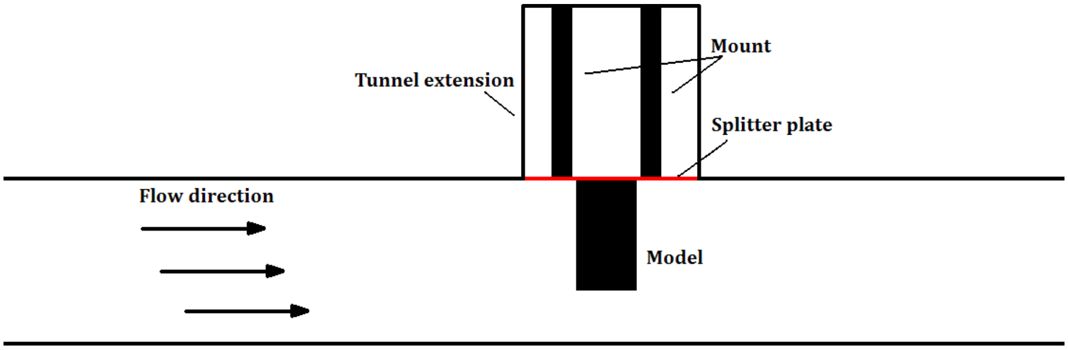

Figure 4.2: Wind tunnel extension and splitter plate

centre of the wind tunnel. However, since only a half-span wing is considered in this experiment, the clamp is preferred over a sting support. Therefore, a sting is not considered either.

Wire Support A wire support holds the model in place using wires. Since wires can only be loaded in tension, they have to be placed upstream of the model, disturbing the airflow. Wires also allow for movement of the entire model, which is not desired. Since a half wing span is considered, one end is to be clamped. Therefore, a wire support will also not be used in this experiment.

Pitch and Plunge Apparatus A PAPA mount is formed by connecting the model to the wall with four rods, as can be seen in Figure 4.1. The rods are clamped at both ends. Due to the spacing between the rods, the rods mainly have a tip deflection instead of rotation. This results in a larger in-plane rotation of the plate connecting the rods to the model, but negligible translation and out-of-plane rotation. This mount type has been used before by NASA in their Benchmark Models Program [67]. The PAPA mount is designed to study aeroelastic phenomena, such as flutter and provides a high level of frequency control. This is done by altering the mount dimensions, i.e. the thickness of the rods, and varying the mass. Also, the eigenfrequencies for the pitching and plunging motion can be controlled separately. The dimensioning may also be used to meet deflection requirements. The downside of this mount is the required space to implement the structure. This can however be solved by extending the wind tunnel with a section containing the mount. A splitter plate ensures minimum interaction between the mount and the flow. It is mounted directly on the tunnel. A sealed bearing ensures the motion of the mount and model are not influenced by the splitter plate. This configuration using an extension is shown in Figure 4.2.

Nonlinear Aeroelastic Testbed Apparatus The NATA mount consists of two sets of springs, as can be seen in Figure 4.3. By changing the spring stiffness, the first set of springs is used to control the plunging frequency while the second set of springs controls the pitching frequency. This mount was

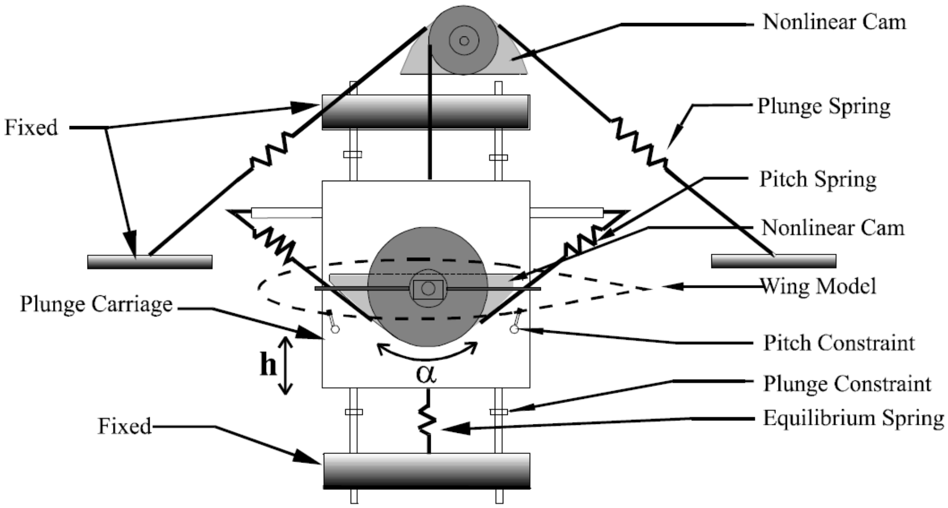

Figure 4.3: Nonlinear Aeroelastic Testbed Apparatus mount [69]

developed and used at the Texas A&M University for the investigation of aeroelastic responses. The advantages are the same as for the PAPA mount, with the added benefit that it requires less space than the PAPA mount. The disadvantage, however, is that it is much more difficult to prevent the airflow from being disturbed by the mount.

4.2 Mount Trade-Off

A clamp, a PAPA mount and a NATA mount are considered for the final design of the experiment, based on their advantages over the other mount options. The selection of the mount for the final model depends on a trade-off based on several criteria, being complexity, flexibility, flow interference, relevance, accuracy, cost, risk and sustainability.

Complexity The complexity of the mount is divided in three parts. The first part contains the required level of optimization and the complexity of the structural analysis. The second part describes the ability to integrate measurement devices, since wires have to go from the model to a receiver outside the tunnel. Finally, manufacturing complexity follows from the structural analysis and optimization.

Flexibility The flexibility of the mount is the ability to design and optimize the structure for its structural behaviour. A clamp cannot be optimized or changed, since it is a fixed support for the model, restricting any degree of freedom. The PAPA and the NATA mounts both can be modified by means of structural and spring optimization respectively.

Flow Interference The next criterion is the interference of the flow in the test section. Since the experiment is used to provide validation data for FSI solvers, it is desired to avoid creating any disturbance in the flow due to a complex mount, since it has to be modelled in the solver. A simple clamp causes the least flow disturbances and therefore is the easiest to model. A splitter plate makes sure this effect is minimized for the PAPA and the NATA mount, but the interaction is still higher than when using a clamp.

Relevance Relevance describes how well the mount can be applied in the validation of general FSI solvers. It also describes to what extent the mount can simulate the actual behaviour of a real wing. This can be decomposed into the ratio between pitching and plunging frequencies, the actual

Table 4.1: Mount trade-off

	Complexity	**Flexibility**	**Flow interference**	**Relevance**	**Accuracy**	**Cost**	**Risk**	**Sustainability**	**Normalized total score**
Weight	17.3%	15.8%	17.8%	15.9%	6.9%	18.9%	4.6%	2.8%	
Clamp	10	1	7	3	9	9	10	8	38
PAPA	2	10	5	7	8	4	7	5	32
NATA	2	8	6	9	5	5	7	5	30

deformation of the mount and the model and the damping of motion. Both the PAPA and the NATA mount are able to represent the behaviour of a real wing. The clamp on the other hand is much easier to implement in a FSI solver for validation purposes.

Accuracy The accuracy describes the ability to predict the behaviour of the mount during the design phase of the experiment. It is the ability to analytically or numerically analyze the mount, without having performed the actual experiment. A clamp can easily be modelled and analyzed both analytically and numerically. Since the NATA mount uses a spring damper system, this is also easily analyzed at a high level of accuracy. Because the PAPA mount is a highly complex structure, it can only be analyzed accurately using numerical Finite Element Method (FEM) software. Since this is an approximation, the level of accuracy is lower and the actual behaviour during the experiment might differ slightly from the prediction.

Cost The cost criterion is mainly determined by the human resources required to optimize the structural behaviour of the mount and the integration of the mount in the tunnel. Since the PAPA requires most time, this mount is graded the lowest, whereas the clamp is graded much higher, since it does not require detailed designing. A very small part of the cost criterion is the use of material and the manufacturing due to the structural complexity. This is a large part of the overall experiment cost, but a small part of the trade-off, since it is considered to have a small influence on this trade-off compared to the human resources. Based on the complexity of the structural parts, the costs for the NATA mount are estimated to be slightly higher than for the PAPA mount.

Risk Risk is used to describe the chance that failure occurs. The consequence of this failure is not taken into account, since it is considered the same for each option. Failure is defined as structural failure, such as rupture or buckling of the mount or model. The clamp is not expected to allow for any kind of failure, whereas the PAPA and the NATA mount contain parts that might fail. However, this failure is not expected to be very likely.

Sustainability Finally, sustainability is based on the amount of material required for the design combined with the complexity of the parts in the mount. Complex parts mostly require more energy during manufacturing. Both the PAPA and the NATA mount require more material and more parts than a simple support.

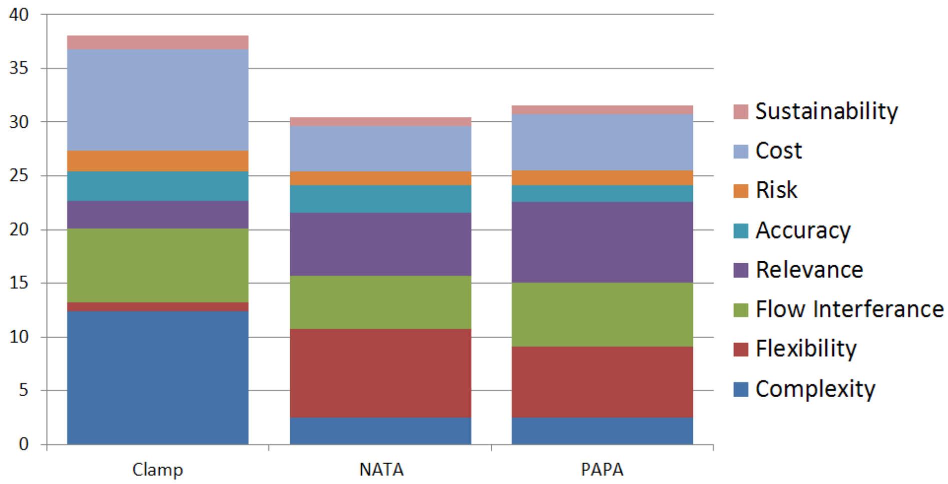

Figure 4.4: Mount options trade-off

Trade-off For all the criteria, the mounts are graded on a scale of one to ten, one being the lowest and ten the highest. Also each criterion is given a weight. This weight is determined using the D-sight decision making software [9]. All criteria are compared to each other in a pairwise comparison. This is based on their mutual importance. The software determines the weighting factors based on these mutual importances. For each criterion, the grades are normalized by dividing the grade by the sum of the given points. This normalized grade is multiplied by the weighting factor of the criterion. The sum of this value for all criteria gives the final score for the mount. All grades and the total scores are given in Table 4.1. Figure 4.4 shows the contributions of all criteria grades to the final scores. From the trade-off follows that a clamped mount is the best solution for the experiment. The PAPA and the NATA mount have a large contribution in the score based on flexibility and relevance. However, the complexity and the cost of the clamp over the PAPA and the NATA mount made it the best option.

4.3 Detailed Design

Since clamping the model satisfies all stated requirements, and since the trade-off rated the clamp highest, the model is mounted inside the wind tunnel using a clamp. This is based mainly on its simplicity and cost. In Figure 4.5, the side of the TST-27 wind tunnel test section is shown. The wall consists of a steel with glass ring, which is replaced by a solid steel ring, in order to place the clamp.

The inner ring of the mount contains a solid disc which is connected to the outer ring by bolts. This configuration allows the model to be mounted at various angles of attack. The model is positioned at its new angle of attack when the wind tunnel is not running. In Figure 4.6, an exploded view of a simplified version of the mount is shown. In the centre of the inner part, the shape of the model is cut out, in order to clamp the model properly and be able to seal the wall of the tunnel. Finally, the outer ring is connected to the wind tunnel using bolts.

The outer ring has an outer diameter of approximately $46cm$, the same as the current tunnel window. The inner diameter varies from $20cm$ inside the tunnel, to $18cm$ on the outside. This slope in the inner part of the ring allows loads induced on the mount to be transferred to the wind tunnel. The thickness of the ring is $4cm$. The thickness is over-dimensioned, to ensure no failure of the wind tunnel structure occurs and to prevent the mount from deforming. Bolts are used to fasten the ring to the tunnel.

The inner ring is designed to fit exactly in the inner space of the outer ring. The thickness of this ring is also $4cm$, based on over-dimensioning to ensure its structural integrity. The diameter also varies from $20cm$ inside the tunnel, to $18cm$ on the outside. Additionally, the ring has a flange of $1cm$

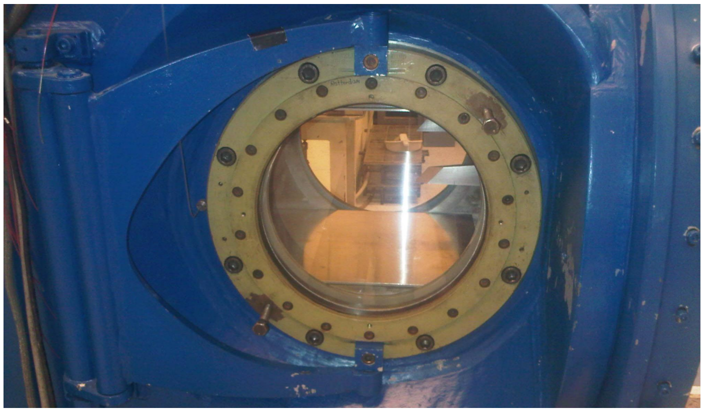

Figure 4.5: Side of the TST-27 wind tunnel test section

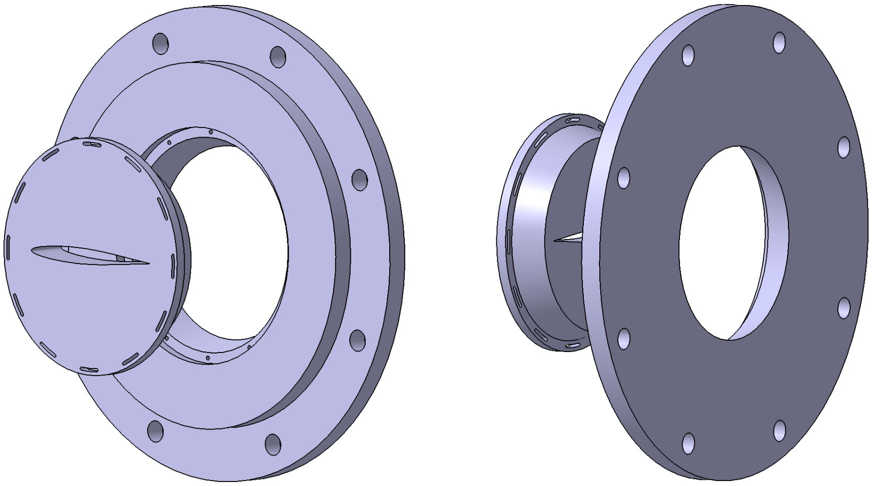

(a) As seen from the inside of the tunnel (b) As seen from the outside of the tunnel

Figure 4.6: Exploded view of simplified mount

thickness and extending the radius of the ring by $1cm$. This flange is used to fasten the inner to the outer ring. The flange is cut out of the outer ring, to ensure a perfect fit and a flat, smooth surface inside the tunnel. In the flange thin slots are drilled, through which bolts attach the ring to the outer ring. The slots allow for fastening at different angles of attack. In the center of the inner ring the exact shape of the model is cut out. The model is clamped in this slot and sealed from the outside of the tunnel.

Chapter 5 — Actuation

As discussed in Section 3.4.2, to obtain the desired aeroelastic behaviour, an oscillation must be initiated by an initial deformation of the model. There are several possibilities to obtain this deformation. In this chapter, the options regarding the actuation of the model are considered. One of these options is then selected and is discussed in more detail.

5.1 Actuation Choices

There are two main ways to actuate the model. Either the structure can be deformed or the flow upstream can be disturbed. Different options based on these two principles are presented hereafter. For the options that deform the model, the following are considered: an actuated flap, a deforming bar, a rotating clamp, a torsional rod, a wing integrated excitation system and a gear. Only one way was found to disturb the flow: moving a flap in the wind tunnel upstream of the model.

5.1.1 Important Considerations

Some parameters are considered to compare the different options in detail before any option can be presented.

The most important parameter for all the options that are considered, is their accuracy. It is extremely important to know the exact behaviour of the actuator that is used on the model and whether it indeed introduces a vibration in the model that leads to a measurable response of the model. The reason for this is that the actuator has to be modelled within the FSI solver to accurately validate this solver. Therefore, if there are large inaccuracies in the knowledge of the actuator's behaviour, uncertainties are introduced in the FSI solvers.

The cost is another parameter for each of the options. Since the overall budget is €50,000, the cost of the actuator must be minimised, while retaining the highest possible accuracy.

Finally, the installation of the actuator within the experiment is also considered. This includes whether the actuator is positioned inside or outside of the model. Regardless of where the actuator is positioned, it has to be accounted for.

5.1.2 Flap

To initiate oscillations of the model in the wind tunnel, a flap can be used. This flap is extended and retracted to induce oscillations by generating additional lift for a short period of time. The flap can be positioned anywhere on the model, however, positioning it closer to the tip results in a larger moment about the root. This in turn means that a smaller flap surface is required. Since the model has a small maximum thickness, it is complicated to implement an actuation mechanism for the flap. If a flap is integrated with the trailing edge of the model, less space is available than if it is to be positioned at the location of the maximum thickness. If it is positioned at the location of the maximum thickness, it is called a spoiler instead of a flap. In Figure 4.1, a typical example of a spoiler of a wing model is shown. To actuate the flap, different options are possible. The actuation mechanism (motor) can be placed either inside the model or outside of the model and wind tunnel. Having it outside requires a system, possibly cables, that runs through the model to push and pull the flap, whereas positioning it inside the model requires a sufficiently small actuation mechanism.

A flap has a number of advantages. One of these is that the flap can be controlled remotely. Also, since the flap is small compared to the model, a small motor can suffice to actuate the flap. Possible motors able to fulfill this are an electric motor, such as a servo or a stepper motor, a pneumatic or hydraulic actuator or a piezoelectric bender. The latter is a material which bends when a current runs through it.

The cost of this kind of mechanism mainly consists of the cost of the motor and the cost of manufacturing the flap. The motors are available for a price starting at approximately €20, whereas the creation of the flap includes the costs of cutting out an existing part of the model and integrating this with a hinge and motor. Therefore, the manufacturing costs are considered to be low.

Several disadvantages of a flap mechanism can be identified. First of all, the model is made of polyester. Creating a hinge that integrates with a polymer model can be cumbersome. Depending on what material the hinge is made of, there is a high chance that the loads acting on the hinge through the flap are too high, resulting in a failure of the flap. Furthermore, positioning the actuator inside the model changes the moment of inertia of the model and this in turn changes the natural frequencies of the model.

To size the flap, the influence it has on the flow needs to be known. For this, a CFD analysis is required and therefore, a more detailed sizing of the flap actuator is left for further research. It is however, possible to perform an estimation of the flap size by analytically calculating the increase in lift on the model due to the flap using the Javafoil applet [22]. From this increase in lift, the deflection of the model can be calculated.

5.1.3 Deforming Bar

A deforming bar is a small bar which is positioned inside the model. This bar can either bend or twist the model depending on its orientation within the model. To make this bar deform the model, it needs to be made of either a piezoelectric material or, contain a magnetorheological fluid.

The former is a piezo bender, a material that bends when a voltage is applied to it. An advantage of piezo benders is their response time, which is in the order of milliseconds. They also have a very precise position control of less than 0.5% [56]. A downside of piezo benders is that they have a very low blocking force. This is the force at the tip of the bender to prevent it from displacing. For piezo benders this blocking force is found to be in the order of magnitude of a few Newtons, meaning it is not strong enough to bend to model.

A magnetorheological fluid is a fluid that becomes solid when subjected to a magnetic field. The particles in the fluid align themselves with the magnetic flux. This fluid can be positioned inside a flexible rod, which deforms when a magnetic field is applied. An advantageous characteristic of this fluid is that its yield stress can be controlled accurately by varying the intensity of the magnetic field, also the response time to changes in the magnetic field lie within a few milliseconds [29]. A disadvantage of this fluid is the fact that it has a very low maximum shear strength, namely in the order of $100kPa$. Due to this, the material fails during the wind tunnel experiment.

5.1.4 Rotating Clamp

Another option to induce an oscillation of the model is to move the mount. This involves a rotation of the entire mount. The model is connected to the mount which in turn is connected to the actuation system. To realise this way of actuation, a sufficiently strong, accurate and highly responsive motor is required to turn the mount and model back and forth within a small time interval. The advantage of such a system is that no components have to be placed inside the model. Possible motors that can fulfill this are a stepper motor or an electro-hydrostatic actuator.

A stepper motor is an electric motor that divides a full rotation into a number of steps. The motor can hold at one of these steps, meaning it can maintain the position of the model at a fixed point. Stepper motors are available in different sizes, each producing a different maximum torque. The cost of a stepper motor varies from a few hundred euros up to €2000, therefore a computation of the torque necessary to rotate the model is required to select an appropriate stepper motor. The precision of a stepper motor is based on how precise its step angle is. Typically the tolerance for this is ±5% [53].

The electro-hydrostatic actuator uses a high-powered stepper motor to drive a reversible pump. This pump pressurizes a working fluid. This working fluid raises the pressure in a cylinder to which the pump is connected resulting in it to move. This system is typically used in aircraft to move control

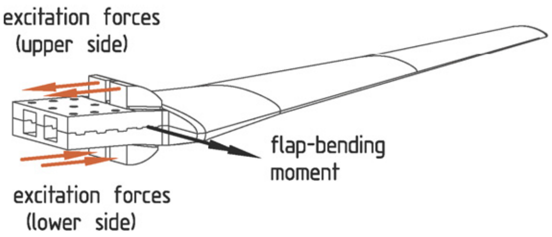

Figure 5.1: Visualisation of excitation forces on a model [32]

surfaces and it is highly responsive. It is however, a very large and expensive system.

This rotating clamp option requires a modification of the clamp to allow the model to rotate freely in the side of the wind tunnel. This requires heavy duty bearings, which in turn requires a too high torque.

5.1.5 Torsional Rod

A torsional rod is an option similar to the deforming bar. A rod is positioned inside the model and is clamped at a specific location to the inside of the model. The rod runs from this particular location to the outside of the wind tunnel. It is then given an initial rotational displacement which in turn twists the model to the same rotational displacement. It is the same principle as a torsional spring which is tensioned and released. The tensioning, by means of a rotation, can be done using an electric motor, similar to the one used in the rotating clamp option. After tensioning, the rod is instantaneously released from the motor, which leads to an oscillatory motion of the model.

An advantage of this method is its simplicity and low cost. The cost is composed of a motor and the manufacturing and integration of the rod. As mentioned earlier, the motors vary in price, where the less powerful and less accurate ones are most inexpensive. The accuracy of this method depends on the accuracy of the motor used to rotate the rod. This can be improved by investing in a more accurate motor. A disadvantage is that the rod changes the inertial properties of the model, which alters its natural frequencies. However, the extent of this influence is dependent on the size of the rod. Furthermore, a mechanism needs to be designed which can instantaneously release the tensioned rod, which adds to the complexity of this method.

5.1.6 Wing Integrated Excitation System

The last option to excite the model that is considered, is one of having a wing integrated excitation system. This mechanism is based on an existing mechanism used at the European Transonic Wind Tunnel [32]. The mechanism pushes at a chosen frequency on the upper and lower surface. This is done by switching between the top and bottom surface, as shown in Figure 5.1. In this way, shear is introduced in the structure which causes an excitation of the model.

This mechanism can be integrated within the mounting system and only works with a clamped mechanism. To push the upper or lower surface, a stack type piezoelectric actuator is used. This type of actuator is of cylindrical shape, and expands when a current is applied to it, and contracts when this current is reversed.

There are some advantages to using this technique. The first advantage is that it has already been used in the past for aeroelasticity experiments. Therefore, it is proven concept and has a higher probability to provide the expected response. Another advantage is that the frequency that is used to produce the vibration can be precisely known. This reduces the amount of uncertainty. Additionally, the excitation of the model can easily be modelled using FEM software.

A disadvantage of this method is the cost. It is a method, which requires changes to the wind tunnel. Concerning the FSI solver validation of this type of mechanism, it is required to precisely know the frequency at which the stack actuators vibrate the model. When this is known, it is possible

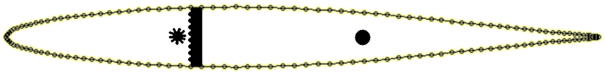

Figure 5.2: Representation of the gears

to distinguish which oscillations of the model are induced by the flow and which oscillations are induced by the excitation mechanism. This requires a high accuracy of the excitation mechanism. Typically, the accuracy of the displacement of piezoelectric stack actuators is in the order of $0.5nm$. This is deemed sufficiently accurate with respect to FSI solver validation purposes.

5.1.7 Gear Option

This option consists of two gears, of which one is located inside and connected to the model and the other is located on the side of the mount. The model is attached to the mount by means of a rod. A torsional spring is used to twist the gear through the mount at the front of the model, after which it is released. By moving the leading edge of the model up, this induces a pitching motion of the model about the rear attachment point of the rod with the model.

This method is considered to be relatively inexpensive, since only gears, a rod and a torsional spring are needed. The method is however complicated, since it requires a modification of the mount to contain the gear. Furthermore, high loads are induced on the rods, since the model is supported by just the moving rod at the front and the rod at the back of the model. Figure 5.2 shows a simplified representation of the gears and rod in a side view of the model.

5.1.8 Excitation of Flow Ahead of Model

Another option for the actuation of the model is to modify the flow field as opposed to actuating the model. This can be done by moving plates upstream in the flow in a rotary way. At a moment in time, the flow should be shaped as a sine wave. This sine wave is then be an input for the model deforms accordingly. The sine wave flow is created for a short duration and is then followed by a constant steady flow. In this way, the behaviour of the model is be observed.

This technique has one main advantage in that it was used extensively by NASA in the past decades. It is a proven concept that does makes the model oscillate.

However, some disadvantages are also present. The installation of such an actuation system is complicated in the TST-27. Another problem arises with the FSI solver validation. The entire actuation system and the flow disturbance resulting from it must be modelled within the CFD code to provide accurate data for the FSI validation.

5.2 Selection of Actuation System

From the previously mentioned actuation options, one has to be selected to be designed in detail. The selection criteria are those mentioned in Section 5.1.1. Several options can already be discarded. First of all, the deforming bar is a non-feasible option. The bar, which is either the piezo bender or a bar containing the magnetorheological fluid, is either too weak, meaning they have a low yield strength, or is not capable of delivering a large enough load to deform the model. Therefore, this option can be discarded. The method of exciting the flow ahead of the model is also discarded, since the modelling of this flow in FSI solvers adds unnecessary uncertainties, which affect the accuracy of the provided data. It is also complicated to determine the flow disturbances needed to deflect the model by a specified amount. For the gear option, all the loads acting on the model must be carried by the rod, since the model is free to rotate about the clamp. The loads acting on the rod are too high, resulting in failure. This option is therefore discarded.

The remaining options are the rotating clamp, the torsional rod, the actuated flap and the wing integrated excitation mechanism. The excitation mechanism has a different effect than the other two systems when exciting. It excites the model constantly whereas the other two mechanisms disturb the model during a short time interval. As a result of this, there is no pure interaction between structures and aerodynamics for this excitation mechanism. It is also not possible to model the piezo stacks in the aeroelastic code without any large modifications of the code, making the other two possibilities superior.

To investigate the feasibility of the rotating clamp, an estimation is made of the required motor size to rotate both the clamp and the model. The wind tunnel wall has a thickness of approximately $40mm$ and is made out of steel. Due to the large inertia of the mount, this requires a very strong and fast motor to obtain the required impulse input on the model. However, the torque needed to turn the mount is too large and a stepper motor with the required speed and accuracy is not available. Also, stepper motors on the market can only produce base angles starting with an angle of 0.36°. This means that the angle of attack of the model can only be altered in steps of 0.36°. A higher accuracy is required since the measurements are taken at intervals of 0.2° angle of attack. Therefore, gears are required to decrease the step angle of the stepper motor. Due to the limitation in accuracy and speed of the motor, this option is discarded.

The feasibility of the rotating rod was verified by means of a calculation of the required torque to rotate the model. As an initial estimation, a rotation of 5° of the model is considered. This leads to a required torque of $85Nm$. To position the rod inside the model, it cannot have a radius larger than $0.4mm$, which is contrained by the thickness of the model. The rod runs through the entire model as well as through the wind tunnel wall, and is attached to a mechanism which torques it. The rod has a length of around $30cm$ resulting in very high von Mises stresses, in the order of $3500MPa$. The angle of twist of the rod is 28°. This stress and angle of twist cause the rod to fail. This option is therefore not feasible.

The remaining option to actuate the model is the flap. Although this option has only a limited number of advantages, it is considered to be the most feasible option. The limitation, as mentioned earlier, is the fact it is difficult to precisely size the flap without a CFD analysis. It is however possible to produce an estimation of the lift forces as a result of a flap deflection. From this, the flap size can be approximated. Furthermore, in comparison to the other options which required a motor, the force to move the flap is expected to be relatively low and therefore a small, fast and sufficiently powerful motor can be selected to change the orientation of the flap.

Based on the feasibility of all the possible actuations mechanisms, the flap is considered to be the most feasible one and this is therefore the selected actuation method for the model.

5.3 Detailed Design

In this section the selected option is designed conceptually. The selected option is the flap. Several variations are possible with regard to flaps. For the model in this report, the simplest flap is selected. This is a plain flap, with a chord, c_f, as shown in Figure 5.3. This flap is selected, since there is insufficient space for complicated mechanisms inside the model to extend and retract it.

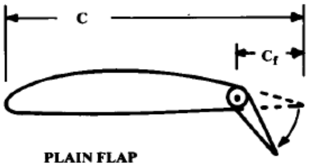

Figure 5.3: Plain flap [62]

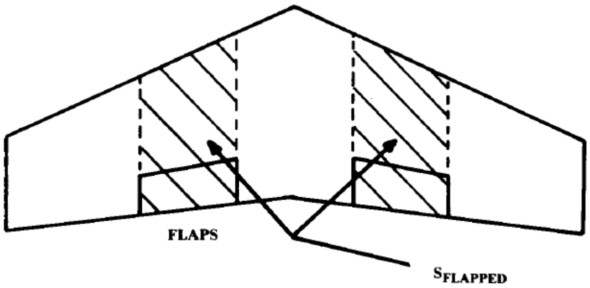

Figure 5.4: Flapped area [62]

5.3.1 Sizing of the Flap

The dimensions of the flap are determined by first performing an initial estimation based on a method to size flaps. From the dimensions following from this estimation, the flap is sized in more detail.

Initial Estimation The flap is sized using an initial sizing method explained in [62]. This method is for commercial aircraft, but is nevertheless deemd a sufficient method to establish initial dimensions of the flap for the model. Equation 5.1 gives the change in maximum lift coefficient, $\Delta C_{L_{max}}$, based on the flapped area, S_f, an approximate lift coefficient contribution of a high-lift device, $\Delta C_{l_{max}}$, the total wing area, S_{ref} and the sweep angle of the flap hinge line, Λ_{HL}. This approximation method considers the width of the flap to be 30% of the chord of the wing and it considers the flap deflection angle to be 40°, these numbers are typical for commercial airliners. The method does not take into account the span-wise position of the flap.

$$\Delta C_{L_{max}} = \Delta C_{l_{max}} \cdot \left(\frac{S_f}{S_{ref}}\right) \cdot cos(\Lambda_{HL})[62] \tag{5.1}$$

Based on statistics, the approximate lift coefficient contribution of a plain flap is 0.9 [62]. Furthermore, the sweep angle of the hinge line is set to be equal to zero. In this way the cross-section of the part of the model with the flap remains constant and the lift coefficient is therefore also constant. This allows to approximate the lift force acting on the flap. The flapped area, S_f, is the area of the wing between the extended edges of the flap, this is shown in Figure 5.4.

S_f is calculated by multiplying the length of the flap by the chord length. Since the chord of the model is constant along the span, the length of the flap can be expressed as a percentage of the length of the model. Applying these simplifications and inserting zero for Λ_{HL}, Equation 5.1 then reduces to Equation 5.2, in which L_f is the length of the flap.

$$\Delta C_{L_{max}} = \Delta C_{l_{max}} \cdot \left(\frac{L_f}{L}\right) \tag{5.2}$$

Based on this increase in lift coefficient, the increase in the lift force can be computed using Equation 5.3.

$$\Delta F_L = \frac{1}{2} \cdot \rho \cdot V^2 \cdot S \cdot \Delta C_{L_{max}} \tag{5.3}$$

Assuming this increase in lift force is acting at the tip of the model, the tip deflection, due to the increase in lift of the flap, can be computed using Equation 5.4.

$$\delta = \frac{\Delta F_L L^3}{3EI} \tag{5.4}$$

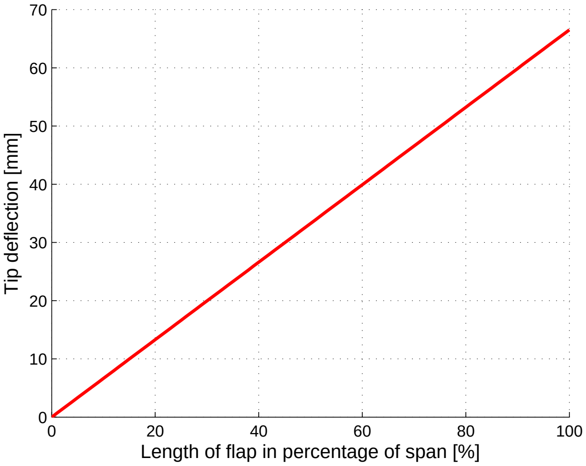

Figure 5.5: Tip deflection of the model due to a flap deflection of 40°

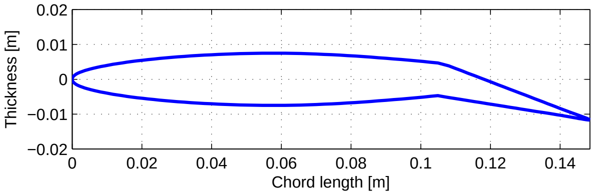

Figure 5.6: Representation of the model cross-section with flap

Equation 5.4 is used to analyze the tip deflection for varying flap length, this is presented in Figure 5.5. This figure gives an estimation of the tip deflection as a result of a deflected flap.

To have a measurable response, the tip deflection increase, due to the flap, needs to be approximately $10mm$. The required deflection cannot be determined precisely, since it depends on too many factors in the aeroelastic model as well as the measurement techniques. Therefore, based on a trial and error approach the $10mm$ tip deflection is set as the minimum.

From the estimation performed in Figure 5.5, it is found that a flap length of 15% of the model length is required to satisfy a tip deflection of $10mm$. This value is based on a flap deflection of 40°, as mentioned earlier [62]. These values are used to size the flap in more detail.

Detailed Sizing Ideally, the flap is located as close to the tip as possible. This minimizes the required area of the flap to induce a deflection. Due to any possible three-dimensional effects occurring at the tip of the model, such as vortices, it is decided to have space margin of $15mm$ between the model tip and the span-wise location where the flap is positioned. This space also allows for positioning of a hinge about which the flap rotates.

Using the Javafoil applet [22], the NACA 64A-010 airfoil can be modified to have a flap with a specified flap chord and deflection angle. From this applet, values for the lift coefficient for different angles of attack can be generated. An airfoil was created with the earlier found deflection angle of 40°. This deflection angle results in flow separation occurring at very small angles of attack. Therefore, the deflection angle was decreased to a smaller deflection angle, namely 15°. Figure 5.6 shows a representation of the deflected flap.

The flap length required for a $10mm$ tip deflection, based on the estimation, was found to be 15%

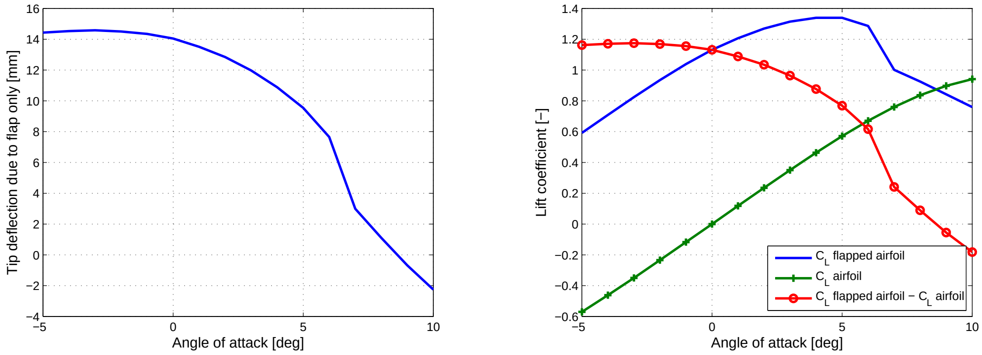

(a) Tip deflection due to flap

(b) $C_L - \alpha$ curve

Figure 5.7: Tip deflection and lift coefficient as function of angle of attack of the model

of the model length. This value is based on the force being centred at the tip. This however, results in an under estimation of the required flap length. Therefore, the flap length is increased to a value of 20% of the model length.

To calculate the tip deflection due to a flap more accurately, beam theory is used. Equation 5.5 gives the tip deflection for a point force located at a position s from the root.

$$\delta = \frac{\Delta F_L s^2}{6EI} \cdot (3L - s) \tag{5.5}$$

In this equation, the moment of inertia is assumed to be the estimated one of the model without any flap deflection. Having a flap increases the moment of inertia. However, to be able to perform analytical calculations, the moment of inertia is assumed to be constant along the length of the model. Furthermore, in the case of the model, it is assumed that the lift force attaches at the centre of the flap. The lift force of the flap is computed by subtracting the lift force of the airfoil without flap from the airfoil with flap.

Figure 5.7a shows the effect of a flap on the tip deflection for varying angles of attack. The shape of this plot follows a similar trend as the $C_L - \alpha$ curve shown in Figure 5.7b. These plots are based on the NACA 64A-010 airfoil with the flap deflected at an angle of 15°. During the experiment, the angle of attack is varied only between 1.2° and 3.6°. In this range of angles of attack, it can be read from Figure 5.7a that the minimum tip deflection is approximately $11mm$. This is $1mm$ above the minimum of $10mm$ and gives a small safety margin.

The flap with a length of 20% of the model length, a flap chord of 30% of the model chord and a deflection of 15° results in a satisfactory tip deflection to have a measurable response. The final dimensions of the flap resulting from these calculations are a length of $46mm$ and a width of $45mm$ as shown in Figure 5.8.

In addition to the tip deflection, an angle of twist occurs as result of the increase in lift force due to the flap. This angle of twist, together with the tip deflection, is used as input to the aeroelastic model. It has a beneficial effect on the response, since it increases the amplitude of the response. This in turn is advantageous from a measurement point of view. Equation 5.6 gives the angle of twist [23].

$$\phi_{twist} = \frac{\Delta T_q L}{GJ} \tag{5.6}$$

In this equation, T_q is the torque, defined as $\Delta F_L \cdot (\bar{x}_{flap} - \bar{x})$. $\bar{x}$ and $\bar{x}_{flap}$ are the location of centre of gravity and the location of the lift force on the flap, with respect to the leading edge of the model. L and G are the length and shear modulus of the model, respectively. J is the torsional constant of the cross-section of the model, which is not possible to determine analytically for an airfoil. For the

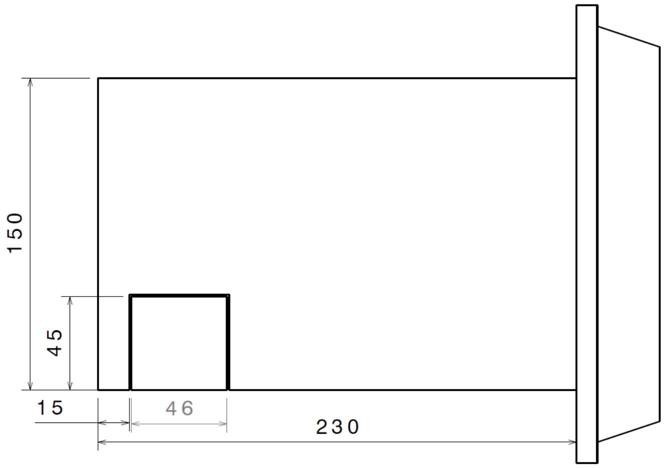

Figure 5.8: Top view of the model with the flap with dimensions in $[mm]$

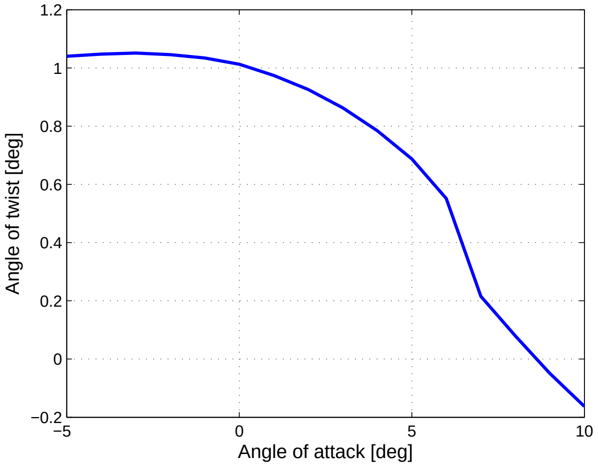

Figure 5.9: Angle of twist as a function of the angle of attack

determination of J, a hollow rectangular cross-section, with a width of $150mm$, height of $15mm$ and a thickness of $3mm$, is assumed. These dimensions follow from the maximum cross-sectional dimensions of the model. Furthermore, it is assumed that the lift force acts in the centre of the flap and that the moment arm between the centre of gravity and the lift force remains constant for different angles of attack. In Figure 5.9 it is shown how the angle of twist varies with the angle of attack. It can be observed that this plot follows the same trend as the plot for the lift force due to the flap, shown in Figure 5.7b. At higher angles of attack the angle of twist decreases, this is because the airfoil stalls here. As is discussed in Chapter 7, during the experiment, the angle of attack is varied only between $1.2°$ and $3.6°$, therefore the angle of twist, during the experiment, has a minimal value of $0.8°$. The assumptions made for the torsional constant results in an under-estimation of the angle of twist. For the model, the angle of twist is higher than the one computed in this section.

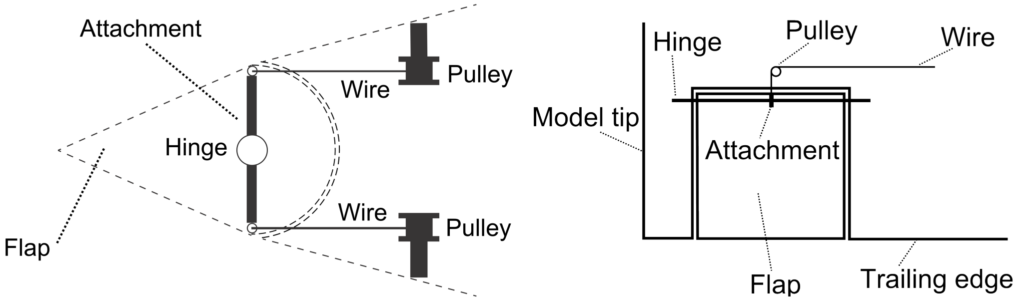

(a) Side view

(b) Top view

Figure 5.10: Representation of the flap mechanism

5.3.2 Flap Mechanism

The flap mechanism consists of a flap attached to a hinge. This hinge runs through the length of the flap and is attached to the model at two locations. Both the inside of the flap and the rear of the model are curved, as shown in Figure 5.10. In this manner the flap can 'turn' inside the rear of the model. If the front of the flap and the rear of the model are made with a flat surface, a part of the top of the model must be removed to allow the flap to rotate about the hinge. The resulting gap creates disturbances in the flow. Therefore, the edges of the model and the flap are rounded. At two locations inside the flap, a cable is attached; one at the top and one at the bottom. For this to be possible, two attachment points are required. From these points, a wire runs towards the model in which two small pulleys are located; one on the top and one on the bottom surface. The wire runs along these pulleys to the root of the model. From here it runs through the mount to the outside of the test-section, where it is connected to an electric servo motor. When the model deflects, the wire can hit the top and bottom surface of the model. This can be prevented by positioning more pulleys along the length of the model.

To deflect the flap, the servo motor pulls the bottom part of the cable and feeds its top part. Doing so, the flap rotates about the hinge and the resultant lift force on the model increases. The flap is retracted by reversing the direction of the motor. The flap deflection angle can be varied depending on the required tip deflection of the model.

Chapter 6 — Measurement Techniques

With an established final design of the model and mount, as well as a defined set of validation data required from the experiment, the measurement techniques that obtain the data can be identified. This chapter describes the measurement techniques that have been considered. For every type of measurement, a set-up is discussed. Finally, the integration of the measurement techniques is described.

6.1 Measurement Techniques Choices

Following from the required types of validation data shown in Section 1.4, the measurement techniques have been divided in three categories: techniques that measure airflow and output flow velocities and shock wave extension from the model surface; techniques that measure model deformation; techniques that measure surface pressures and also output instantaneous shock wave position and strength. A selection is made from the considered measurement techniques, based on the advantages and disadvantages of every technique.

6.1.1 Flow Measurements

This subsection encompasses all viable measurement techniques to obtain information related to the flow during the experiment. Particle Image Velocimetry (PIV) and Planar Doppler Velocimetry (PDV) are considered, as they can provide three-dimensional flow data. Particle Shadow Velocimetry (PSV) and Schlieren are also flow measurement techniques, but these are not considered, because they are not suited for a three-dimensional model.

Particle Image Velocimetry PIV is a visual technique that measures particle displacement to obtain flow field data [59]. Particles are released in the flow, which are illuminated by a laser. The laser light is scattered by the particles, which can be recorded by a camera. By taking two images of the flow in rapid succession, the difference in position of the particles can be determined. From this data, the flow field can be reconstructed.

There are several possible types of PIV, the difference lies within the number of cameras used. In Figure 6.1, an example set-up for PIV is given with one camera. With this type of PIV, two-component velocity vectors can be measured. However, the out of plane displacement cannot be recorded, so this technique is only valid for two-dimensional flows. Stereoscopic PIV is a PIV method that can measure all three velocity components, albeit in a plane [13]. The cameras are placed under an angle with respect to each other, so each camera has a slightly different view of the same flow. By combining the two views, a three-dimensional reconstruction of the flow in the plane can be obtained. To obtain flow field data over the whole model, the laser is shifted and new measurements are taken. However, if the model is oscillating, phase-locking must be used to make sure that the measurements are taken at the same position within an oscillation cycle. The determination of the deflection is discussed in Section 6.1.2. To match the flow measurements at different laser locations along the span, the phase of the oscillation is determined with the model deformation measurement technique chosen in Section 6.1.2, and the flow data is joined when the phases coincide.

If one or two additional cameras are used, the technique is called tomographic PIV. With tomographic PIV, it is possible to measure all three components of velocity in a three-dimensional volume [14]. However, the three-dimensional volume remains relatively small when compared to the model and test section size (approximately $12mm$ depth [33]), while the data size increases considerably. Therefore, laser shifting and phase-locking is still needed to obtain flow data over the whole model.

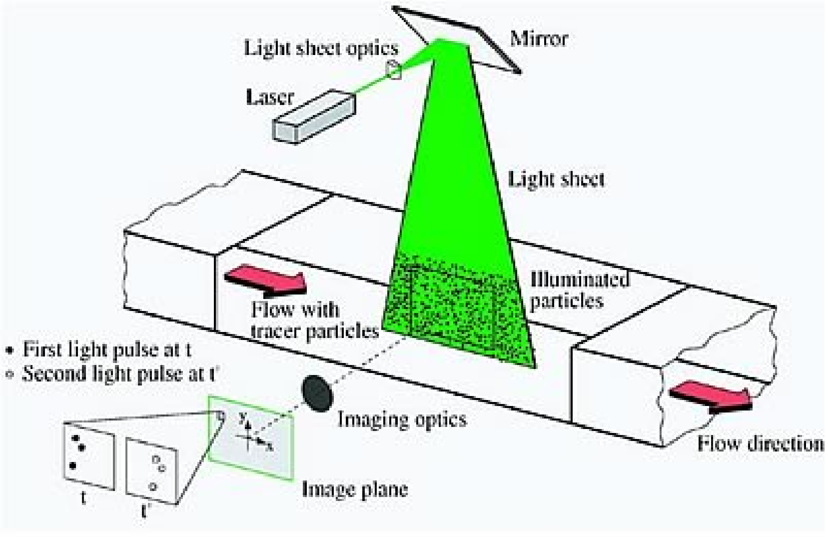

Figure 6.1: Example PIV set-up with one camera [50]

Planar Doppler Velocimetry PDV is another image-based technique that is capable of producing three component velocity measurements of the flow in a plane [27]. With PDV, one measures the Doppler shift of light scattered by seed particles. To perform PDV, particles are released in the flow and a two-dimensional plane of the flow is illuminated with a laser. Since the frequency shift is many orders of magnitude smaller than the frequency of the illuminating light, an absorption cell is placed in front of the camera. This absorption cell is a narrow band of iodine, and it allows the Doppler-shifted light to be detected by the camera [51]. It is unreasonable to assume that the particles are uniformly distributed. Furthermore, the laser power is not constant over time. If unaccounted for, these effects cause errors in the velocity calculations. To resolve this, another camera looks at the same light without filter as a reference [27]. An example set-up for PDV is shown in Figure 6.2.

Due to the way PDV works, it is desirable to collect scattering. This allows for large fields of view (10-50cm [52]), or for seeding particles to be smaller than 1μm [27]. It also has a good measurement uncertainty, which is lower than 1m/s RMS. The spatial resolution depends on the camera used. A

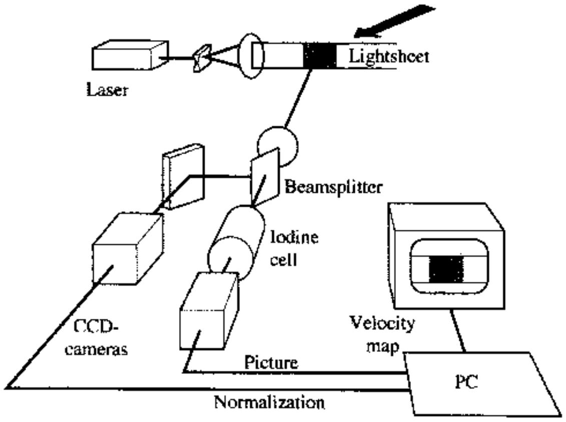

Figure 6.2: Example PDV set-up [52]

downside to PDV is the scanning frequency, which is relatively low (maximum of $400 Hz$ [52]). Also, the iodine cell can cause significant errors in the measurements if not correctly calibrated [27].

Flow Measurement Technique Selection The ability to provide the three components of the flow is essential for a three-dimensional model. PIV with one camera can therefore be eliminated, as it cannot detect the out-of-plane displacement of the particles. Tomographic PIV can provide data for a three-dimensional volume of the flow, whereas stereoscopic PIV and PDV can only provide the three components of the flow velocity within a plane. However, the added benefit of using tomographic PIV is negligible, as phase-locking and laser shifting are still needed to obtain data over the whole model, while the data size grows considerably. Therefore, tomographic PIV is eliminated, and only stereoscopic PIV and PDV remain as options. Stereoscopic PIV has cameras that can measure at a high framerate ($5,400 Hz$ at maximum resolution), whereas PDV has a maximum of $400 Hz$ [52]. Considering the high frequencies of the model oscillations, and the short response time, it is not possible to provide (near-) instantaneous flow measurements with PDV. Therefore, stereoscopic PIV is used for flow measurements.

6.1.2 Deformation

This subsection discusses all viable measurement techniques to measure displacement, and indirectly the frequency, of the model. Videogrammetric Model Deformation (VMD), Projection Moiré Interferometry (PMI), strain gauges and accelerometers are considered.

Videogrammetric Model Deformation VMD is a measurement technique that is able to visually determine displacements of the model [7]. Targets are mounted on the model, which are recorded by a camera. Based on the displacement of the targets between images, the deformation of the model can be determined. The cameras can be placed either above or on the side of the model, but a clear view of all targets is needed [8]. The targets can be either glued to or painted on the model. The targets are as thin as possible, to minimise their intrusiveness. In [7], retroreflective targets were used with a thickness of $1.02 mm$, and a surface roughness of $5.08 \mu m$. Another type of targets used were polished paint diffuse targets, which had a surface thickness of $0.0127 mm$ and a surface roughness of less than $0.254 \mu m$. The targets must be evenly spaced along the chord length at several locations along the span of the model to measure the displacement [3]. An example of target placement for VMD can be seen in Figure 6.3. The accuracy of VMD depends on the camera, namely the frequency at which it can measure and the resolution of the images. The minimum displacement that can be measured with a camera depends on the minimal shift of the targets on the recorded images.

One major advantage of VMD is the ability to measure the model visually, without the need to place sensors inside the model. This is especially important in the TST-27 wind tunnel, as there is little space available within the model. Although the measuring takes place outside the wind tunnel, the technique is still intrusive, since targets need to be placed on the model. Also, the TST-27 only allows cameras to be placed on the side. Although measurements from the side are still possible [8], it is less ideal than measuring from above, as the targets are viewed from under an angle, which needs to be accounted for. A technique for VMD measurements from the side is discussed in [8].

Projection Moiré Interferometry Projection Moiré Interferometry (PMI) is an optical measurement technique used for surface topology and shape characterization [54]. The elegance of the technique is its simplicity, as it requires only two major components: a projector and a camera. An example set-up for PMI can be seen in Figure 6.4. The projection system projects a grid of equispaced parallel lines on the model surface. The projector system requires its optical axis to be perpendicular to the measured surface [17]. The lines can be created by placing a Ronchi ruling in front of the projector. The projector emits infra-red light with a wavelength of about $800 nm$, which must be taken into account for the recording camera. Additionally, the camera must be placed under an angle with respect to the projector of about 30-45° [17], while still lying within a plane perpendicular to the projected

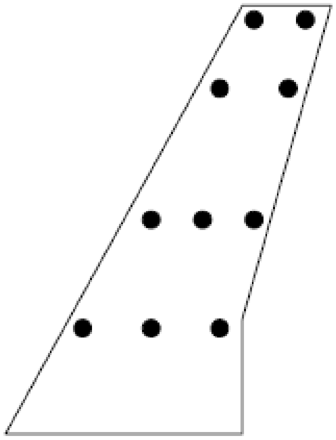

Figure 6.3: Example target placement for VMD (not the actual model) [3]

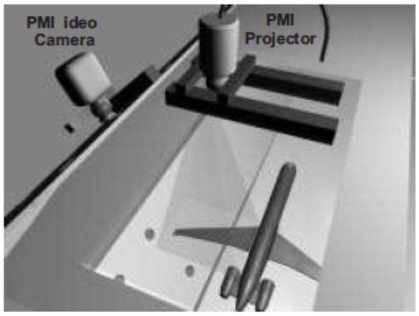

Figure 6.4: Example PMI set-up [17]

grid lines. An example PMI image from raw data can be seen in Figure 6.5. Image processing is then applied to remove camera distortions with a computationally generated reference grid (the vertical lines). Combining this reference grid with the raw image, the Moiré fringe patterns can be found, as seen in Figure 6.6.

PMI is the least intrusive measurement technique considered for deformation, as nothing needs to be attached to the model for it to operate. PMI can also be used for large areas, which enables it to measure the model globally. Furthermore, PMI provides a continuous surface grid of the model, which can increase its accuracy. The downside of PMI is the sampling rate, which is very low ($10Hz$ in [17]). Another argument against PMI is the fact that the projector needs to be located above the model. In the TST-27, no space is available to add a camera above the model.

Strain Gauges Strain gauges are sensors that locally measure the strain of an object. Deformations cause the electrical resistance of the strain gauge to change, which can be measured. From this change in resistance, the strain can be deducted. Since the strain gauges are dynamically loaded due to the oscillations of the model, hysteresis may occur, depending on the amplitude and the variation of the load, as well as on the length of the measurement grid. Shorter strain gauges and higher amplitudes increase the risk of hysteresis. Experience shows that hysteresis becomes smaller after a number of load cycles, and that with strain gauges of lengths between $3mm$ and $6mm$, errors do not exceed 1% [24]. The length of the strain gauge also has an impact on accuracy in case of high frequencies. For example, deviations from the static gauge factors reach 5% within the frequency range up to $45kHz$, $110kHz$ and more than $290kHz$ for $20mm$, $10mm$ and $3mm$ gauges respectively [75]. The use of strain

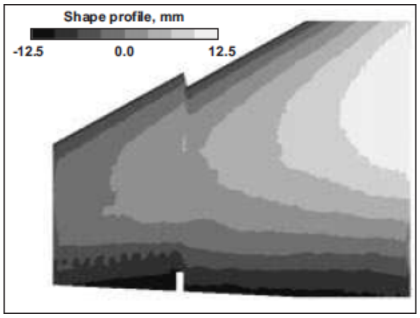

Figure 6.5: Raw PMI image [17]

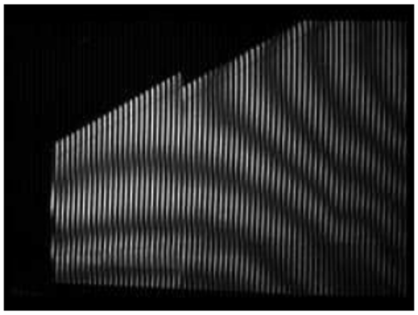

Figure 6.6: PMI image with Moiré fringes [17]

gauges is generally restricted to strains in the range of $\pm 3,000 \mu m/m$, with gauges used for dynamic measurements having ranges of between $\pm 2,000 \mu m/m$ and $\pm 2,400 \mu m/m$ and operating lives of 10^7 cycles [42]. For strain gauges with a metal measuring grid, fatigue occurs as a result of the continuous dynamic loading. Depending on the amplitude and variation in the load, this results in an increase in electrical resistance, which is apparent as dynamic zero point drift, and in microscopic cracks on the grain boundaries in the metal of the measuring grid. This in turn results in failure [24]. Moreover, strain gauges suffer from transverse sensitivity. This may result in erroneous measurements in case displacements in directions perpendicular to the measurement direction occur.

The cost of strain gauges varies largely, and can range from few euros to hundreds of euros. Moreover, the positioning of the strain gauge requires supplementary materials, which may exceed the cost of the strain gauge.

Strain gauges have the advantage that they can measure local deformation very accurately. However, they need to be placed within the model, where space is limited. Another downside of strain gauges, is the fact that it can only measure displacements locally, therefore multiple sensors are needed to obtain deformation data over the whole model. Also, the short operating life at high frequency oscillations must be considered.

Accelerometers Accelerometers are electromechanical devices that measure accelerations. The accelerations can be integrated over time twice to locally obtain displacements. Also, if placed at convenient locations, the accelerometers can identify separate oscillation modes. Moreover, to avoid measurements in directions other than the desired ones, the accelerometers are placed at the elastic axis. Piezoelectric accelerometers can be used for oscillation measurements since they have a wide frequency response, good sensitivity and resolution and are easy to install. In the case of low level signals, it is desirable to use an accelerometer of high sensitivity in order to provide an output signal well above the amplifier's noise level. Accelerometers to be considered for the purposes of this experiment most likely need to have a range of 0 to $50g$. Accelerometers of higher range also have higher natural frequencies but lower sensitivity and signal to noise ratio. Therefore, a careful trade-off needs to be made between range and sensitivity or resolution, when selecting a particular accelerometer. The cost of accelerometers is comparable to the cost of the strain gauges.

Just as with strain gauges, accelerometers only measure deformation locally, and multiple sensors are needed to provide data over the whole model. Accelerometers are actually less accurate for measuring displacement with respect to strain gauges, as accelerometers only obtain displacement indirectly by integration.

Deformation Measurement Technique Selection Since the use of PMI necessarily requires a camera with a top view of the model, and since this is not possible in the TST-27 wind tunnel, this measurement technique is automatically dismissed. Strain gauges, accelerometers, and VMD can be used independently or in combinations. Additionally, strain gauges and accelerometers have been mentioned as reliable methods for measuring bending. However, using either strain gauges or accelerometers introduces complexity in the manufacturing of the model, and measuring the pitching motion of the model with techniques other than VMD requires even more sensors. Moreover, only a slight deviation from the prescribed location of placement for these sensors may render the data irrelevant for validation purposes. Finally, VMD is required to allow the use of pressure sensitive paint, as mentioned in Section 6.4, and does not need equipment supplementary to the one used for pressure sensitive paint. Therefore VMD is used to measure displacement in this experiment.

6.1.3 Pressure

This subsection describes the considered measurement techniques which can measure pressure on the surface of the model. Pressure Sensitive Paint (PSP) and pressure transducers are considered here.

Pressure Sensitive Paint The fundamental principle of PSP is the coating of the model surface with oxygen-sensitive luminescent molecules dispersed in an oxygen-permeable polymer binder and illuminated with exciting radiation. The intensity of the resulting luminescence depends on the pressure seen by the coating molecules. The luminescence intensity distribution that accompanies the pressure field over the model surface can be recorded using an imaging camera. Then the image can be digitized, stored, and processed on a computer to produce a map of the model surface pressure field [39].

The relation between pressure and light intensity can be derived from the second order approximation of the Stern-Volmer relation seen in Equation 6.1, where the zero subscript denotes the value for no-flow conditions. The second order form of this relation is used to account for non-linearities in the sensitivity coefficients. The coefficients A, B and C are the coating sensitivities of the paint that can be determined by experimental calibration.

$$\frac{I_{f,ref}}{I_f} = A(T) + B(T)\frac{p_{ref}}{p} + C(T)\frac{p_{ref}}{p}^2 \tag{6.1}$$

According to the Stern-Volmer equation, the PSP has the highest luminescence when there is the least amount of oxygen concentration, that is, the least applied pressure. Aside from the sensitivity coefficients, an important parameter of PSP is the response time to changes in pressure. Due to the very high frequency at which the model oscillates during the experiment, a fast-response PSP is required. Considering the frequency of the first bending mode of the model, the PSP must respond to pressure changes in less than $3ms$. Such types of PSPs have been developed, and show pressure resolutions under $400Pa$ [43].

Pressure Transducers Pressure transducers are sensors that directly transform surface pressure inputs to electrical signals. The Kulite XCQ-062-25D is the smallest pressure transducer found on the market, with a diameter of $1.6mm$ and a length of $9.5mm$. It is also the only pressure transducer that can physically be implemented in the model, due to space availability and flow interference reasons. Pressure transducers measure pressure locally, and a large array of sensors is needed to have a nearly complete surface coverage. Moreover, this sensor can only be placed at 40% chord, and in the close vicinity of this chord percentage, where the model is the thickest. This particular sensor has a range of $0 - 1.7MPa$ and a natural frequency of $240kHz$. The cost ranges from €200 to €300.

Pressure Measurement Technique Selection An advantage of pressure transducers is the high possible measurement frequency. However, a PSP measurement system can achieve frequencies that are well above the required frequency. Unlike the conventional discrete pressure transducer method, PSP can acquire a global surface pressure distribution. It can produce global, high-spatial resolution and quantitative pressure distribution results [47]. Moreover, since the size of the model is limited, limited amounts of measurement equipment can be placed inside the model. Therefore, extremely low spatial resolution may be achieved with pressure transducers. Moreover, the thickness of the model away from the 40% line does not allow pressure transducer placement in any case. Additionally, from the high spatial resolution provided by PSP, shock wave location and shock wave displacement can be found for FSI solver validation. An important argument against both PSP and pressure transducers is that they interfere with the flow around the model. However, if the paint is applied with high precision and uniformity, the uncertainty caused by this interference can be eliminated, by knowing the new properties of the model. Finally, the costs involved in using PSP as the main surface pressure measurement system are estimated to be significantly lower than of using pressure transducers. For example, an initial investment of around €19000 for the light source and software needed for PSP can be compared to a price of approximately €300 for a pressure transducer. Assuming the model thickness allows for such placement, it costs €19000 to measure the pressure at seven discrete chord locations along nine span locations.

Considering the facts mentioned above, for this experiment, PSP is used to measure the pressure distribution on the model. Three pressure transducers are used to calibrate PSP.

6.2 Particle Image Velocimetry Set-up

Stereoscopic PIV will be used to measure the flow field around the model. This means that two PIV cameras are used simultaneously. As mentioned before, the cameras are placed under an angle with respect to each other, so each camera has a slightly different view of the same flow. This is required to measure the three components of the velocity. However, to have the entire image plane in focus, a lens must be added between the camera and the plane. The plane created by the lens, the camera and the image plane must have have one common line for the image to be in focus. This condition is called the Scheimpflug condition [41]. Furthermore, light filters are needed to counteract background light, and only record the light scattered by the particles. Since the laser light is green, green filters will be used.

The FASTCAM SA1.1 [55] is the camera with the highest frame rate that the TU Delft has available for PIV purposes. A high frame rate is desired, due to the high frequencies of the vibration modes of the model. It has a frame rate of $5{,}400Hz$ at a resolution of $1024\text{x}1024pix$. It can only measure the flow field at half that rate, which is $2{,}700Hz$, since the camera requires two images to obtain one flow field image. In general, the sampling frequency should be ten times higher than the to be observed frequency. Although the PIV camera does not measure the vibrations of the model, it does measure the flow, which in turn is affected by the deflection of the model. To accurately match the flow field data with the deflection, the measurements must occur at the same time, and thus have the same frequency.

As was seen in Section 3.5, the first bending mode and the first torsion mode can be measured with the frame rate of $5{,}400Hz$ at the maximum resolution of $1024\text{x}1024px$. The second bending mode can only be detected if the frame rate is increased. One may also consider increasing the frame rate, if more data points per cycle are required. However, this may interfere with the PSP measurements. PSP needs a certain exposure time to capture the incoming light from the coating accurately.

When selecting PIV seeding particles, the effect the particles may have on the other measurement techniques must be considered. The model will be coated with PSP, and the particles may interfere or damage the coating. For example, oil can spoil the coating, whereas titanium-oxide particles can damage it. Dry ice does neither of these, while still providing reliable PIV measurements [31]. One problem this study ran into was obtaining a reliable particle size. This was addressed in [36], where a static mixer was used to create more uniform particle sizes, as well as dispersing the particles in the flow more uniformly.

6.3 Videogrammetric Model Deformation Set-up

VMD will be used to measure the deformation. As no room is available directly above the model, the VMD camera will be placed to the side of the model. The technique described by Burner et al. [8] will therefore be used, as they implemented a VMD system for in-flight VMD measurements with the camera also on the side. It is mentioned that an angle of about 10° was used between the camera and the model. However, it is desirable to have the largest angle between the model and the camera as possible. As VMD visually measures the difference of the position of the targets, the targets must be as visible as possible. Decreasing the angle between the model and the camera decreases the light return from the VMD targets, thus making the targets harder to track. One way around this is by raising the targets, but this severely affects the flow around the model. Therefore, only the angle between the model and the camera will be considered, and it should preferably be around 30°, as is conventional with obliquely measuring VMD [8].

Polished diffuse paint targets will be used as VMD targets for the experiment. These targets are the thinnest, and have a much lower surface roughness than retroreflective targets. The targets have a surface roughness of $0.254 \mu m$, which is slightly higher than the requirement of $0.2 \mu m$, but it is deemed a minor difference. The targets should be placed in a similar fashion as in Figure 6.3. Targets should be placed near the leading and trailing edge of the model at different points of the span. From this, the rotation of the model can be measured, and indirectly the eigenfrequency for torsion. Targets will also be placed at the mid-chord of the model. Combined with the targets at the trailing and leading edge, the plunge motion and indirectly the eigenfrequency for bending can be measured. The target locations along the span of the model can be chosen depending on the bending and torsion modes that are to be measured. However, since only the first bending mode and the first torsion mode are considered, no specific locations are needed to measure these modes. It has been decided that four rows of of three targets will be used along the span of the model. The targets will be placed at 20%, 40%, 60% and 80% of the span. The target size is discussed by Bell et al. [3], where it is mentioned that VMD targets should be as large as 8 pixels across on the camera. To achieve this for all targets, the targets further away from the camera should be made larger.

6.4 Pressure Sensitive Paint Set-up

In [2], Baron et al. first showed that sub-millisecond response times can be achieved by using porous binders for the paint. According to Gregory et al. in [21], there are three types of PSP that have such response: anodized aluminium, thin-layer chromatography (TLC) plate and polymer/ceramic (PC) PSP. However, since anodized aluminium PSP can only be used on aluminium models, and since TLC PSP is too fragile to use in wind tunnel testing, the only PSP applicable to this experiment is PC-PSP. This type of paint can be applied by spraying on a complex shape, such as a wing model [65].

PC-PSP is a hybrid formulation that was developed specifically to improve the diffusivity of the binder material, thus allowing faster response times. The formulation is a mixture of a high concentration of ceramic particles with a small amount of polymer to physically hold the ceramic particles to the surface. The response times of the polymer/ceramic paint formulations developed by Scroggin in [68] were on the order of $60 \mu s$, which is sufficient for the purposes of this experiment (requirement D1.1.2) .

Along with the binder, the luminescent dye is an the essential ingredient of PSP. According to Liu in [72], three families of luminescent dyes, Platinum Porphyrins, Ruthenium Polypyridyls and Pyrene derivatives, have been commonly used for making PSP. The Platinum Porphyrin compounds, which can be excited by either Ultra Violet (UV) or blue light, emit red luminescence. They are very sensitive to oxygen, but they often have low luminescent intensity at the atmospheric pressure. The Ruthenium compounds also emit red luminescence when excited by either an UV light or a blue light. They are very photo-stable, but are difficult to incorporate into polymer systems. The Pyrene derivatives, which are UV excited, emit blue luminescence. The Pyrene derivatives have low temperature sensitivity; however, they suffer from photo-degradation and sublimation. Considering the above mentioned characteristics, platinum tetra(pentauorophenyl) porphyrin (PtTFPP) is used in the PSP for this experiment, as specified by Disotell in [11]

Placement and Usage One of the main components of a PSP measurement system in unsteady conditions is a high-speed camera. For this experiment, the FASTCAM SA1.1 is used. This is the same camera as the camera used for the PIV measurements.

The illumination source of a PSP measurement system is used to excite the luminescent sensor molecules of the PSP coating, causing them to luminesce. The intensity of the light emitted by the coating is proportional to the excitation light that is absorbed, and the high frame rate used by the camera limits the exposure time. It is therefore necessary that the excitation light field illuminating the model surface is of sufficient power level in the PSP coating absorption wavelength band, namely, $390nm$, and that measurements are conducted at the lowest acceptable frequency. It is also desirable that the intensity of the excitation source be stable in time [39]. The LM2X-390 LED Illumination Source has to be purchased for this experiment from Innovative Scientific Solutions Inc. (ISSI). Moreover, to allow for sufficient exposure of the images, the camera frequency is set at $2700Hz$.

It is important that the detector records only the luminescence emission in the spectra of the PSP coating. The detection of light from sources other than the PSP coating produces an error in the measurement. To prevent this, the use of optical filters over the detector source is required [39]. A long pass filter with a wave length of $590nm$ is placed in front of the camera. This filters the illumination light component, but allows the luminophore component.

As the model has a three-dimensional shape and displaces during the test, a correction for image spatial non-alignment is done by spatially aligning, "registering," the wind-on (I) and wind-off (I_0) images before they are ratioed. In this operation the wind-on image is aligned (i.e., shifted, rotated, scaled, warped, etc.) with the wind-off image through a mathematical transformation so that a location on the model is the same in both the wind-on and -off images [39].

To calibrate the measurements that result from PSP, two Kulite XCQ-062-25D are placed at 20.8% (A) and 55.75% (B) chord and 83% span and one at 52.5% (C) chord and 8.5% span as seen in Figure 6.7. This figure also displays the predicted pressure distribution at one of the highest levels of displacement in the oscillation cycle, as is discussed in Section 8.1.1. The locations for the sensors have been chosen strategically. According to [72], the transducers used in in-situ calibration have to cover as much of the pressure range as possible, hence the transducers placed at 83%, where most of the pressures can be observed without significant interference from the tip vortices. Moreover, transducer B is at some moments in the oscillations up stream of the shock wave, which helps eliminate the errors caused by temperature sensitivity. Finally, the pressure transducer placed closer to the root (A) serves as a reference. At that location there are no significant variations in pressure. The pressure transducer configuration is limited by the two dashed lines in Figure 6.7, which mark the chord range where the thickness of the model allows for transducer placement.

To use the pressure transducers, holes are drilled on the surface of the model. Since the transducers are used together with PSP, they must be placed in the model after the paint is applied, so that the paint does not interfere with the sensor. The diameter of the sensor is $1.6mm$ and the length is $9.5mm$. A least squares fit of the data establishes the calibration coefficients mentioned earlier [4]. Accurate identification and spatial correlation of the transducer and paint data requires that the in-situ method be performed after the mapping operation, using the spatially correct intensity ratio image. In the in-situ method, the data that result from the pressure transducers is correlated to the luminescence intensity at different points on the model through extrapolation. A diagram of the calibration process is

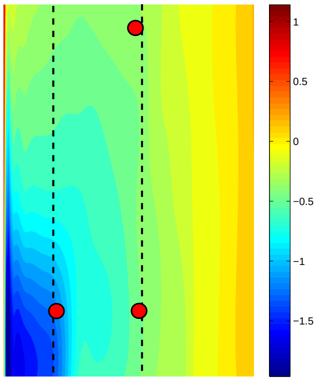

Figure 6.7: Pressure transducer locations

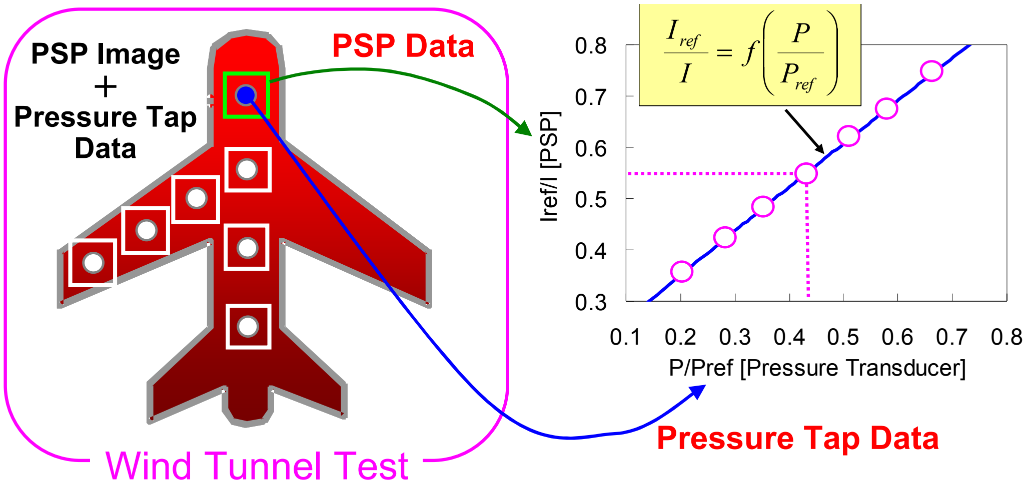

Figure 6.8: Diagram of the in-situ calibration process [47]

shown in Figure 6.8. Software acquired from ISSI, namely the ProImage, ProField, ProGraph package is used for the calibration and pressure mapping.

Moreover, with in-situ calibration, temperature effects are absorbed in the calibration coefficients, and spatial variations in temperature are averaged out among all points included in the calibration [4].

Finally, in order to capture only relevant measurements, to simplify the data processing, as well as to decrease the power usage by the light sources, the measurement series requires a definite start and end. To start every measurement series, a change in the state of the actuator is used as a trigger. To end every measurement series, the actuator state may be changed again, or another manual trigger can be implemented.

6.5 Measurement Techniques Integration

It is desirable that both the time resolved pressure and velocity distributions are measured simultaneously using a combined system with the fast-response PSP and the time resolved PIV. The correlation of both the pressure and velocity fields are useful to analyze the unsteady flow fields and

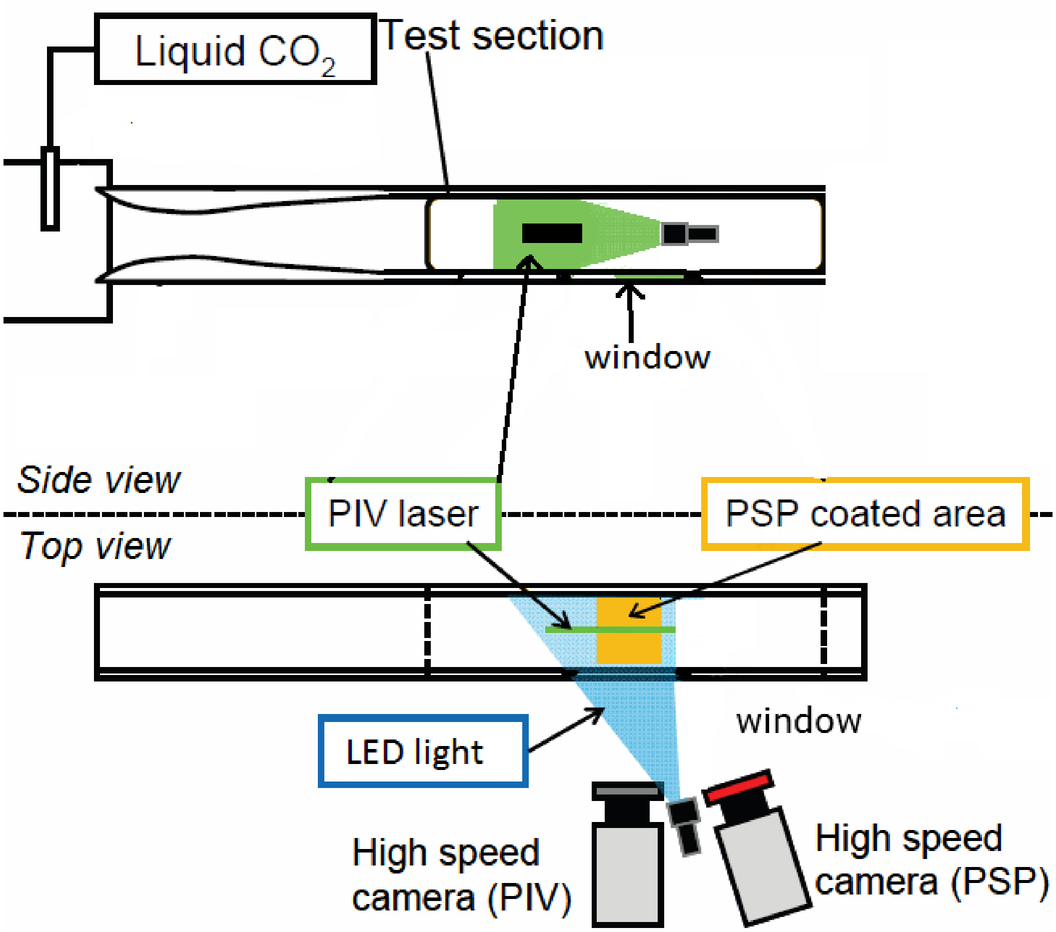

Figure 6.9: Illustration of the combined PIV and PSP measurement set-up [31]

validate FSI results.

According to Koike et al. in [31], the contamination of the tracer particles in PIV for PSP coating is one of the biggest problems encountered when using both techniques simultaneously. The titanium oxide particles that are commonly used for PIV at the TU Delft can damage the PSP sensor physically and chemically. In order to solve this problem, Reeder et al. in [63] proposed using solid carbon dioxide, namely dry ice, as the PIV tracer, since the dry ice particles sublime in normal atmospheric conditions and physical and chemical damages for the PSP coating are negligible. In order to exclude the illumination for PSP and the luminescence from the PSP, a band-pass filter for the wavelength of $532nm$, or green, is attached on the lens for the PIV camera. An illustration of the overall set-up can be seen in Figure 6.9.

Koike et al. concluded in [31] that the influence of the dry ice on the response ability of the PSP is small. The fog of the dry ice particles slightly interrupts the luminescence from the PSP to the camera and decrease the intensity of the measured intensity of the PSP luminescence, thus introducing noise in the PSP measurements. As the result, the averaged pressure measured with the PSP increased. However, the noise introduced by the PIV particles was smaller than pressure fluctuations caused by a moving shock wave, and were therefore deemed tolerable. A total decrease in pressure sensitivity of less than $0.01\%/kPa$ was detected.

Finally, the injection of the carbon dioxide may decrease the total temperature and the specific heat ratio in the wind tunnel. As a result, the velocity of the uniform flow decreases. Therefore, the monitoring and the controlling of the flow conditions are the most important issues for the simultaneous measurement of PIV and PSP using dry ice particles. Reeder et al. and Koike et al. report a decrease in flow velocity of 2 to 5% in [63] and [31] respectively. Moreover, Reeder et al. report that the flow remains uniform if dry ice is injected in the flow, and an empty test section is used.

To further facilitate the validation of FSI solver pressure data, the PSP data have to be mapped onto a surface grid of a model in the three dimensional object space. Liu and Sullivan in [72] describe an approach to conducting the PSP and VMD measurements simultaneously, with the same camera. In this approach, VMD software is integrated as an additional part of the PSP software package. Liu and Sullivan also mention that an oblique viewing angle of the camera, which is inevitable in the set-up of this experiment, is favourable for good position sensitivity for VMD measurements. Thus, the surface grid generated by VMD is used to map the pressures, and no additional transformations are required, since the two measurements use the same camera.

Chapter 7 — Experiment Set-up

As a final design is established for the model, the mount, the actuation system and measurement techniques, the experiment process can be described. This chapter describes the measurement campaign, detailing with both how the total number of measurements performed, as well as a description of the procedure of the experiment.

The way the measurement campaign is performed is crucial. It has an impact on the data provided for the FSI solvers, as well as on the amount of time the TU Delft TST-27 wind tunnel facility is used. This section details every aspect of the measurement campaign from the number of measurement points to the sequence of a wind tunnel run.

The wind tunnel testing is performed on a range of angles of attack from 1.2° to 3.6°. The interval taken between each measurement step is 0.2° which leads to a total of twelve measurements. These angles of attack are chosen to provide the necessary amount of data. Before an explanation can be made on why this range was chosen, it should be noted that for a given Mach number of 0.7, a supersonic region only appears at an angle of attack of 1.8° and higher.

Starting at an angle of attack of 1.2° means that for the first two measurements, no transonic behaviour is observed. The data obtained from these first two measurements are used to validate the set-up of the model, the calibration of the measurement techniques and the post-processing steps to make sure the experiment is set-up properly.

From the angles of attack of 1.8° to 3.6°, nine measurements are performed. These numerous measurements are performed to observe the different states of the shock waves over the model. The shock waves get stronger as the angle of attack increases. To validate FSI solvers, it is considered that to have an appropriate array of data, these different shock waves strength results are required.

The number of measurements possible depends on the amount of time available and the bolting mechanism. As a conservative estimation, it is considered that only one angle of attack measurement can be performed each half day. Having intervals of 0.2° and therefore twelve measurement points overall leads to a use of the wind tunnel of six days. The second parameters on which the interval was chosen depends on the bolting mechanism. The bolting mechanism needs to be very precise to allow for intervals of only 0.2°. For a lower interval, the accuracy is considered to be too low.

The procedure for the measurement campaign is as follows, see Figure 7.1. Note that it is considered that the model is already manufactured and the PSP coating has already been applied. Before anything can be mounted within the wind tunnel, the cameras for the PIV, VMD and PSP are set up on the window side of the wind tunnel. The model is then mounted and bolted within the wind tunnel at the proper angle of attack.

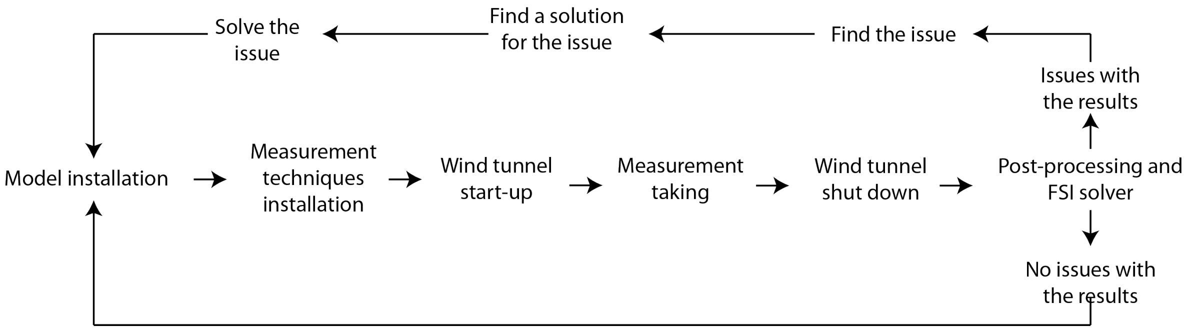

Figure 7.1: Testing procedure

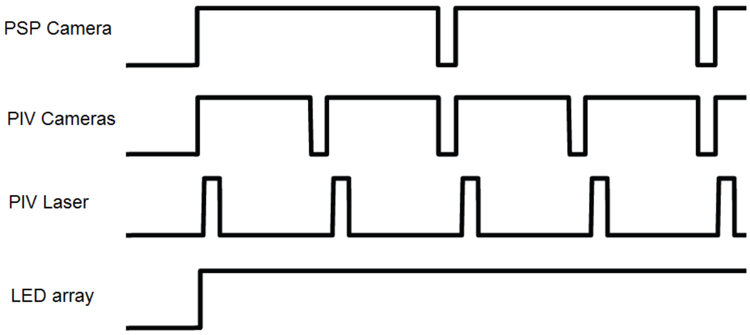

Figure 7.2: Measurement synchronisation procedure

The experiment starts with the wind tunnel producing the prescribed flow and with the particle dispenser introducing CO_2 particles into it. Once the flow reaches the required steady conditions, the actuator is used to induce the motion of the model. The change of the state of the actuator signals the start of the measurements to the measurement synchronisation device. Since the PSP camera is set at a frame rate that is twice as small as the PIV camera frame rate, the two types of cameras start the measurement at the same time but the PSP camera takes one image while the PIV cameras take two. Laser pulses are triggered with every PIV image taken, and the LED array is powered for the entire duration of the experiment. This arrangement can be seen in Figure 7.2.

After the model is excited, the CO_2 particles that cross above it change their velocity according to the flow disturbances. This is recorded by the PIV cameras. Simultaneously, the excitations cause changes in surface pressure. These in turn induce a response from the pressure transducers, and changes in luminescence of the PSP. The change in luminescence is recorded by the VMD/PSP camera. Additionally, the VMD/PSP camera records the displacement of the targets placed on the model.

The images stored in the PIV cameras are then transmitted to the PIV software, which analyzes the flow field information and computes the flow field velocities. The pressures sensed by the pressure transducers are transmitted to the PSP software through the pressure scanning system available at the TST-27. The VMD/PSP camera transmits the images to both the VMD and the PSP software. The VMD software analyzes the model deformation and generates and transmits a surface grid for every instant. The PSP software then calibrates the luminescence to the pressure on the model surface, and assigns pressures to every point on the two-dimensional model. Then the software maps these pressures to the surface grid. The surface pressures from the PSP software, the model deformation from the VMD software and the flow field velocities from the PIV software are then used to validate the outputs of the FSI solver. It is important to mention that the PSP can indirectly provide the pressure information on the bottom surface of the model. As an example, if the pressure distribution is measured on the top surface for an angle of attack of 4°, the pressure distribution on the bottom surface of the model can also be obtained if the same experiment, under the same conditions, is performed at $-4°$ angle of attack. This is possible due to the inherent symmetry of the airfoil.

The entire experiment process takes around thirty seconds. The wind tunnel is then stopped. The data obtained is then directly post processed and used to start validating the FSI solvers. This step is necessary to make sure there are no problems in the data collection process. If any issues arise with the results once they are inserted into the FSI solver, the problem should be isolated, a solution for it should be found and the measurement set-up should be changed accordingly. Then, the measurement step needs to be done again and the new results can once again be inserted into the FSI solvers. Once the results have been approved, the angle of attack is changed and the entire process starts again. This is done for the twelve measurement steps.

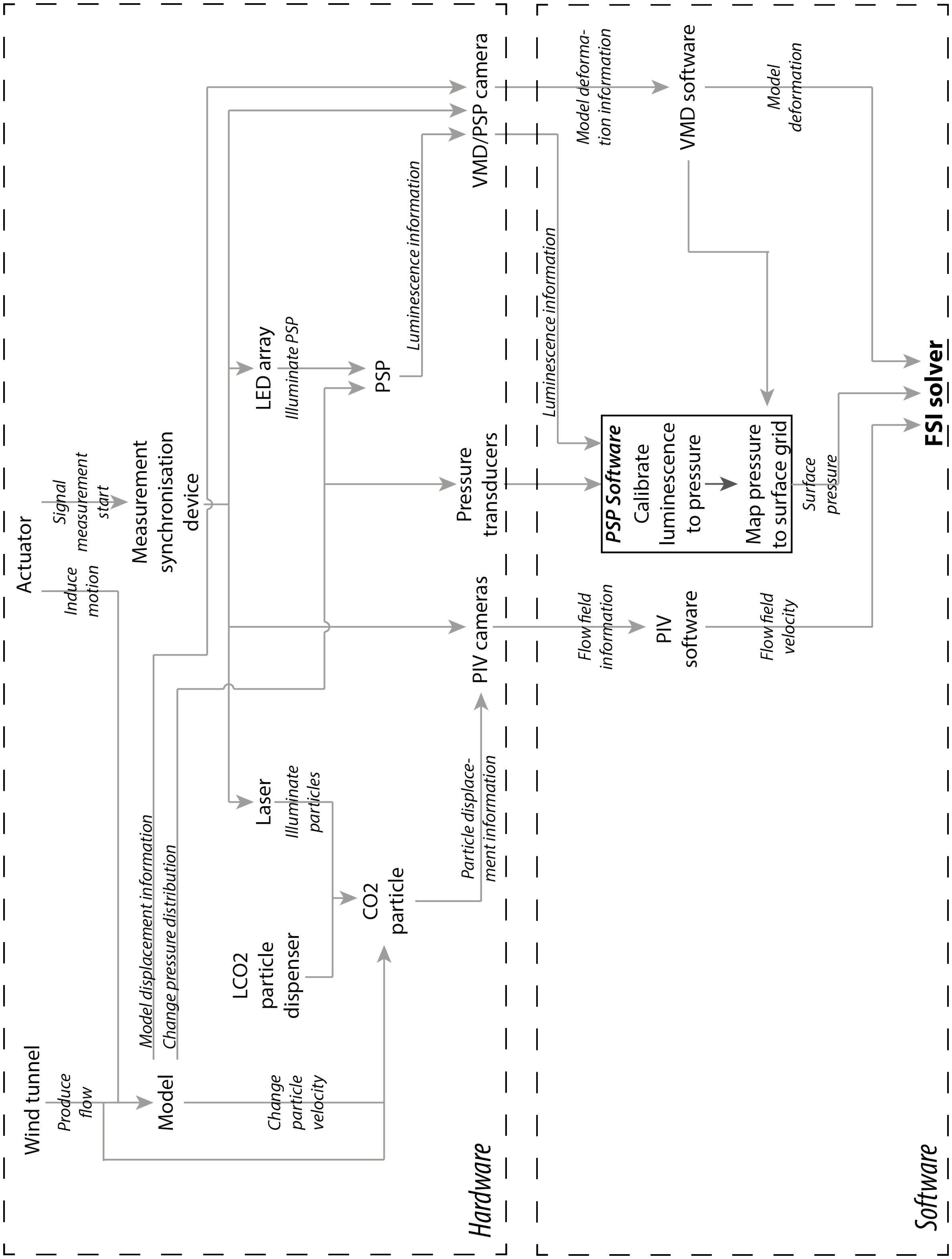

Figure 7.3: Hardware - Software diagram

Chapter 8 — Performance and Sensitivity Analysis

Once all the elements that take part in the experiment have been designed, a performance and sensitivity analysis can be outlined. The performance analysis presents the expected behaviour of the entire system, with the chosen design parameters. The sensitivity analysis on the other hand refers to the change in the behaviour of the system, should a parameter be slightly altered. This chapter covers the performance and sensitivity analysis of the model and the measurement techniques separately. In the model section, the aerodynamic and the aeroelastic performance, together with the aeroelastic-structural sensitivity are presented. In the measurement techniques section, the performance and sensitivity analysis of the PIV, PSP and VMD systems is presented. Finally, the compliance of the experiment with the requirements is verified.

8.1 Model

In this section, the analysis is focused on the performance and sensitivity of the model. First, the aerodynamic performance of the model in terms of pressure distributions on the top surface of the model is presented. Following, the time history of the structural response of the model, together with the damping characteristics and the flutter boundary are analyzed. Finally, the influence on modifying structural parameters of the model on the aeroelastic behaviour is outlined.

8.1.1 Aerodynamic Performance

In this subsection of the performance analysis, the time analysis of the pressure distribution that is measured by the PSP is analyzed. This analysis focuses on the top surface of the model, on which the PSP is applied. The pressure coefficient over an airfoil varies with the angle of attack, for a given Mach number. Thus, knowledge on the effective angle of attack faced by each two-dimensional section of the model along its length is necessary. Once the effective angle of attack is known, data regarding the pressure distribution along the chord of the NACA 64A-010 airfoil is needed. An assumption that is made in this analysis is that the tip vortices do not influence the pressure distribution over the model and are thus not implemented. However, this is taken into account when choosing the positioning of the pressure transducers required to calibrate the luminosity received by the PSP, presented in Section 6.4.

Consulting the NACA report on the 64A-series airfoils [70], values for the pressure coefficient on the top surface of the NACA 64A-010 airfoil are obtained. However, the data ranges from $-1.8°$ until $10.2°$, in steps of $1°$. There is no data available for the top surface of the airfoil for angles of attack lower than -1.8°. However, these data are equivalent to reading the values for the bottom surface of the airfoil at positive angles of attack, due to the symmetry of the airfoil. The angle of attack of the model changes rapidly in time in very small steps. Also, large pressure differences can be present along the chord line of the airfoil for a set angle of attack. That is why refined data is needed in order to accurately predict the time variation in pressure along the surface of the model where the PSP is applied. In order to solve this issue of discrete sparse data, cubic spline interpolation is used to obtain estimates for a wider range of values for the angle of attack and for the position along the chord length.

Reference Section of the Three-dimensional Model Since the numerical aeroelastic model only deals with the time response of a two-dimensional airfoil, as presented in Section 3.4.1, a solution needs to be found to represent the three-dimensional model. In other words, the results obtained from

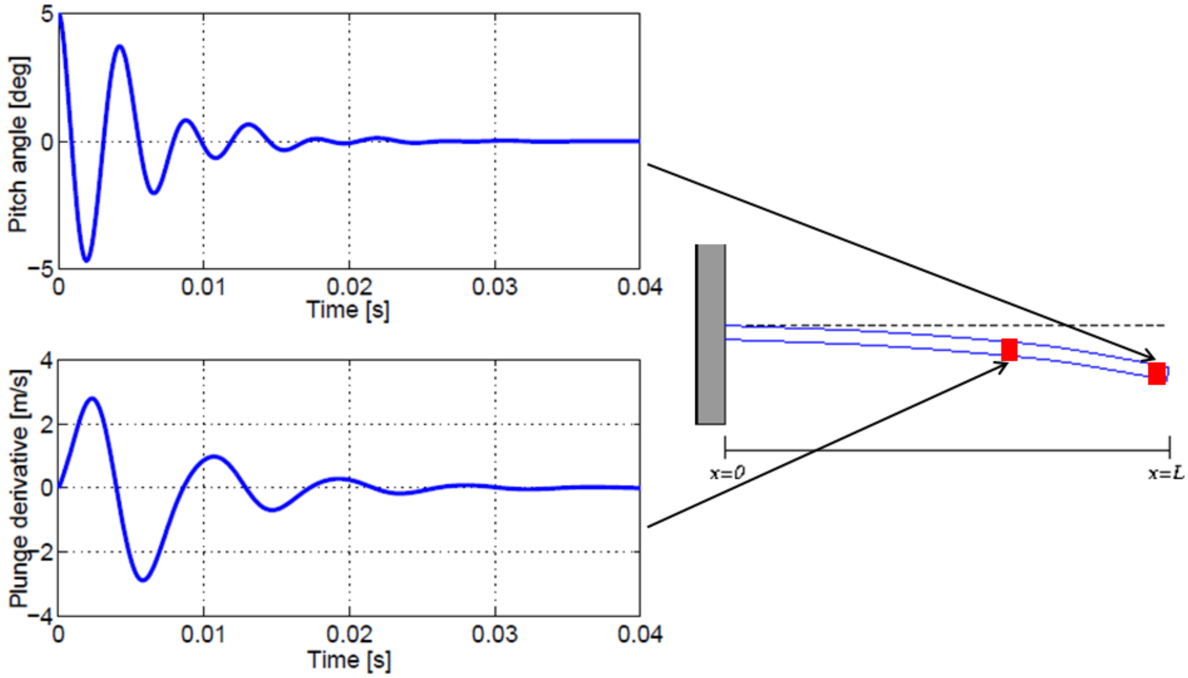

Figure 8.1: Pitch and plunge response of the two-dimensional aeroelastic model and their reference section location on the three-dimensional model

the numerical model represent a two-dimensional section on the model, from which information on the other sections on the model can be obtained. For the plunging motion, the displacement is not linear from the root towards the tip. Thus, it has been shown that a representative location along the beam that can be modeled by the two-dimensional model is at two-thirds of the length of the model. The pitch angle however varies linearly from the root towards the tip of the model. This is the reason why the tip can be a representative location for the entire three-dimensional model, in terms of the twist angle. Figure 8.1 shows the sections of the three-dimensional model represented by the two-dimensional results.

Effective Angle of Attack Different sections of the model along the length face a different angle of attack, due to the pitch angle that faces the flow and the plunging velocity. As mentioned before, Equation 8.1 describes the relation between the effective angle of attack and the two parameters mentioned before.

$$\alpha_{eff} = \theta + \frac{\dot{h}}{V} \tag{8.1}$$

where θ is the local pitch angle of the section, $\dot{h}$ is the local velocity in plunge of the section. The time history of these values are one of the outputs of the two-dimensional aeroelastic model. Equation 8.2 and Equation 8.3 show the procedure to obtain the three-dimensional plunging velocity and pitch angle, at each time step.

$$h(x,t) = A_{amp}(t)\phi(x) \tag{8.2a}$$

$$\dot{h_{3D}}(x,t) = \dot{A}_{amp}(t)\phi(x) \tag{8.2b}$$

$$\dot{A}_{amp}(t) = \frac{\dot{h_{3D}}(\frac{2}{3}L,t)}{\dot{\phi}(\frac{2}{3}L)} = \frac{\dot{h}_{2D}(t)}{\dot{\phi}(\frac{2}{3}L)} \tag{8.2c}$$

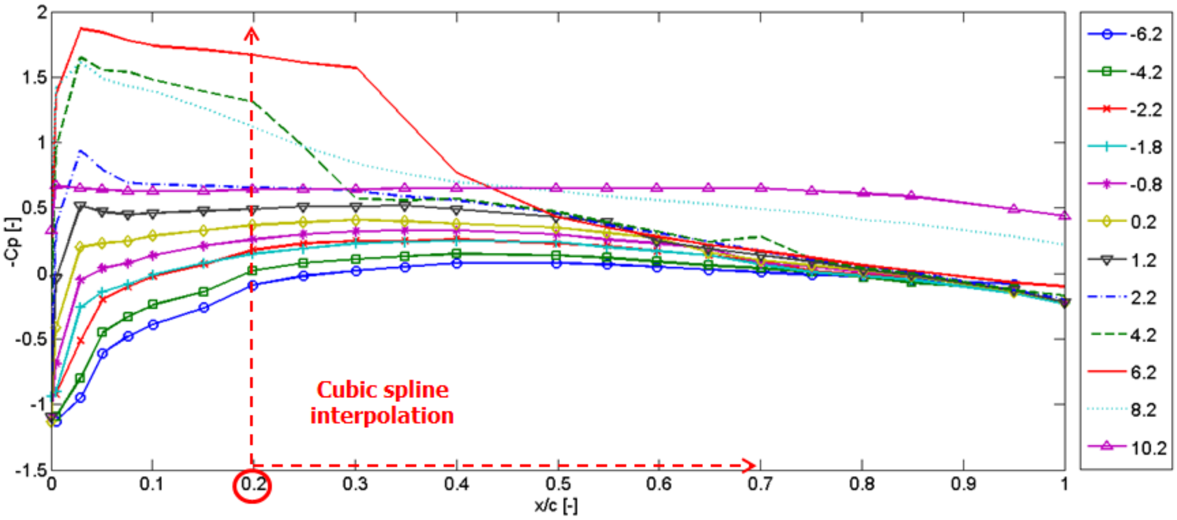

Figure 8.2: Pressure coefficient distribution for different angles of attack [°]

$$\dot{\theta}_{3D}(x,t) = \frac{x}{L}\dot{\theta}_{2D}(t) \tag{8.3}$$

In Equation 8.2, $h(x,t)$ represents the deflection function of the bending mode, $A_{amp}(t)$ being the amplitude at each time step and $\phi(x)$ the bending mode shape. $h_{3D}(x,t)$ indicates the plunge deflection function of the three-dimensional model, whereas $h_{2D}(t)$ represents the plunge motion obtained as an output from the two-dimensional aeroelastic model. Similarly, $\theta_{2D}(t)$ in Equation 8.3 represents the time history of the pitch angle - also an output obtained from the aeroelastic model, while $\theta_{3D}(x,t)$ is the pitch angle of the three-dimensional model. This set of equations is evaluated at every time step in order to obtain the complete time history of the effective angle of attack for each section of the three-dimensional model. This is later used to obtain the pressure distribution along the entire length of the model. It is important to mention that all the derivatives present in Equation 8.2 and Equation 8.3 indicate time derivatives.

Pressure Coefficient NACA 64A-010 Data on the pressure coefficients on the upper surface of the model can be obtained from the NACA 6-series report [70]. As mentioned before, data is obtained along the chord line only for a few angles of attack, from $-1.8°$ until $10.2°$. In order to achieve a better resolution in estimating the pressure distribution over the airfoil, cubic spline interpolation is used for both data points along the chord length and for intermediate angles of attack. In addition, the data for negative angles of attack is obtained by reading the pressure distribution on the bottom surface of the airfoil due to symmetry. Figure 8.2 shows the pressure distribution along the chord length for different angles of attack.

Pressure Coefficient Results Having obtained the effective angle of attack for each segment of the model and the corresponding pressure distribution along the chord length, a complete estimation of the pressure coefficient on the entire upper surface of the model can be obtained. For the purpose of this performance analysis, the pressure distribution along the top surface of the model is analyzed in time for two-thirds of an oscillation, in order to show the regions of high and low pressure, depending on the effective angle of attack. The response follows an initial pitch angle of 5° and no initial plunge deflection. Figure 8.3 shows instantaneous pressure distributions along the model, for different time steps. The time history of the effective angle of attack of the reference section that is placed at two-thirds of the length of the model is also shown.

As it can be seen, at positive angles of attack, the region towards the tip of the model experiences

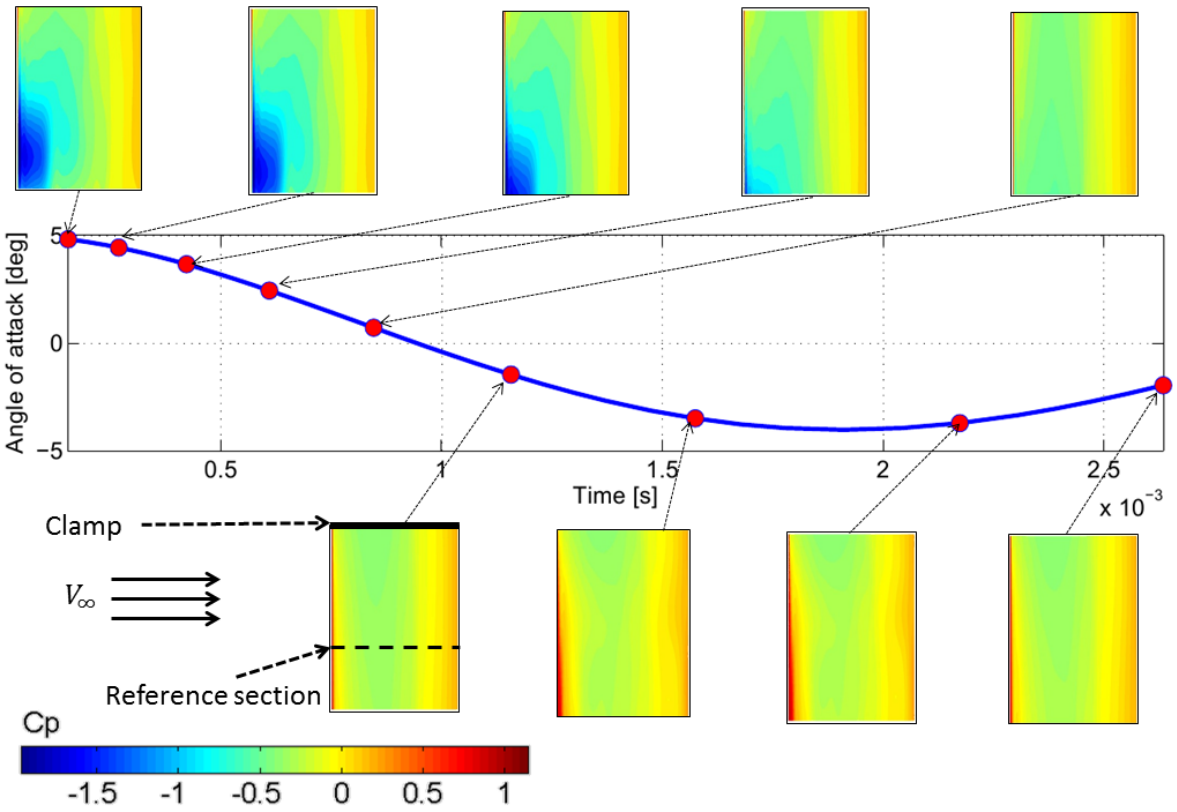

Figure 8.3: Instantaneous pressure distribution along the model

lower pressures, compared to the regions towards its root. This is due to the fact that the tip of the model has a higher plunging velocity, which adds to the value of the effective angle of attack. The low pressure coefficient indicates that the lift force is higher across the respective region. In addition, the large change in pressure across the chord line indicates an increase in drag. This is also an indication on the presence of a shock wave, since the change in pressure occurs abruptly, compared to other regions on the surface of the model, where the pressure gradient is more uniformly distributed. This is best depicted in the first three images of the instantaneous pressure response in Figure 8.3. As the angle of attack starts to decrease, regions of higher pressure coefficient move gradually towards the tip of the model, the lift decreasing accordingly. At the lowest angle of attack, there are no regions of very low pressure coefficient on the top surface of the model. One can observe that, in the area close to the tip of the model, high pressure coefficients exist close to the leading edge of the model. In addition, at low angles of attack, the pressure coefficient distribution is more uniformly distributed along the chord line, no abrupt changes being present. The reason for this is the fact that at positive angles of attack the shock wave is stronger on the upper surface.

In Section 3.1, the critical pressure coefficient has been plotted for different values of the free stream Mach number. Using the data obtained, it is found that for a Mach number of 0.7, the critical pressure coefficient has a value of −0.7791. That means that a pressure coefficient more negative than the critical pressure coefficient indicates a region of supersonic flow over the wing. In addition, when the pressure coefficient increases and reaches the critical value, a shock wave appears, making the flow subsonic. In order to visualize the exact location of the shock wave along the model, an isoline of the critical pressure coefficient can be drawn on the pressure distribution for each time step. The shock wave is located at the interface between the supersonic, low pressure region and the subsonic, high

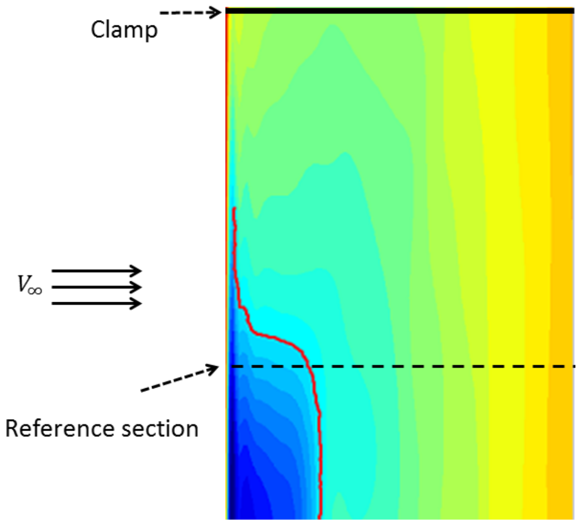

Figure 8.4: Position of the shock wave at 4° angle of attack of the reference section

pressure region. Figure 8.4 shows the position of the shock wave at a time step for which the angle of attack is positive. The red isoline presented in the figure shows the points on the model where the critical pressure coefficient is reached. As stated before, the PSP can measure changes in pressure as low as $57Pa$. Due to the fast changes of pressure in time along the chord and the span of the model, the pressure differences for the most part of the model are higher than this minimum pressure resolution, namely in the order of $1000Pa$. This means that the PSP is able to sense these changes over the entire upper surface of the model. Additionally, it has been demonstrated that because of the change with time of the effective angle of attack, the shock waves effectively move over the span of the model. Through the ability to determine the exact location and strength of the pressure distribution measured by PSP, the validation data necessary to define the aerodynamic loads on the model is provided.

8.1.2 Aeroelastic Performance

In this section the performance of the final design configuration with respect to its aeroelastic behaviour is explained. The Mach number at which the model is tested in the wind tunnel is 0.7, as explained in Section 3.1. The final structural design parameters are found in Section 3.5 and in Section 3.4.2, it is explained how the structural response, the flutter boundary and the damping ratio are obtained. In the three paragraphs below the aeroelastic behaviour of respectively the structural response, the flutter boundary and the damping ratio are given and explained for the final design configuration.

Structural Response The Aeroelastic behaviour of the structural response depends on the initial conditions. The initial conditions can be an initial plunge displacement (h), an initial pitch angle (θ), an initial plunge velocity ($\dot{h}$) and an initial pitch rate ($\dot{\theta}$), or a combination thereof. To give an example of the response of the system, an initial pitch angle of 3.6° is given to the model. When the initial conditions are let go, the response of the model is monitored and plotted. To summarize, the initial conditions are given in Equation 8.4.

$$\bar{x}_0 = [0 \; 3.6\frac{\pi}{180} \; 0 \; 0]^T \tag{8.4}$$

In Figure 3.4.2 it is explained how the structural response is obtained. In Figure 8.5 the plunge motion and pitch angle responses to these initial conditions are given, along with their derivatives.

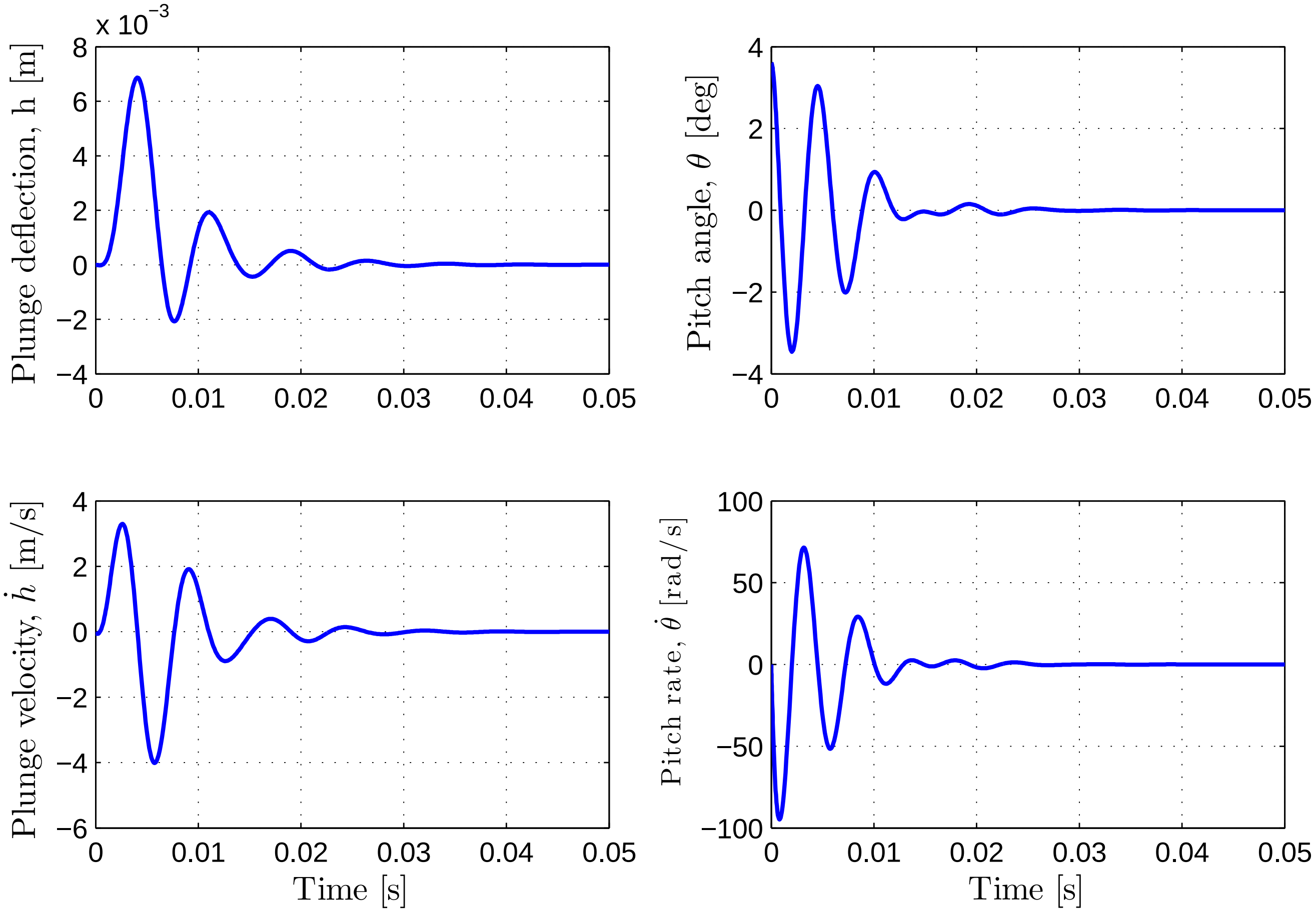

Figure 8.5: Response of h, θ, $\dot{h}$, $\dot{\theta}$ for $\bar{x}_0 = [0\ 3.6\frac{\pi}{180}\ 0\ 0]^T$

The plunge motion at the start is zero, since this is the initial condition. Because the pitch angle is positive at the initial conditions, the wing provides lift, causing the wing to have a positive plunge motion. At the same time the pitch angle decreases since the effective pitch angle due to the plunge motion decreases. As a result, the lift decreases, but at the same time the plunge motion increases because there is still a net force directed upward. This continues until the pitch angle equals zero. At this time, the plunge velocity has a maximum. Now the lift is negative and a net downward force directed downwards is created, causing a deceleration in the plunge motion and a decrease in the plunge velocity. If the plunge motion reaches its maximum, the plunge velocity is zero and the pitch angle has a minimum. At this time, the pitch angle rate is zero. After this point, the pitch angle rate becomes positive because the effective pitch angle due to the plunge motion increases. However, since the pitch angle is still negative the plunge motion decreases. Now the pitch angle rate increases. If the pitch angle rate reaches its maximum, the pitch angle is zero. At this point, the plunge velocity reaches its minimum. After this point, the pitch angle becomes positive and the wing generates positive lift again. As a result, the plunge velocity increases. The plunge motion is now decelerating, but because the plunge velocity is still negative, the plunge motion decreases. This continues until the plunge reaches its minimum and the pitch angle reaches its maximum. This process repeats itself until it damps out.

Since the system is highly damped, the behaviour described above is not perfectly seen. The maximum plunge velocity is not present exactly at zero pitch angle for the same time. Moreover, the

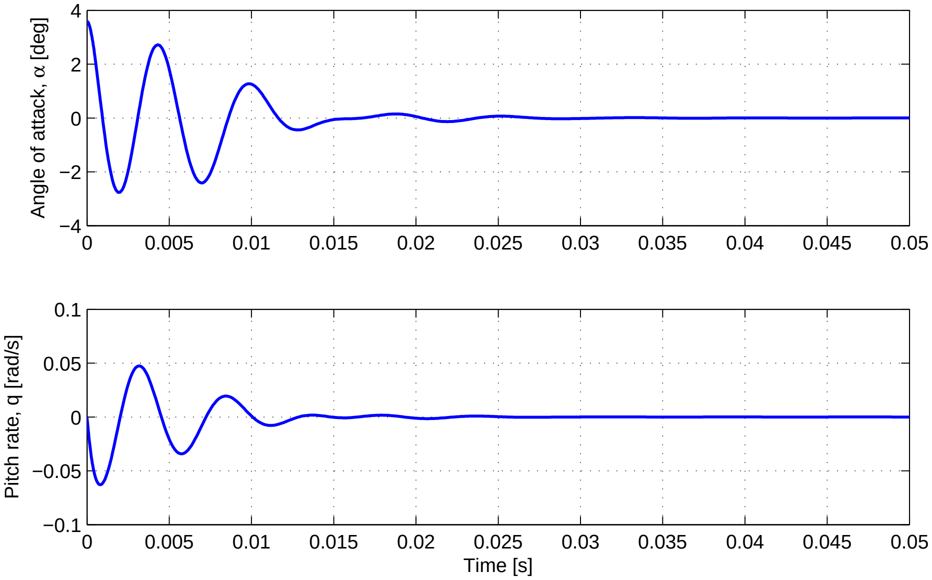

Figure 8.6: Response of α and q for $\bar{z}_0 = [0\ 3.6\frac{\pi}{180}\ 0\ 0]^T$

maximum pitch rate is not found exactly at a plunge motion of zero for the same time.

In Equation 3.21, the method to obtain the angle of attack and the pitch rate from the pitch angle, pitch rate, plunge motion, chord and velocity is given. In Figure 8.6, the response of the angle of attack and the pitch rate to the initial conditions is given.

To calculate the settling time until the oscillation of the model is damped out, it is assumed that the model is damped after three oscillations. This is chosen because in this time range, the amplitude is big enough to measure. The time untill the response is damped out after an initial pitch angle of 3.6° is 0.01478 seconds. This corresponds to an $|\alpha(t) - \alpha_{final}|$ that is 2.27% of its peak value. The frequency of the response is 204 Hz. This is within the frequency range of the FASTCAM to measure with full resolution.

Aerodynamics-Structure Temporal Behaviour In this paragraph, the analysis of the time response of the aerodynamic loads and the structural deformation in terms of plunging and pitching motion is presented. Similar to the pressure coefficients results, this analysis follows from an initial pitch angle of 5° and no initial plunge displacement.

Figure 8.7 and Figure 8.8 represent the aerodynamic loads, the normal force and the pitching moment coefficient (upper part of each figure), compared to the structural response in the plunge and pitch motion (lower part of each figure). The normal force coefficient in Figure 8.7 shows that the initial pitch angle creates an initial lift force, whereas no initial plunge deformation of the structure is present. Advancing in time, the structure starts to plunge, with a time delay, as a reaction to the initial lift. However, at the maximum amplitude of the plunging motion, the lift force becomes negative, damping the motion of the structure. It can be noticed, in general, that due to the higher frequency of the aerodynamic normal force, the structure is overexcited. This overexcitation results in the damping of the structure, which then reacts with a time delay and a phase shift to the aerodynamic inputs. The same behaviour can be seen in Figure 8.8. The initial pitch angle creates a pitching moment. However, the pitch response of the structure is not in phase with the aerodynamic moment coefficient. In this case, the frequency difference between the aerodynamic load and the structural response is less significant than the one seen for the normal force - plunge displacement.

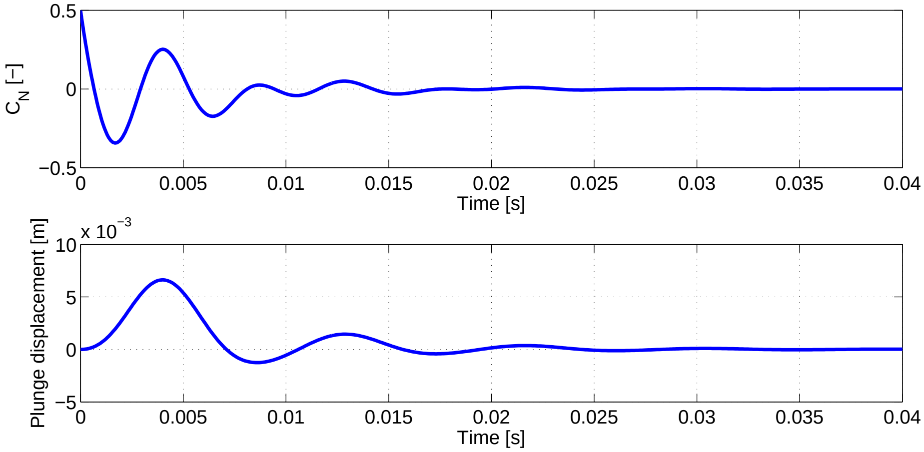

Figure 8.7: Normal force coefficient and plunge displacement in time

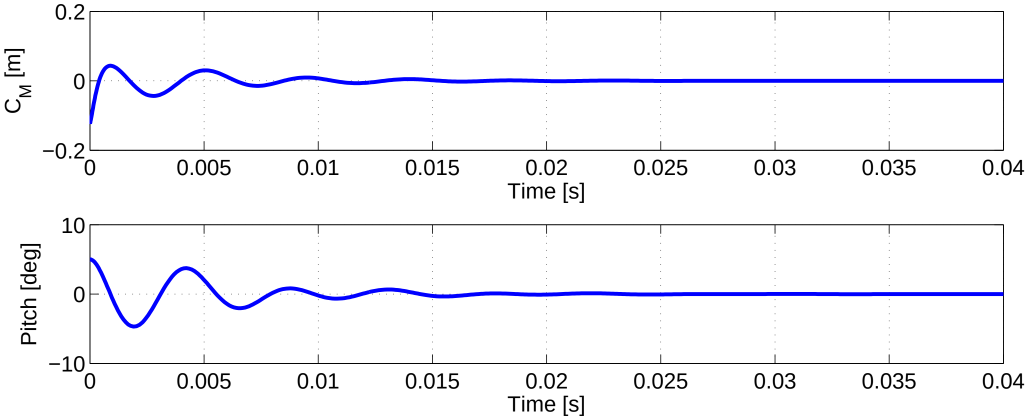

Figure 8.8: Pitching moment coefficient and pitch displacement in time

The aerodynamic loads affect the structural behaviour which, in turn, affects the aerodynamic loads. As a general remark, it can be noticed that the aerodynamic loads have similar frequencies and show a phase shift with respect to the response of the structure. Furthermore, the plunge response shows a higher damping when compared to the pitch response.

Flutter Boundary In Section 3.4.2, it is explained how the flutter boundary is obtained. The flutter boundary of the final model is given in Figure 8.9.

In Figure 8.9a, the flutter boundary for the transonic flight regime of $M = 0.7$ until $M = 0.89$ is given. Here, it can be clearly seen that there is a dip in the non-dimensional flutter velocity for the transonic flight regime. This is called the transonic dip. As explained in Equation 3.4.2, it is nescessary for stability that the flutter boundary stays above the wind tunnel range. In Figure 8.9b, it can be seen that the Mach number at which the model becomes unstable is 0.766. Since the model is tested at $M = 0.7$, the flutter margin is 9.4%.

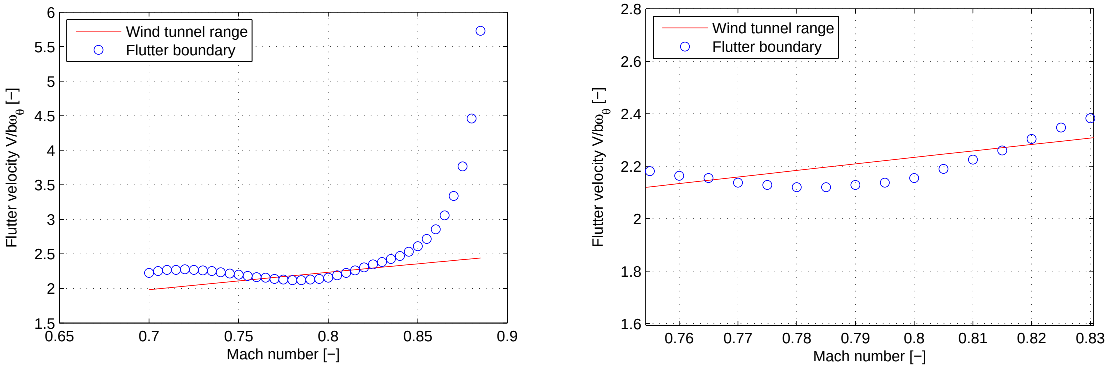

(a) Overview

(b) Close-up

Figure 8.9: Flutter boundary

Damping Ratio The damping ratio as a function of the non-dimensional flutter velocity for a Mach number of 0.7 is given in Figure 8.10. The eigenvalues that have been found consist of six real eigenvalues and three complex pairs of eigenvalues. To have a stable system, the six real eigenvalues have a damping ratio of one and the three complex pairs have a damping ratio between zero and one, see Section 3.4.2. The three complex pairs consist of:

- Coupled torsion- unsteady aerodynamics mode
- Torsion mode
- Bending mode

Since the eigenvalues for each mode change position across the range of velocities, they are given the same symbol. The three complex pairs are indicated by arrows, as seen in Figure 8.10.

The coupled torsion with the unsteady aerodynamics mode is very highly damped with a low frequency (low imaginary part of eigenvalue). This can be clearly seen from Figure 8.10. For a velocity of zero m/s, this mode has almost no frequency and the damping ratio is one. With an increase in velocity, the frequency of this mode also increases, as a result the damping ratio decreases. As can be seen from the figure, the spacing between each of the circles is equal. This means that this mode is changing continuously and has no regime where it is highly sensitive to a change in velocity.

The second complex pair that can be observed is the torsion mode. At zero velocity, this mode has only a frequency and no real part. As a result, the damping ratio is zero. With increasing velocity, the real part of the eigenvalue of the torsional mode increases and finally this real part becomes dominant, reaching a damping ratio of one. Since the damping ratio increases with an increase in velocity, this mode becomes stable throughout the flight regime. For a non-dimensional velocity of two, the circles have a larger spacing. This means that at this velocity, the torsion mode is highly sensitive for a change in velocity. After this point the torsion mode becomes more stable in a short time until about a non-dimensional velocity of three. After this point, the torsion mode is continuously increasing until a damping ratio of one.

The third complex pair is the bending mode. This mode starts, similar to the torsion mode, with only a frequency part at a damping ratio of zero. Next, the mode becomes more stable with increasing velocity until a non-dimensional velocity of two, like the torsion mode. At this point, the spacing of the circles become larger. This means that the bending mode is highly sensitive to the velocity. After this value, the damping ratio of the bending mode decreases rapidly and reaches values below zero. The non-dimensional velocity at which the damping ratio is zero, is 2.15. This is the point at which the system becomes unstable and is called the non-dimensional flutter velocity. This matches the point that be observed from the flutter boundary given in Figure 8.9. It can be seen that for a

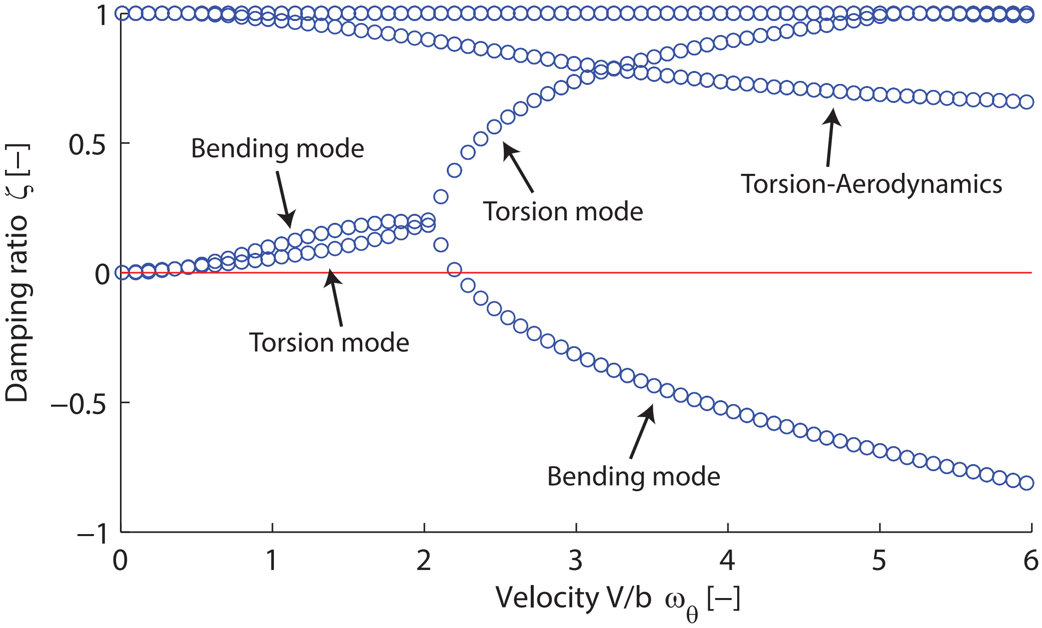

Figure 8.10: Damping ratio as a function of flutter velocity for $M = 0.7$

non-dimensional flutter velocity of 2.15 the flutter boundary goes below the wind tunnel range, making the system unstable.

8.1.3 Structure-Aeroelasticity Sensitvity Analysis

To determine and describe the sensitivity of the final design configuration, a sensitivity analysis is performed. In this section, the sensitivity of the final design configuration is made with respect to a variation in one of the structural input parameters. The influence of all structural input parameters are qualitatively described in Section 3.4.3. The structural input parameters of the final design configuration are given in Section 3.5. The Mach number at which the model is tested is $M = 0.7$, as is described in Section 3.1. In this sensitivity analysis, a variation of ±5% is given to all input parameters. Based on this sensitivity analysis, the impact of a variation of each input parameter is analyzed. The output parameters for this sensitivity analysis are the buckling factor, the deformation of the tip, the von Mises stress, the natural torsion frequency, the natural bending frequency and the Mach number at flutter speed. In Equation 8.5 until Equation 8.9, the range of values for each parameter is given. After investigation on the impact of changing structural input variables, the most important output variables are analyzed individually to give an overview on how they are affected by the structural input variables. For this analysis, the buckling factor, the deformation, the von Mises stress and the bending and torsion frequencies are obtained using the Patran/Nastran software, whereas the Mach number at flutter speed is obtained via the aeroelastic model, as is described in Section 3.4.

$$2.85 \leq t_{skin} \leq 3.15 \qquad [mm] \qquad (8.5)$$

$$142.5 \leq c \leq 157.5 \qquad [mm] \qquad (8.6)$$

$$218.5 \leq L \leq 241.5 \qquad [mm] \qquad (8.7)$$

$$1995 \leq \rho \leq 2205 \qquad [kg/m^3] \qquad (8.8)$$

$$5.985 \leq E \leq 6.615 \qquad [GPa] \qquad (8.9)$$

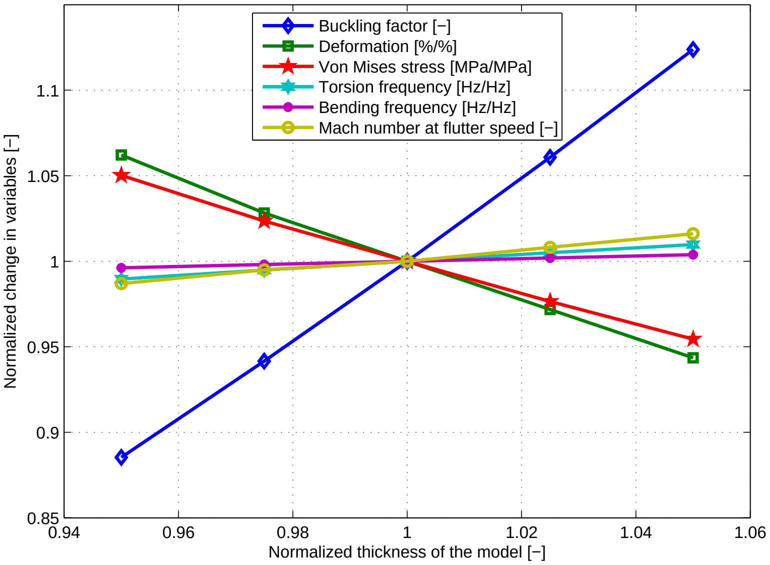

Figure 8.11: Influence of thickness on the final design variables

Thickness When manufacturing the model, there could be a slight offset in its skin thickness. To see the influence of this offset on the performance of the wind tunnel model, a sensitivity analysis is required. For the final design, the thickness of the model is $3mm$. For the sensitivity analysis, the thickness is varied from $2.85mm$ until $3.15mm$ in four steps of $0.075mm$. The results of the sensitivity analysis for the thickness are presented in Figure 8.11. In this figure, the input and the output variables are normalised according to the final design value. Therefore, the sensitivity of multiple variables can be combined in one graph. From Figure 8.11, it can be found that the buckling factor is most sensitve to changes in the thickness of the model. The buckling factor increases significantly with an increase in thickness. If the thickness of the model is increased by 5%, the buckling factor increases by 12%. The same relation holds in case the thickness decreases, meaning that the model experiences buckling earlier for a model with a lower thickness. However, the deformation and the von Mises stress decrease by 6% and 4% respectively, with an increase of 5% in thickness. The natural bending and torsion frequency, as well as the Mach number at flutter speed are less sensitive to changes in thickness, since the changes in these output variables are below 2%, with a change of 5% in thickness.

Chord Similar to the thickness, an offset in the chord length could occur during the manufacturing of the model. To see the influence of this offset on the performance of the wind tunnel model, a sensitivity analysis is also required on the chord length. For the final design, the chord length of the model is $150mm$. To perform the sensitivity analysis, the chord is varied from $142.5mm$ until $157.5m$ in four steps of $3.75mm$. The results for the sensitivity analysis of the chord length are presented in Figure 8.12. From this figure, it can be found that the deformation is the most sensitive to changes in the chord length of the model. The deformation decreases with an increase in chord length, which can be explained by the fact that the inertia and thus the stiffness of the model increases. The deformation decreases by 7% with an increase of 5% in chord length. The von Mises stress also decreases significantly (4%) with an increase in chord length of 5%, whereas the natural torsion frequency only decreases by 2%. Remarkably, the natural bending frequency increases (4%) with an increase in chord length (5%), which is in opposed relation to the natural torsion frequency. The Mach number at flutter speed changes no more than 2% with a change in chord length of 5%, whereas the buckling factor is the least

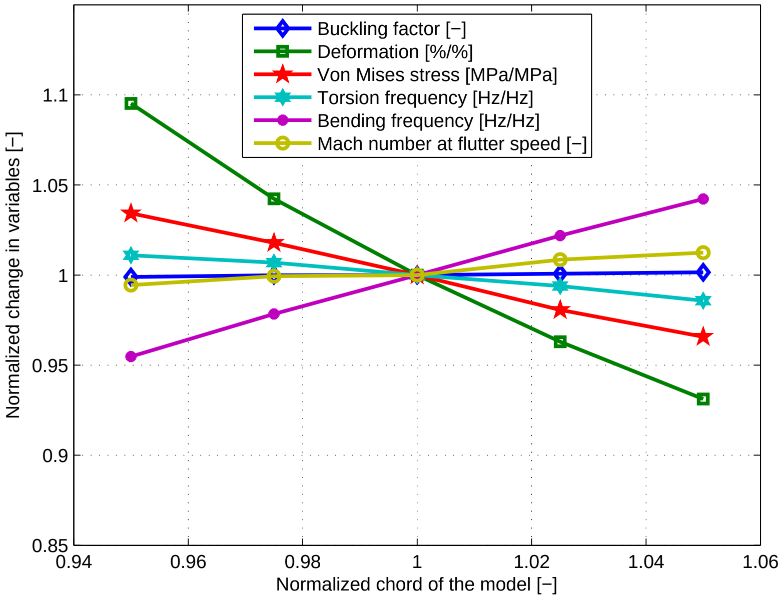

Figure 8.12: Influence of chord length on the final design variables

sensitive ($< 0.15\%$).

Length Similar to the thickness and the chord, the length of the model could also have an offset due to manufacturing of the model. To see the influence of this offset on the performance of the wind tunnel model, a sensitivity analysis is also required on the length of the model. For the final design, the length of the model is set to $230mm$. For the sensitivity analysis, the length of the model is varied from $218.5mm$ until $241.5mm$ in four steps of $5.75mm$. The results of the sensitivity analysis for the length of the model are presented in Figure 8.13. As can be seen from this figure, the output variables are quite sensitive to changes in the length. The buckling factor and the deformation are the most sensitive to changes in the length of the model. The model deforms 13% more if itl is 5% longer, whereas the buckling factor decreases by 12%. The von Mises stress increases significantly (8%) with an increase in length (5%). The natural bending frequency, the natural torsion frequency and the Mach number at flutter speed decrease by 8%, 5% and 1% respectively with an increase of 5% in length.

Density Next to the offset in the dimensions of the model, also the material properties of the model could have an offset. To see the influence of an offset in the material properties on the performance of the wind tunnel model, a sensitivity analysis is required. The first material property that is used for a sensitivity analysis is the density of the material. The material that is used for the final design is chopped roving glass fibre reinforced polyester with a 50% fibre volume content, which has a density of $2100kg \cdot m^{-3}$. Since this polyester type uses chopped fibres, the density of the material is different for different volume fractions of chopped fibres. Next to the volume fraction, also the density of the unsaturated polyester resin and the glass fibres could have a slight offset. For the sensitivity analysis, the density of the material is changed from $1995kg \cdot m^{-3}$ until $2205kg \cdot m^{-3}$ in four steps of $52.5kg \cdot m^{-3}$. The results of the sensitivity analysis for the density are presented in Figure 8.14. From this figure, it can be seen that the buckling factor, the deformation and the von Mises stress are not sensitve to a change in the density. Furthermore, the Mach number at flutter speed only changes by 0.5% with an increase in density of 5%. The only two output variables that have a significant change due to a

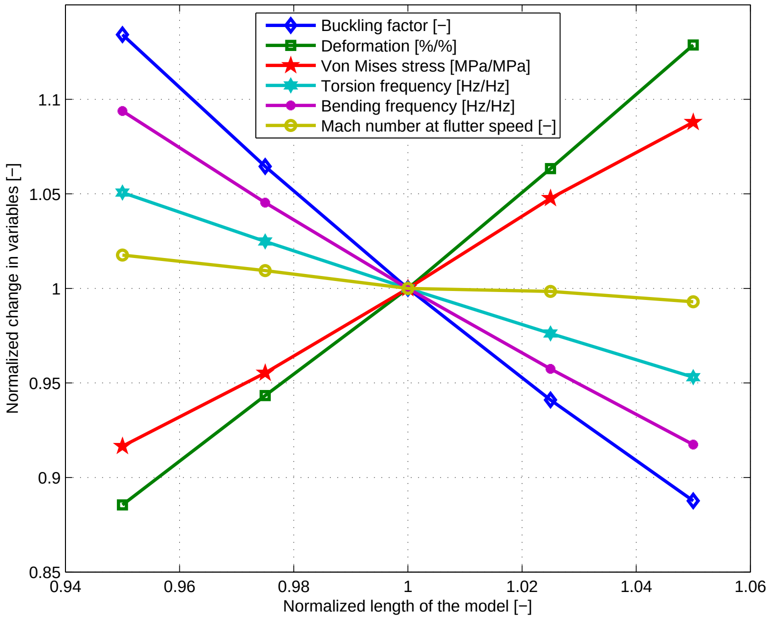

Figure 8.13: Influence of length of model on the final design variables

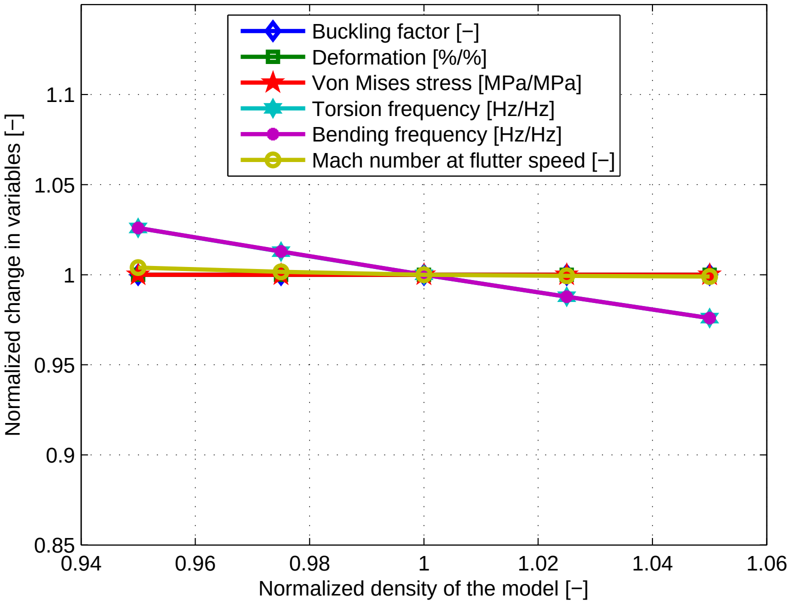

Figure 8.14: Influence of density on the final design variables

change in density are the natural bending and natural torsion frequencies. Both frequencies decrease by 2.5% with an increase in density of 5%.

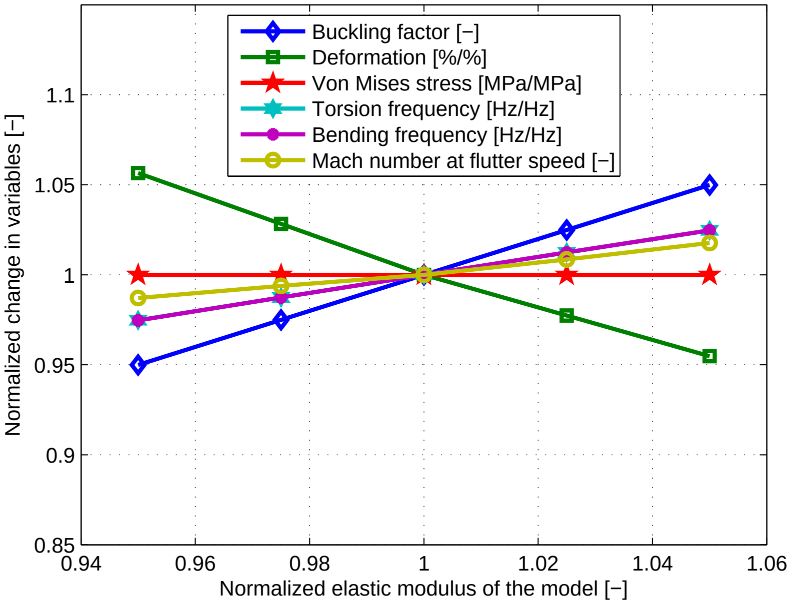

Figure 8.15: Influence of elastic modulus on the final design variables

Elastic Modulus The second material property that could have an offset is the elastic modulus. Similar to the density, the elastic modulus is dependent on the volume fraction of the chopped fibres in the polyester. Also, the elastic modulus of the material is assumed to be isotropic, due to the random orientation of the small chopped fibres. In reality, isotropic properties are difficult to achieve, which can have an influence on the elastic modulus of the material. To see the influence of an offset in the elastic modulus of the material, a sensitivity analysis is required. For the final design, the elastic modulus of the material is $6.3GPa$. For the sensitivity analysis, the elastic modulus is varied from $5.985GPa$ until $6.615GPa$ in four steps of $157.5MPa$. The results of the sensitivity analysis for the elastic modulus are presented in Figure 8.15. From this figure, it can be seen that the von Mises stress is not influenced by the elastic modulus, since the stresses only depend on the loading and the geometry of the model, whereas the elastic modulus is a material property. Also, it can be seen that the buckling factor and the deformation change approximately by the same value as the change in the elastic modulus (5%). However, the deformation decreases with an increase in elastic modulus due to the increased stiffness, whereas the buckling factor increases with an increase in elastic modulus. The natural bending and natural torsion frequency show the same relation with respect to the elastic modulus of the material. Both frequencies increase by 2.5% with an increase in elastic modulus of 5%. Lastly, the Mach number at flutter speed increases by 2% with an increase of 5% in elastic modulus.

Flutter Margin From the final design it is found that the model flutters at a Mach number of 0.766. The wind tunnel operates at a Mach number of 0.7 during the experiment, which means that the flutter margin is only 9.36%. Since the flutter margin is small, the Mach number at flutter speed is analyzed in more detail to get a better understanding of the influence of the geometry and material properties of the model on the flutter boundary. To analyze the flutter boundary, the flutter margin is plotted against the normalized structural input parameters. The results of this analysis can be found in Figure 8.16.

From this figure, it can be seen that the elastic modulus and the thickness of the model influence the model the most. As described in Section 3.6, it is hard to manufacture the model precisely, which

Table 8.1: Influence of the model parameters on the flutter margin

Parameter	t_{skin}	L	$\rho_{material}$	E	c
Deviation [%]	1.44	0.774	0.12	1.44	0.62

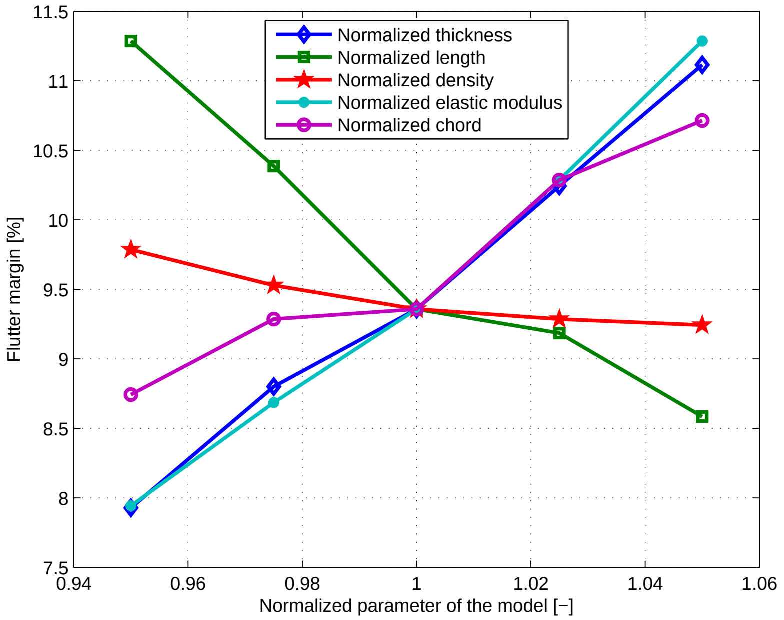

Figure 8.16: Flutter margin for different geometries and material properties

can have a large influence on the thickness, since the thickness is only $3mm$. Therefore, the thickness of the model must be manufactured with utter care, since the performance of the model is greatly dependent on the accuracy of the thickness. Note that the relation for the flutter boundary is not linear and superposition cannot be done, since the flutter boundary is dependent on eigenvalues that are obtained via the aeroelastic model using a state-space system. The maximum deviations of all parameters, that are changed by ± 5%, that lower the flutter margin with respect to the (9.36%) flutter margin for the non-varied structural parameters, are given in Table 8.1.

Since only small deviations are studied compared to the non-varied structural parameter, all deviations from the non-varied structural parameter value can be assumed to be independent of each other. This means that deviations can be approximated to be orthonormal to each other. The total error, σ, can be calculated using Equation 8.10.

$$\sigma = \sqrt{t_{skin}^2 + L^2 + \rho_{material}^2 + E^2 + c^2} \tag{8.10}$$

This gives a total deviation of 2.26%, giving a flutter margin of 7.10%. However, when running the simulation where all variables are changed by 5%, which decrease the flutter margin, the flutter margin will only by 4.72%. Therefore, it can be concluded that it is hard to distinguish the relation of each separate parameter and that the model should be manufactured with utter care to prevent offset in any of the design parameters. In addition, to see the influence of changing certain parameters, a new simulation should be run, since the separate changes cannot simply be added up.

8.2 Measurement Devices

In this section the performance and sensitivity of the measurement devices is analyzed. This section is different from the previous one for two reasons. First, the performance and sensitivity of measurement techniques is difficult to treat separately. Second, these two topics are more difficult to quantify, and the details given for the performance of measurement devices indicate orders of magnitude rather than precise values. In the following three sections the performance and sensitivity of the final design with respect to PIV, PSP and VMD are given.

8.2.1 Particle Image Velocimetry Performance and Sensitivity

The performance and sensitivity of the PIV set-up can be divided in the uncertainties arising from the technique itself, and uncertainties arising from the used tracer particles. These will be discussed simultaneously, as the uncertainty in the output (performance) is directly related to the influence of the uncertainties arising from the inputs (sensitivity).

The spatial resolution of PIV is dependent on the size of the interrogation areas [60]. The interrogation area is defined as an area in pixels, from which one flow vector is obtained. It is assumed that all particles move homogeneously. This is usually not the case however, and therefore the flow vector will only be an average of the velocities of the particles. The size of the interrogation area can be changed, and a smaller interrogation area can lead to more accurate velocity measurements. However, the interrogation window cannot be made too small, or the particle density per window will be too low. Typically, an interrogation area of 32x32px is used for PIV recording. With an image size of 1024x1024px, the spatial resolution will be $32/1024 \approx 3\%$ of the measurement area. Uncertainties also affect the determined flow velocity. Due to bias errors in particle location determination and random noise, the recording of the particles introduces errors in the computed flow velocity. The total velocity error can be assumed to be around 2% for stereoscopic PIV, based on previous experiments [60].

Due to the nature of the CO_2 particles, these will also be examined separately. The dry ice particles cool the airflow, which changes the temperature locally. This change is very hard to model in computer simulations, and can cause errors in the computations. It should also be mentioned that the temperature change also affects the PSP coating, but only slightly, according to [31]. Another uncertainty is due to the inconsistent size of the dry ice particles. In [31], Koike et al. reported that the particle size was estimated to be $1.2\mu m$ from previous research, but was actually larger because the particle size increased inside the feeding tube. Although larger particles are easier to detect, the traceability of the particles becomes wrong when the particle size varies.

8.2.2 Videogrammetric Model Deformation Performance and Sensitivity

The performance and sensitivity of the VMD measurement technique is related to uncertainties in target centroid measurements, camera calibration and data reduction [7]. The uncertainty related to the centroid measurement is caused by camera noise, target size and centroid calculation schemes. Bias errors occur in the centroid calculation, since the image centre of the VMD target is not the same as the geometrical centre of the target due to perspective imaging. The deviation can be as large as 0.3% of the target diameter and is dependent on the viewing angle of the camera, the size of the target, sensor size, and focal length [35]. The uncertainty related to camera calibration is associated with the used mathematical model and the accuracy of the numerical methods. Typically, the residuals of the accuracy of the camera calibration can be assumed to be around $1\mu m$ [7]. The uncertainty in data reduction includes the calculations of target locations, wing twist and bending. For example, with a one-camera VMD system, it is assumed that the model does not move laterally to calculate the other two components. Concerning the spatial resolution, a similar technique to VMD utilized by DLR gives an accuracy in the order of 0.01% of the field of view [49]. While this technique is not the same as VMD, it might give an indication of the spatial resolution obtainable with VMD as the techniques are related.

8.2.3 Pressure Sensitive Paint Performance and Sensitivity

Performance The performance of PSP is mainly driven by its accuracy. There are several factors that influence the uncertainty and therefore the accuracy of PSP. In large part, the accuracy of PSP is determined by its pressure sensitivity, which is the percentage change in luminescence with a change in pressure. As seen in the Stern-Volmer relation in Equation 6.1, the change in luminescence with pressure depends on coefficients $A(T)$, $B(T)$, $C(T)$, etc. According to Gregory et. al. in [21], the $B(T)$ coefficient is equivalent to pressure sensitivity. Moreover, Liu et. al. mention in [72] that a large $B(T)$ coefficient generally indicates a good pressure response [72]. However, Bell et. al mention in [4] that increased pressure sensitivity is achieved at the expense of luminescence output signal. In turn, a higher output signal can be achieved with a more powerful light source, although increasing the power excessively can cause an over saturation of the luminophore [72]. Finally, the sensitivity reported by Sugimoto et. al. in [71] for PC-PSP with PtTFPP luminophore and toluene as solvent is of $0.7\%/kPa$, while a sensitivity of $0.8\%/kPa$ has been reported for the same luminophore and an unspecified solvent by Sakaue et. al. in [64].

The coefficients named above are also influenced by the surface temperature on the model. Therefore, the uncertainty caused by temperature effects, or changes in luminescence with changes in temperature needs to be mentioned. This uncertainty is implicitly corrected for when calibrating the PSP results to the pressure transducers output. It is therefore limited to the uncertainty in the pressure transducer output, and in their coverage of temperatures. In [46], Nakakita and Asai reported a minimum accuracy of $200Pa$ for an anodized aluminium PSP, which is also a porous PSP. It is therefore assumed that the accuracy of this paint is similar to the accuracy of PC-PSP.

Additionally, there are other less quantifiable, and correctable sources of uncertainty. First, there are uncertainties in the photo-detector outputs. These stem from photon shot noise, dark current shot noise, amplifier noise, quantization noise, and pattern noise. When the dark current and pattern noise are subtracted and the noise floor is negligible, the detector noise is photon shot noise limited.

Furthermore, there is an uncertainty that results from the pressure resolution achievable by a paint. Disotell showed in [11] that the combination of luminophore and binder chosen for this experiment can achieve a pressure resolution of $52.7Pa$. More uncertainty arises from model deformation due to aerodynamic loads that causes a displacement of the wind-on image relative to the wind-off image. The uncertainty is caused by a change in the illumination intensity on the model surface after the model moves with respect to the light source. In addition, model deformation leads to a small change in the distance between the model surface and the camera lens.

Finally, uncertainties may arise from temporal variations in luminescence and illumination caused by sediments or exposure to light during non testing periods, filter leakage and pressure mapping errors.

Sensitivity The measurements that result from PSP are sensitive to a number of factors. First, the application of PSP coating to the model surface can alter the model's aerodynamic characteristics. The surface finish of the coating, its roughness and waviness, can alter the boundary layer and the coating thickness can alter the model geometry (e.g., wing leading-edge radius). At transonic Mach numbers, changes in the boundary layer can have an effect on shock location on the model surface. McLachlan et al. report in [39] that under transonic flow, the shock wave location can be changed with changes in the boundary layer attributed to PSP coating surface roughness. Therefore, the surface finish needs to be controlled with scrutiny.

Moreover, not only the finish of the coating needs to be controlled, but also the thickness and luminophore concentration. The Signal to Noise Ration (SNR) of PSP is directly proportional to thickness, and inversely proportional to the time response. Thus, as the paint thickness decreases, the luminescence emitted by the paint also decreases, thus degrading the SNR. However, thicker paints decrease the frequency response, thus a too thick paint layer may decrease the response below the desired one. The luminescent emission of a luminophore is characterized by the quantum yield (or efficiency); it is generally desirable to have as high a luminescent output as possible to maximize the

SNR of a photodetector. The luminescent intensity is proportional to the concentration of the probe molecules over a certain range. However, it cannot be increased indefinitely by increasing the dye concentration; if the concentration is too high, self-quenching of luminescence occurs [72].

Furthermore, the addition of the PSP coating layer has been observed in some test situations to affect the pressure tap readings [15], introducing a bias error in the tap measurements relative to the clean no-paint condition. This bias error is a measurement uncertainty factor when the in-situ calibration approach is employed [39]. Moreover, if there are large variations of temperature across the surface of the model, and the pressure transducers are outside the area of these variations, the temperature sensitivity of the paint may not be accounted for in the calibration [21].

Finally, one drawback of using PSP is the phenomenon of photo-degradation, where the luminescent intensity of the PSP deteriorates over time as the molecules are over-exposed to high intensities of light for an extended period of time [16]. The luminophore used in this experiment is PtTFPP, which is relatively photo-stable: the decay of luminescent intensity with continuous illumination is $1.5\%/h$. Nevertheless, care must be taken so as not to expose the paint to light outside of testing periods.

8.3 Compliance

The designed experiment is tested for its compliance to all requirements, as defined in Section 1.6. Table 8.2 shows all requirements and whether they are met or not. Next, the compliance of important and unmet requirements is discussed.

8.3.1 Requirements compliance

D1.4 The designed experiment focusses on the experiment to be performed. During the experiment, data is gathered rather than processed. Therefore, no information is available in this report on the confidence interval used for the data processing or on the noise added to the data during data processing.

D3 After the data is gathered, it is provided as input for computational solvers. Since the scope of this report does not include the processing of the data, the data format is not described. Therefore the compliance of this requirement is not yet described and met.

E1 During the experiment, for a single angle of attack, all measurements are performed simultaneously. Therefore no repeatability is expected. However, if the experiment has to be repeated for validation purposes, the experiment defines the accuracy of this repeatability. The actual accuracy follows from the new measurements being performed. Therefore it cannot be stated that this requirement is met, having performed this study.

The requirement also describes that the flow in the wind tunnel must be steady. Since the project has focussed on the design of the experiment, no tests have been performed to measure the flow of the chosen wind tunnel. Therefore it is unknown if the requirement is met.

E5 To identify and label all parameters in the data set, more information is required. The hard- and software to be used needs to be known, as well as the entire set-up of the measurement devices and connections. When all this is known, a complete measurement is performed for calibration and identifying the parameters in the acquired dataset. Therefore requirement E5.1 is not yet met.

M3 The defined surface roughness is based on a model being put in the flow, having low drag due to friction. The designed model meets this requirement. However, since PSP is applied, the surface is that of the PSP. The surface roughness of the paint is not documented, so the requirement is not necessarily met. Also the targets for the VMD measurement are placed on the skin of the model. This influences the surface roughness locally.

Table 8.2: Requirements compliance table

Id.	*d*	*Requirement*	*Compliance*
D		**Requirements pertaining to the data measurement**	
D1		The experiment shall provide accurate data on pressure and model deformation.	
D1.1	d	The obtained data should have a sufficient resolution for validation of the desired phenomena.	
D1.1.1		The measured pressure data must have a minimum sampling resolution of 14 dots per cm.	✓
D1.1.2		The pressure measurements must have a temporal resolution of at least 10 times the oscillation frequency.	✓
D1.1.3		The deformation measurements must have a temporal resolution of at least 10 times the oscillation frequency.	✓
D1.1.4		The pressure measurements must have a spatial resolution of at most $0.75mm$.	✓
D1.1.5		The deformation measurements must have a spatial resolution of at most $4mm$.	✓
D1.2	d	The employed measurement techniques must have a low systematic error.	
D1.2.1		The measurement bias of the pressure data based on amplitude must be less than $230Pa$.	✓
D1.2.2		The measurement bias of the deformation data based on amplitude must be less than $0.05mm$.	✓
D1.4		The data must be processed accurately.	
D1.4.1		The dataset must be processed with a confidence interval of 95%.	✗
D1.4.2		The processed experimental data must have a SNR of at least $40dB$.	✗
D1.5		The employed measurement techniques must have a high enough sensitivity.	
D1.5.1		The pressure must be measured with a sensitivity of at least $230Pa$.	✓
D1.5.2		The deformation must be measured with a sensitivity of at least $0.05mm$.	✓
D2	d	The experiment shall provide relevant measurement data and boundary conditions for numeric FSI solvers.	
D2.2		The experiment must measure the deformation of the model.	
D2.2.1		The experiment must measure the twist of the model.	✓
D2.2.2		The experiment must measure the model deflection.	✓
D2.3		The experiment must measure the frequency of at least the first bending mode and the first torsion mode of the structure.	✓
D2.4		The experiment must measure the position of shock waves along the chord and in span-wise directions.	✓
D2.5		The experiment must measure the pressure distribution along the chord and in span-wise directions.	✓
D2.6		The boundary conditions provided by the experiment must be reproducible in computational models.	✓
D2.7		The running time of the experiment should allow for the completion of an entire measurement set.	✓
D3		The measured data must be provided in a format that allows for its input into computational solvers.	✗
E		**Requirements pertaining to the experiment**	
E1		Free stream flow conditions (pressure, temperature, density) must be constant during the experiment.	
E1.1		In case of required repeatability, the deformation and a boundary condition at a reference point may not differ by more than 1%.	✗
E1.2		The flow in the wind tunnel test section must be steady.	✗
E2	d	The experiment must take place in transonic conditions, at a Mach number between 0.5 and 1.	✓
E3	d	The experiment must take place at a Reynolds number of at least 10^6.	✓
E5		The experiment description must be clear, correct and follow a logical sequence.	
E5.1		The parameters in the data set must be clearly labeled and explained.	✗
E5.2		Any possible source of error must be documented.	✓
E6	d	The experiment must provide data that is relevant for transonic transport aircraft.	✓
M		**Requirements pertaining to the model**	
M2	d	The model and the mount must fit in the test section of the selected wind tunnel.	✓
M3		The surface roughness of the finished model should be at the most $0.20\mu m$.	✗
M4		The manufactured model must have tolerances no larger than $0.1mm$.	✓
M5		The area blockage in the wind tunnel due to the model should not be more than 5% of the tunnel section concerned.	✓
M6		The amplitude of the models tip deflection must have a maximum of 10% of the model length ($23mm$).	✓
M7		The model must have a buckling factor of at least 2.	
R		**Constraints and requirements on resources**	
R1		The safety of all personnel must be guaranteed during the experiment.	✓
R2	d	The wind tunnel integrity must be maintained.	✓
R3	d	The budget for the experiment shall not exceed €50,000.	✓
R4	d	The experiment must be performed at the TU Delft.	✓

8.3.2 Validation Data

In Section 1.4, different levels of validation data are outlined. The most important data that have to be provided by this experiment are the validation data contained in level zero, namely the wind tunnel boundary conditions, pressure on the surface of the model, flow velocity in the test section, deformation of the model and model geometry and characteristics. This subsection provides the means of obtaining these level zero data, together with their specifications.

Wind Tunnel Boundary Conditions In order to obtain the boundary conditions related to the wind tunnel, the complete geometry of the wind tunnel is provided, together with the static conditions in the settling chamber. In this way, any interference of the model with the flow can be modelled. This option is chosen, since there is no location along the wind tunnel at which a full set of steady conditions can be measured, except for the settling chamber. This is the reason why the test section cannot be modeled separately in the FSI solvers.

Pressure on the Model Surface The pressure on the model surface is obtained from the PSP measurements. The PSP can measure changes in pressure as low as $57Pa$. The nominal spatial resolution achieved, considering the camera used, is $0.75mm/pixel$. In case a higher resolution is necessary, different lenses and camera orientation can be implemented. The temporal resolution, aiming for a resolution not lower than the resolution of flow field velocity measurements, while maintaining sufficient exposure time, is set at $2700Hz$. The PSP is applied on the top surface of the model. In order to obtain the pressure on the bottom surface of the model, the experiment can be performed at negative angles of attack. Since the experiment uses a symmetric airfoil, data recorded on the top surface at these negative angles of attack are representative for the pressure distribution on the bottom surface of the model, at positive angles of attack.

Flow Velocity in the Test Section The velocity field around the model is measured using the stereoscopic PIV system. The spatial resolution is 3% of the measurement area. The temporal resolution of these measurements is the same as for the PSP system, namely $2700Hz$. The width of the area illuminated by the lasers has a thickness of at most $2mm$. In case the flow velocity needs to be measured at multiple locations, the PIV system has to be repositioned and recalibrated.

Deformation of the Model The deformation of the model is measured by the VMD system. The locations of the targets is discussed in Section 6.3. The spatial resolution is at most $4mm$ and the time resolution is the same as for the other measurement techniques, $2700Hz$.

Model Geometry and Characteristics The exact geometry of the model is needed to reproduce the experiment in the FSI solver. A detailed CAD drawing is provided, together with the material properties, surface roughness, exact positioning of the model and the measurement devices.

As a conclusion, it can be seen that the experiment provides all the level zero data required for the validation of the FSI solvers. From the level one validation data, only the exact geometry of the mount system is provided.

Chapter 9 — Cost and Risk Analysis

At this point, the design of the experiment is defined, and its performance analyzed. There are two other very important factors that have to be taken into account before further research is performed on the topic: the cost of the experiment and the incurred risks. These factors are carefully considered during the design process, and are presented in this section. First the costs are summarized, followed by an explanation of the risk factors.

9.1 Cost Analysis

With a final design in place, it is possible to estimate the cost of producing the model and preparing it for the experiment. The cost consists of four main components: model material, production equipment, labour and measurement techniques cost. These components are described in the paragraphs below. This section concludes with a final cost estimation.

Model Material and Production Equipment Cost The chopped glass fibre roving reinforced polyester costs 4.35€/kg. With an estimated model weight of $0.409kg$, the raw material cost is €1.78. However, since more material is used during manufacturing, for example excess resin that is removed or resin that is prepared but not needed, the raw material costs are higher. Assuming that the minimum amount of material that can be purchased is $5kg$ and considering a minimal shipping fee, the estimated material cost is €30. Additionally, as mentioned before, to satisfy the surface roughness requirement, lapping film is used. Diamond lapping film 661X, which is a product created by 3M, can achieve a surface roughness of $0.1\mu m$. 25 sheets, which is the minimum quantity, can be ordered for €140 [25]. It is assumed that this amount is sufficient for our purpose. Moreover, depending on whether it is available at the TU Delft, a spray-gun needs to be bought. A chopper gun, which does not automatically spray the resin, costs approximately €300, which forms a lower bound of this cost. Finally, based on [45], a mould intended for spray-up costs €500.

Labour Costs The total time it takes for creating two halves of the model is approximately 30 hours, including curing. However, only approximately 9 hours include manual processing. This time estimate assumes the use of an autoclave for the curing of the model [1]. Since an autoclave is not used, the total time for manual processing is reduced to 8 hours. Determining the amount of time it takes for refining both the outer and the inner surface is difficult, however it is estimated to take several days. Polishing the outer surface to the required surface roughness needs to be done in several steps, with each step requiring attention. Refining the inner surface for thickness purposes requires grinding and measuring whether the required tolerances are met. This is a time-consuming process, as it needs multiple measurements to see if the requirements are met. Moreover, grinding of a composite is a slow process. These processes take approximately 6 working days. The assembly of the model itself is assumed to take half of a working day, assuming that all the individual parts meet the set requirements. Considering an hourly cost of €40 per hour, the labour cost is estimated to be €2,400.

Measurement Techniques The cost for measurement techniques is in turn separated into PIV, PSP, and VMD costs. The cost related to stereoscopic PIV are minor for this experiment. The cameras of the TU Delft can be used without cost, so only the dry ice contributes to the cost for PIV. In [36], the liquid CO_2 was stored in a $180L$ dewars, which was then fed directly into the feeding

Table 9.1: Overview of costs

Element	**Costs**
Model raw material	€30
Lapping film	€140
Spray-gun	€300
Mould	€500
Model manufacturing	€2,400
Liquid CO_2	€70
PSP paint and application	€1,000
LED array	€3,800
Pressure transducers	€900
PSP software	€15,200
VMD targets	€500
VMD software	€6,000
Total	€30,840

tube. CO_2 recipients typically used in restaurants can also be utilised. These are produced in much smaller sizes: between a few hundred grams and several kilograms. In [31], a mass flow of $6.6 grams/s$ LCO_2 was obtained from a $0.5mm$ orifice, whereas $26.4 grams/s$ LCO_2 was obtained with an orifice of $1.0mm$. With this in mind, and taking the total of 8 minutes run-time of the experiment into account, the maximum required weight for the LCO_2 is $12.6kg$. This costs €70 in terms of restaurant type CO_2 recipients. The costs related to PSP are comprised of the materials and equipment required to apply the paint, the light source, the pressure transducers required for calibration and the processing software. The cost for the paint and its application is difficult to estimate, but it is assumed to be €1,000. The LED array offered by ISSI costs €3,800. The cost of three pressure transducers is €900. Finally, purchasing the complete package of PSP analysis software from ISSI costs €15,200. The costs related to VMD are comprised of the targets to be applied on the model and the software required for VMD analysis. The cost of the VMD targets and their application is assumed to be €500. An estimate for the VMD software cost can be made based on the cost of the ProGraph software included in the PSP software package, which generates structural meshes. Based on this, the VMD software cost is estimated at €6,000. It must be noted that the costs related to the software can be considered a long term investment for the experiment owner. Therefore, in an alternate cost analysis, it may be possible to amortize this cost across a certain number of experiments that the software would be used for.

Finally, the total cost of the model can be calculated. This is illustrated in Table 9.1, with the values rounded up to the next euro. It must be noted that total cost in this table relates to the first produced model. In case that the model fails during the experiment, breaks during production or handling, or does not meet the design standards, producing a new mode only involves additional costs related to raw material, lapping film, labour, PSP paint and application, and VMD targets. Therefore, the cost of the second and additional models are €4,070.

9.2 Risk Analysis

The risk analysis of the experiment is divided into five distinct parts. Firstly, the general experiment and validation data risks are explained. Then, the risks pertaining to the model are considered, followed by the mount and the actuation system risks. Finally, the risks regarding the measurement techniques are evaluated.

9.2.1 Validation Risks

Several risks stem from the data that has to be provided for the FSI solver validation. Most of these risks are related to incorrect measurements, and are described in Section 9.2.6.

However, there is one major that can be considered separate from these: the risk that the boundary condition data provided on the wind tunnel is incorrect. The data is provided through a CAD drawing of the entire wind tunnel and a measurement of the conditions in the settling chamber. There is a risk that the CAD drawings provided for the FSI solver are slightly different from the real wind tunnel. This error can propagate and affect the boundary conditions used for the FSI solver. This causes the solvers to use different data from the experimental values, and large divergence can occur. By knowing the exact manufacturing accuracy of the wind tunnel, one can be able to estimate the error and account for it within the FSI solver. Similarly, if the measurements of the conditions within the settling chambers are erroneous, it greatly affects the boundary conditions and therefore the FSI solver accuracy and relevance.

9.2.2 Model Risks

There are several risks directly related to the model. Over the course of this section, they are detailed and explained.

Failure The most critical risk pertaining to the model is the risk of failure. Failure of the model can have large consequences for the experiment, such as damage to the wind tunnel or the impossibility to obtain the desired data. This failure can occur in three primary ways: structural failure (yield or buckling), impact with the wind tunnel walls and model assembly failure.

The model is designed in such a way to prevent failure in yield and buckling with a safety factor of two, as described in Section 3.3. In this section, the load calculations are based on an angle of attack of 3.6°, the maximum static angle of attack described in Chapter 7. However, the angle of attack increases above this value during the aeroelastic oscillations, as shown in Section 8.1.2. Since the slope of the $C_L - \alpha$ curve is linear, and the maximum lift coefficient does not exceed 0.8 at $M = 0.7$ [70], the maximum load always falls within the defined safety factor of 2, and the model does not fail due to excess lift load.

For skin buckling, a buckling factor of 2 is taken, and therefore the model only begins to buckle if the load increases to double the original value. However, the effects of a twist of the model on the buckling are not well studied and could prove to be of influence. This must be taken into consideration in any further study of this experiment. The buckling calculations are performed numerically using Patran/Nastran, and therefore there are modelling errors present. In terms of meshing, the use of a finer mesh only increases the buckling factor, and therefore the values are a reasonable lower estimate. The model used is a shell with open ends. When the ends are closed, the buckling factor increases by approximately 5%, which means that the performed analysis is still a valid conservative estimate.

The second failure risk is physical impact with the wind tunnel. This can occur due to two causes: excess deflection and failure of the mounting system. For the first cause, both requirement M6 and the chosen length prevent the model from touching the top and bottom walls, as described in Section 3.2.1. Secondly, should the mount fail, the model is made out of a material with a considerably lower toughness than the steel wind tunnel walls [10] and this safeguards them from any impact. However, the wind tunnel windows are made of a considerably less tough material. Therefore, to minimize the risk of an impact destroying them, the length of the model has a safety distance of $5cm$ from the wall, as shown in Section 3.2.1.

Finally, the model is produced by spray-up moulding of two halves, which are then bonded together with adhesives, as described in Section 3.6. Due to the small scale of the model, the contact area between the two halves is very small, and therefore care needs to be taken during the production process, in order to prevent a separation of the model. In addition, if further research is performed on the experiment, the adhesive-structure interaction is an area that can benefit from additional analysis.

Aerodynamic Effects The size and structure of the model has a large effect on the aerodynamics around it, especially in a small scale wind tunnel such as the TST-27. The interference of the model on the flow must be minimized. This interference is mainly caused by four factors: the length and thickness of the model, the Reynolds number and the airfoil.

When the model length causes its tip to be too close to the wind tunnel wall, the airflow is effectively blocked, which influences the velocities and pressures measured. This is accounted for with a safety factor, as described in Section 3.2.1. However, even without the wall, there are still tip effects such as vortices and flow mixing present. This means that any pressure and velocity data taken near the tip is less accurate, and this needs to be taken into account. However, the FSI solver should also be able to model these effects, mitigating this risk.

The thickness causes a similar effect. A thick airfoil reduces the effective area of the test section, as seen in Section 2.2. This increases the local velocity of the air, causing differences between the measured data and the expected results. These effects are considerably reduced with a model area blockage of lower than 5%, which is specified by requirement M5.

The Reynolds number influences what phenomena occur on the model. In order for the experiment to be as relevant as possible for transonic flight, it is desired that the Reynolds number is as large as possible, and requirement E3 species that the minimum Reynolds number is 10^6. Due to the high total pressure in the wind tunnel, this value is easily achieved, making this risk negligible.

The airfoil is a key factor in determining the critical Mach number of the flow on the airfoil. Since the experiment has as a goal measuring aeroelastic effects in transonic flow, it is essential that shock waves form over the airfoil. In Section 3.1, the angle of attack necessary for the critical Mach number to be the experiment Mach number of 0.7 is found to be 1.89°. The experiment is set up to cover the range of 1.2° to 3.6° in Chapter 7, meaning that the desired effects are present. This is also confirmed in section Section 8.1.1, and therefore this risk is mitigated.

Manufacturing There are also risks associated with the manufacturing of the model. These can be grouped into four categories: the layup process, the assembly, the machining and the handling.

In terms of the layup process, the spraying procedure needs to be monitored accurately due to the risk of anisotropy in the material. The orientation of the glass fibre reinforcements must be as random as possible, otherwise the material properties are not the same as calculated and the model may behave in unexpected ways or even fail prematurely. In addition, the surface thickness is difficult to control during such a process. This is mitigated by manufacturing with a safety factor applied to the thickness, followed by precise measurements after manufacturing and, if necessary, additional sanding of the inside of the model to remove excess material. Finally, the two parts of the polyester, the resin and the hardener, must be mixed in the correct proportions. If an error is made in this process, the resin does not solidify correctly and cannot be used. Therefore, the weights of the two parts must be carefully monitored when mixing, and if any error occurs, the proportion must be matched by adding the necessary part.

In terms of assembly, one of the risks is the failure of the bonding, as described above. In addition, during the bonding process the two halves need to be matched exactly, and the seal must be airtight, to prevent any unwanted disturbances in the flow. This must be inspected after manufacturing in order to confirm that no errors are made during the process.

The machining risk comes from the precision and the material temperature sensitivity. The tolerances for the precision of the machining are set up in requirement M4 to be $0.1mm$ and must be followed strictly. If for example a drilled hole does not match this tolerance, the model needs to be manufactured again, which affects the cost and scheduling. Additionally, during machining, special care must be taken to not damage the polymer structure. To prevent this, the machining must be done at a low speed, and the temperature must be watched closely, in order for it not to exceed $190°C$, the maximum processing temperature of the polyester.

Finally, the model must be handled with care, as any impact can affect the surface roughness greatly, and can damage the pressure sensitive paint. An excessive surface roughness, as defined in requirement M3, can affect the quality of the validation data.

Analysis During the course of the design process, a number of assumptions are made to simplify the analytical calculations. This can have effects on the accuracy of the results.

In Section 3.3.1, it is stated that the deflection is not allowed to be larger than 10%, as within that range the deflection can be assumed to be linear without shortening effects, and the lift is assumed to act in the vertical direction with respect to the wind tunnel floor. However, this is not entirely accurate, as there are always deformations of the model when bending, and any deflection causes the lift to not be exactly vertical. The lower the deflection, the smaller these effects are. Since the different direction of the lift only reduces the vertical component, this is not a danger for failure. The safety factor of 2 is still applicable to prevent failure due to any unforeseen deformations. Since failure of the model can be prevented in this way, any other deviations from the predicted effects are not as critical, as they can still be measured and accounted for.

However, the measurability of the experiment is a critical factor. The frequency is confirmed with the use of Patran/Nastran numerical methods. These methods have inherent modelling errors. However, since the frequencies are low enough to measure, as shown in Section 3.5, even a large modelling error still puts the frequencies within the camera range. Additionally, in case the frequencies do exceed the camera range, it is possible the increase to camera's sampling rate, at the expense of its resolution.

9.2.3 Aeroelastic Risks

The risk involved in the aeroelastic behaviour of the model consists of two aspects: insufficient theoretical approach and faults in manufacturing.

Insufficient Theoretical Approach The theory used to describe the aeroelastic behaviour is obtained from [30]. Moreover assumptions are made for the aerodynamic model, as well as for the aeroelastic model. These assumptions can be found in Section 3.4.1. For the aerodynamic model, the theory from [30] was assumed to be a sufficient representation to determine the aeroelastic behaviour. The risk is that this may be overly simplified and that in test conditions it does not represent the aeroelastic behaviour accurately.

To implement this, experimental data was used from [70]. This data is assumed to be verified and validated, and correct. If this is not the case, or if the results have slight errors, this may severely impact the final response of the system. Moreover, this model is linear. If the changes in angle of attack or pitch rate are too high, the theory is not valid anymore. Also it was assumed that the elastic axis lies at a quarter chord point. This is used for a first order simplification. In further studies, this risk should be eliminated by incorporating the exact position of elastic axis. For the aeroelastic model it was assumed that there was no structural damping in the system. This does not give higher risks, since the model is undamped for lower Mach numbers. This assumption can be seen as a safety factor for the flutter margin. Finally, it is assumed that the uncoupled natural bending and torsional frequency obtained from Patran/Nastran are representative for the aeroelastic model. If there are errors in these calculations, the flutter boundary may change.

Manufacturing Errors Errors in manufacturing can have a large influence on the aeroelastic behaviour. Since the flutter margin is very important to monitor, for this parameter a sensitivity study was performed. In Figure 8.16, the results can be seen. The results of this figure are given in a 'ceteris paribus' manner, meaning that the effect of the flutter margin is given for the change of each individual parameter. It can be seen that if the elastic modulus or thickness decreases by 5%, the flutter margin already decreases by 1.44%. The elastic modulus is a direct result of how the glass fibers are sprayed and which direction they have. Moreover, during manufacturing it is difficult to have the low tolerances in thickness, as explained in Section 3.6. Since only small deviations are studied compared to the non-varied structural parameter value, all deviations from the mean value can be assumed to be independent of each other. This means that deviations can be approximated to be orthonormal to each other. Based on this assumption, the final flutter margin is 7.10%, see Chapter 8. The Mach number can be controlled within a Mach number of 0.002 [76]. This gives a flutter margin of 0.285% with respect to the Mach number at which the model is tested, $M = 0.7$. If the wind tunnel is started, the wind tunnel can have an overshoot with respect to the Mach number. The experimental strategy to reach this Mach number is therefore to first set the wind tunnel at $M = 0.5$ and then steadily increase the Mach number until $M = 0.7$. With this approach the Mach number can be accurately controlled within 0.002. Based on this, the risk of the occurrence of flutter is minimal if all parameters can stay within the ±5%. However, care has to be taken with respect to the model skin thickness. The influence of the thickness on the flutter risk is expected to be the most important, since it is difficult to achieve an exact thickness when producing the model with respect to faults in manufacturing. Therefore, this must be monitored accurately during manufacturing.

9.2.4 Mount Risks

The mount has two major sources of risk: the risk of breaking, and the risk of incorrect positioning.

Failure Due to the fact that the mount holds the model in place, it is of crucial importance for the realization of the experiment. The mount is designed in such a way that its strength is much larger than the model's, and the model will always fail before the mount.

Positioning In Chapter 7, the variation of the angle of attack with the experiment is described. In order to achieve this variation, the clamp must be unbolted, rotated and reattached. This is an operation performed by a human, and therefore there will always be inherent errors. As described in Section 4.3, the mount is bolted to a slider, and the exact position will determine the angle of attack of the model. In order to make this more accurate, one possibility is to incorporate a scale of possible angles on the mount for visual reference, measuring the angle exactly to design this scale.

9.2.5 Actuation Risks

There are several risks associated to the actuation system, thes are failure, aerodynamic effects and installation.

Failure The flap mechanism is not designed in thorough detail. This leads to an increased amount of uncertainty, which also increases the risk of failure occurring in this part of the model. The flap itself is attached to the main model by means of a small bar. Due to the loads on the flap, there is the risk for this bar to fail. This will have large consequences for the experiment since the model cannot be actuated and therefore it is not possible to perform the experiment. Another part of the of the mechanism that can fail is the attachment point of the wires with the flap. Due to the limited amount of space available inside the flap, there is also little free space for attachment points. These points must therefore be very small which makes them prone to failure. The same holds for the pulleys that are placed closer towards the leading edge of the model. These pulleys need to be attached to either the top or bottom surface in the model. Due to the limited space available, the supports of the pulleys must also be small. To reduce the chance of failure, the two pulleys are attached, which increases the stiffness of this part of the mechanism. The tension forces in the cable need to be withstood by the pulley supports, which are also prone to failure. The wire connecting the flap to the servo through the pulley can also fail. Care must be taken that the tensile stresses occurring in this wire do not exceed the tensile yield strength of the material of which the wire is made.

The hinge runs along the length of the flap. Due to the deflection of the model, the hinge can bend. This bending can result in the hinge deforming plastically after which it will no longer be able to rotate. This will have as a result the loss in functionality of the entire flap mechanism.

Aerodynamic Effects Undesired aerodynamic effects can occur due to the fact that there is a gap between the flap and the model itself. Flow disturbances can occur at the location of this gap and one must take this into account when designing the flap in more detail. An attempt is made to reduce this aerodynamic effect by curving both the rear of the model and the front of the flap, which in turn reduces the gap between the flap and the model. Another aerodynamic phenomenon that can occur at the flap are shock waves. These can have a large effect on the loads acting on the model which in turn affects the loads on the overall flap mechanism.

Installation The subsystems belonging to the flap mechanism are very small. There is a risk in positioning them accurately at the specified position. Locating them at a different location will have as result that moment arms can change, which alters the torque required to displace the flap from its position.

9.2.6 Measurement Techniques Risks

Particle Image Velocimetry PIV risks are mostly related to data acquisition. The camera usage is one of these risks. There is only a limited amount of cameras that can be placed at the window of the wind tunnel at any time. Improper calibration can deteriorate the image quality and give erroneous velocities. Finally, the usage of a laser induces risks. Not only may it harm the person performing the experiment, but errors can occur in the data if the location of the laser is not well known, or if the laser sheet is too spread out to measure accurately. Risks related to data processing also need to be taken into account. As two PIV cameras will be used, which each record eight gigabytes of flow data per second for six minutes [55], at least 5.7 terabytes of data will be generated over the course of the experiments. Another risk to consider is the cooling effect of the dry ice particles. This can cause local velocity drops, although Koike et al. mention that these differences in the flow are negligible [31].

Videogrammetric Model Deformation Being an optically based measurement technique, the same risks for the cameras of VMD as the ones mentioned for PIV apply. The main difference, and therefore the increase in risk, will be due to the deformation of the model. Inaccurate measuring of the displacement of the targets is another big risk. The target displacement is used to calculate the model displacement and indirectly the first bending and torsion mode. Errors in measuring the target displacements propagate to the latter. The tip displacement also cannot be too large, otherwise the tip blocks the view for the targets further away from the camera.

Pressure Sensitive Paint The coating used for the PSP may affect the aerodynamic properties of the model which may be difficult to quantify and implement in the FSI solvers. If the coating is not applied uniformly, the response and luminosity will differ over the model, as these depend on the thickness of the coating. Also, the coating consists of toxic substances that need to be handled with care during the placement process. Lighting is also important for the PSP, as the laser light activates the PSP luminophores. If the lighting is not strong enough at certain parts of the model, the response will also be weaker, which leads to incorrect results. As for the cameras, the same risks will be incurred as for the PIV.

Pressure Transducers The pressure transducers will also introduce additional risks into the model. They will affect the aerodynamics of the model locally as the surface becomes uneven because of them. Also, due to the size of the model, it will be challenging to install the pressure transducers inside the model.

Chapter 10 — Conclusion and Recommendations

This section of the report contains the conclusion of the research described in this report and the recommendations on further improvement. The conclusion will contain the main achievements of this research and will give an overview of the final design. In the recommendations section, some directions are stated in which the final design could be improved, and areas for future research are discussed.

10.1 Conclusion

The goal of this project is to design an experiment that provides experimental data for the validation of FSI solvers in the transonic regime. Furthermore, this report looks into the feasibility of such an experiment being conducted in the TU Delft facilitites. The main disadvantage of conducting an experiment at the TU Delft in the transonic regime is that the available wind tunnels are relatively small. The challenges that arise from the dimensions of the wind tunnels are the low Reynolds number, the limited space for measurement devices and the high natural frequencies of the model.

Following a preliminary study on wind tunnels, the experiment is designed to be conducted at the TST-27 at the TU Delft facilities. The wind tunnel model has a simple rectangular planform with a chord of $150mm$, a length of $230mm$ and a skin thickness of $3mm$ and uses the NACA 64A-010 airfoil. The material that is used for the model is chopped roving glass fibre reinforced polyester, which has a density of $2,100kgm^{-3}$, an elastic modulus of $6.3GPa$ and a Poisson's ratio of 0.342. The wind tunnel model is attached to the wind tunnel wall via a clamped mount, taking up one of the two windows in the TST-27 wind tunnel. To actuate the model, a flap is used to deform the tip of the model by a minimum of $10mm$. To actuate this flap, an electric servo motor is used to control a pulley system, which in turn rotates the flap. To provide validation data during the experiment, three FASTCAM SA1.1 cameras are required to observe the model via PSP, VMD and PIV measurement techniques. PSP is used to measure the pressure on the top surface of the model, VMD is used to measure the deflection of certain targets on the model and PIV is used to measure the velocity around the model. Furthermore, three pressure transducers are integrated in the model in order to calibrate the PSP. The model is manufactured using a manual spray-up technique, which is post processed with automated grinding and manual polishing.

The experiment provides measurement data on aeroelastic oscillations. The model is designed in such a way that other aeroelastic phenomena, such as flutter and buffeting, do not occur during the experiment. Flutter is prevented by designing the model such that the flutter boundary stays above the operating Mach number, which is set to $M = 0.7$. The flutter boundary is found using a aeroelastic model, which is implemented in MATLAB. To prevent buffeting, the flow upfront the wind tunnel model in the test section is kept undisturbed. The cameras are able to measure the first bending and the first torsion mode of the model to improve the quality of the validation data. Furthermore, the model is designed to sustain twice the maximum predicted loading on the model for stress as well as buckling considerations. The requirement for the deflection is set at maximum 10% to keep the lift distribution vertical and to neglect the shortening of the model due to the deflection. With this 10% limit, the deformation is significant, while the structure still behaves approximately linear. The model is found to deform by 7.7% under the maximum loading.

10.2 Recommendations

In this report the design of the T-FLEX wing experiment is presented. To perform the experiment, and provide the experimental data for the validation of the FSI solvers in the transonic regime, more research still has to be performed. For each major aspect of the design process, recommendations for further research have been outlined. These recommendations are discussed and explained in more detail in the following sections.

10.2.1 Wind Tunnel

Currently, the entire wind tunnel geometry must be provided as boundary conditions for the FSI solvers, since it is not known at which location the flow is completely steady. For further research, it is recommended to study in full detail at which locations the flow is steady. When this information is available, these locations in the wind tunnel can represent boundary conditions for the FSI solvers.

10.2.2 Model

The model described in this report is a simplified wing compared to that of commercial airliners. This is chosen to introduce less complexity in the model. As a result, the behaviour of the model is easier to predict and there is less uncertainty in the entire design. For further research, the model may be designed in more detail to increase the relevance of the experiment to commercial transonic transport aircraft. Therefore, the aspect ratio can be increased. For the final design, the aspect ratio is 3, whereas commercial aircraft generally have an aspect ratio between 9 and 12. Moreover, there is no taper in the final design, whereas commercial aircraft in general do have a taper ratio. The wing can be made more realistic by adding taper. In addition, a sweep angle can be added in the design of the model. A wing with sweep has a higher bending moment near the tip, causing a higher degree of coupling between the bending and torsional oscillation modes. By adding sweep in further research this higher degree coupling can be researched. Finally, in the current design, the ratio between the first natural torsion frequency and the first natural bending frequency is 3.44. In general, this ratio is close to 2 [67]. Tuning the model closed to this ratio makes it more representative for a wing of a commercial airliner. .

To calculate the first and second area moment of inertia, polynomials of the contour of the airfoil are used. These polynomials have offsets in their results. Moreover, since no taper is present in the wing design, the inertias are calculated with a two-dimensional model. However, since a flap and measurement devices are present in the model, these inertias are not constant along the span. For further research it is recommended to calculate these inertias more accurately.

The natural bending and the natural torsional frequencies used to calculate the aeroelastic behaviour of the model are calculated with Patran/Nastran. The simulation performed by using Patran/Nastran is an approximation of reality, since the numerical solver is based on assumptions. In addition, the accuracy of the model is dependent on the mesh on the surface of the model and the loads and boundary conditions, which adds to the uncertainty. In Patran/Nastran, the pressure distribution is simulated by ten equally placed pressures along the chord. This is done to make a first order approximation of the structural modes. For further research, however, it is recommended to increase the number of points along the chord, so that the pressure distribution is more continuous and represents reality more accurately. Also, in Patran/Nastran, the wing is modelled by a shell with a $3mm$ skin thickness. By using a shell, Patran/Nastran approximates the model by a thin walled assumption. Since the skin is $3mm$ thick, this introduces errors. For further research, it is recommended to more accurately represent the model in a FEM. Furthermore, in this report and in the Patran/Nastran model, the model is open at the tip. The points at the contour of the tip are fixed with respect to each other. This is an additional simplification to make the model easier to simulate, but also introduces errors, since with a closed model, the points at the contour of the tip may have a slight displacement with respect to each other. Therefore, it is recommended to close the model in further research. Finally, in the Patran/Nastran simulation, the actuation system and the flap are not included. For further research, it is highly recommended to incorporate this in the model. To optimize the modes, more research can be done by varying the thickness along the chord instead of having a constant thickness. Since the second natural bending frequency cannot be measured, more research can be done whether the natural bending frequency can be lowered by adding a tip mass. Finally, the influence of torsion with respect to the buckling of the model is not included. To more accurately calculate the buckling factor this may be included in the model.

To describe the aeroelastic behaviour of the model, it is highly recommended to calculate the exact position of the elastic axis along the span of the model, and include it in the simulation. Also, it is recommended to research the aerodynamic model in an even more advanced way. The aerodynamic model is of major importance in determining the aeroelastic behaviour of the model and should therefore represent reality as closely as possible. It is also recommended to include three-dimensional effects in this aerodynamic model. This can be done by including wing tip vortices in the model, as well as model the pressure distribution with more accuracy. To model the pressure distribution with more accuracy, the pressure has to be known for a higher number of points along the chord, as well as for a smaller step size in angle of attack. The final step to incorporate the three-dimensional effects is to know the exact position along the span that is described by the two-dimensional model. Next, it is recommended to use a non-linearized model, so that the model can be used for higher deviations and not only for small deflections. Finally, to more accurately determine the response of the system, more research has to be done concerning the structural damping of the model, which is assumed to be negligible in the present implementation.

10.2.3 Actuation

To obtain a first order estimation of the size of the flap, the sizing of the flap is based on statistical method. It is therefore highly recommended to design the flap in more detail. Since the second moment of area is assumed to be constant, and does not vary along the span of the wing, the deflection and thus the size of the flap are less accurate. The sizing is also based on the lift coefficients generated by the Javafoil applet [22]. The accuracy of data generated by this applet is questionable. From these lift coefficients, the lift on the flap is estimated. This is considered to be the only force acting on the flap. This however, is a very first order approximation and a CFD analysis is required to compute the effects of the flow, and thus the forces on the flap, more accurately.

The angle of twist is computed using a torsional constant based on the assumption that the cross-section is a hollow rectangle, which leads to an inaccuracy of the angle of twist. Numerical software should be used to calculate the torsional constant of the cross-section of the model. Furthermore, the mechanism inside the model has been described very conceptually and no dimensions nor computations are performed for this mechanism. It is highly recommended to investigate this mechanism in more detail for further research.

The cut out resulting from the implementation of the flap has an influence on the bending and torsional stiffness of the model. This might result in a need for additional reinforcements at the location of the flap. In addition to this, the flap will affect the natural frequencies of the model. This will have to be considered carefully when designing the flap in more detail.

10.2.4 Measurement Techniques

It has been established that PSP is susceptible to many different sources of error. First, and most important, errors stemming from temperature sensitivity have been mentioned. It would be extremely useful to investigate the temperature changes across the model, and correct for aberrations they would cause in pressure measurements. To do this, an analytical model of the model surface temperature could be set up, resulting in corrections for the measurements. Alternatively, the temperature sensitivity could be counteracted by implementing a temperature sensitive luminophore in the experiment, along with a pressure sensitive one, and by altering the calibration accordingly.

Second, uncertainty is introduced in the experiment by using carbon dioxide particles for PIV. It is recommended to investigate their consequences on the boundary conditions, flow speed and flow uniformity. Alternatively, the repeatability of the experiment should be demonstrated. This would allow for the flow and pressure measurements to be conducted separately, and remove the uncertainty introduced by the carbon dioxide particles altogether.

Lastly, since the software package chosen for the analysis of PSP measurements does not include an integrated VMD module, it is recommended to investigate the connection between the PSP and the VMD software. Alternatively, another PSP software package should be chosen, such as the one used in [3], which includes a VMD module. It is not recommended however to develop a new data analysis solution, since this would reach far beyond the budget of the experiment.

10.2.5 Experiment Set-up

As of now, the experiment features measurement techniques to obtain flow measurements, deformation measurements and pressure measurements over the top surface of the model. For different FSI solvers, different data may be valued higher than what is provided now. Although it has not specifically been mentioned, the chosen model allows for some flexibility regarding the validation data to be obtained.

For example, one may be interested in the pressure distribution over the top and bottom surface to obtain the lift coefficient of the model. This can be achieved in two ways with the model. The first option is to operate the experiment at negative angles of attack, such that the top surface acts as the bottom surface with respect to the flow. This is possible, since the airfoil is symmetric. If the data from two measurement runs are combined, a pressure distribution over the whole model can be made. The other option is to install pressure transducers also in the bottom skin of the model. If another camera is placed to measure the bottom surface, the pressure distribution could actually be coupled in the same experiment. However, one must note that the pressure transducers cannot be placed at the same locations on the top surface as on the bottom surface, due to the limited space. Since the pressure transducers are used for calibration only, different locations of the pressure transducers do not affect the results.

Another variation on the current experiment set-up would be to measure the flow field in more detail. This could be done by adding cameras to measure the flow below the model as well as above the model. Also, if a specific area of the flow is of particular interest, tomographic PIV could be used to obtain a three-dimensional volume of flow vectors, instead of just a plane.

10.2.6 Manufacturing

Since the aeroelastic behaviour of the model is highly dependent on the exact structural parameters, it is important to manufacture the model with high accuracy. Before manufacturing the model, it is highly recommended to research all the manufacturing techniques into more detail together with their tolerances. Besides producing the model, it also has to be assembled. Therefore, it is also highly recommended to do more research into the bonding and assembling of the model and the tolerances that can be achieved during the assembly process.

Appendix A — Workload Distribution

Table A.1: Workload distribution table

Task	**Responsible(s)**
Summary	Raphaël
Acknowledgements	Martin
Preface	Benjamin
Nomenclature	Dirk
Introduction	
Intro	Raphaël
Aeroelasticity	Stefan
Transonic Effects	Raphaël
FSI Solvers	Raphaël
Validation data	
Level Zero Validation Data	Alex, Martin
Level One Validation Data	Alex, Martin
Design approach	Raphaël
Experiment Requirements	Dirk
Wind Tunnel	
Wind Tunnel choices	Raphaël
TST-27 Description	Virgílio
Reynolds Number Calculation	Dirk
Model	
Airfoil	Virgílio
Model Planform	
Length	Virgílio
Chord	Virgílio
Sweep	Virgílio
Taper	Virgílio
Structures and Materials	
Design Space Set-up	Alex, Dirk, Virgílio
Flutter Boundary	Alex, Remco, Virgílio
Natural Frequencies	Martin, Virgílio
Buckling	Martin, Virgílio
Stress Failure	Martin, Virgílio
Material Processing and Properties	Benjamin
Aeroelastic Model	
Theory	Alex, Remco
Model Response	Alex, Remco
Structure-Aeroelasticity Interference	Alex, Remco
Final Design	Virgílio
Mount	

Continued on next page

Table A.1 – continued from previous page

Task	Responsible(s)
Mount Options	Dirk
Mount Trade-Off	Dirk
Detailed Design	Dirk
Actuation	
Actuation Choices	
Important considerations	Raphaël
Flap	Niels
Deforming Bar	Niels
Rotating Clamp	Niels
Torsional Rod	Niels
Wing Integrated Excitation Mechanism	Niels
Gear Option	Dirk, Niels
Excitation of Flow Ahead of Model	Raphaël
Selection of Actuation System	Niels
Detailed Design	
Sizing of the Flap	Niels
Flap Mechanism	Niels
Measurement Techniques	
Measurement Techniques Options	Max, Stefan
Flow Measurements	Max
Deformation	Max
Pressure	Stefan
Particle Image Velocimetry Set-up	Max
Videogrammetric Model Deformation Set-up	Max
Pressure Sensitive Paint Set-up	Stefan
Measurement Techniques Integration	Stefan
Experiment Set-up	
Model Production	Benjamin
Measurement Campaign	Raphaël
Performance and Sensitivity Analysis	
Model	
Aerodynamic Response	Alex
Aeroelastic Behaviour	Alex, Remco
Structure-aeroelasticity Sensitivity Analysis	Remco, Martin
Measurement Devices	
Particle Image Velocimetry	Max
Videogrammetric Model Deformation	Max
Pressure Sensitive Painting	Stefan
Compliance	
Requirements	Dirk
Validation data	Alex
Cost and Risk Analysis	
Cost Analysis	Benjamin, Stefan
Risk Analysis	
Validation Risks	Raphaël
Model Risks	Virgílio
Aeroelastic Risks	Remco
Mount Risks	Virgílio
Actuation Risks	Niels

Continued on next page

Table A.1 – continued from previous page

Task	Responsible(s)
Measurement Techniques Risks	Max
Conclusions and Recommendations	
Conclusion	Martin
Recommendations	
Wind Tunnel	Remco
Model	Remco
Actuation	Niels, Remco
Measurement Techniques	Max, Stefan
Experiment Set-up	Max
Manufacturing	Remco
Appendices	
Workload Distribution	Niels
Model Planform	Dirk
Functional Flow Diagram	Remco
Function Breakdown Structure	Remco
Time Planning	Virgílio

Appendix B — Model Planform

This appendix contains a visualization of the model planform. The technical drawing contains a view of the model cross-section, including the skin thickness. Secondly there is a top/bottom view of the model, containing the chord and the span of the model. The right view looks at the model from the trailing edge and shows the thickness of the wing. It can also bee seen that the airfoil is symmetrical. Finally, there is an isometric view showing the entire model. The drawing only shows the lay-out of the model, without the closed tip section or the mount. The drawing is on a scale of 1:2 and is shown on the next page.

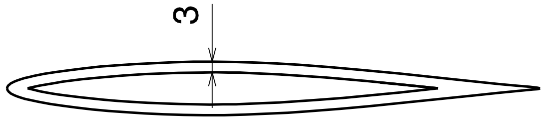

Front view

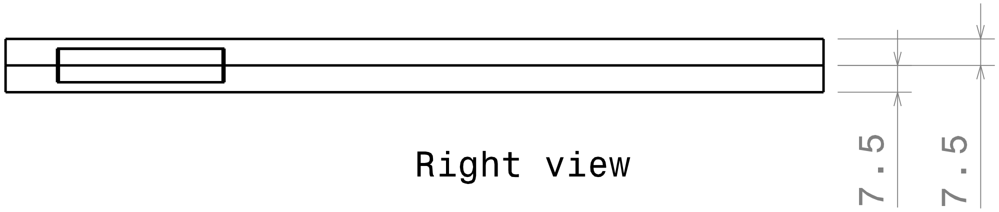

Right view

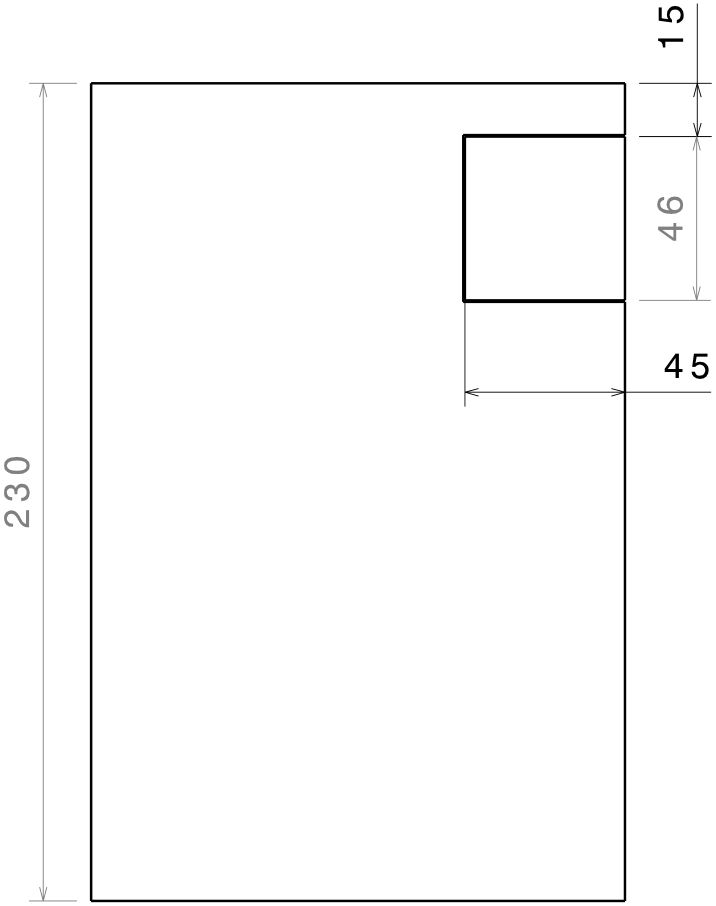

Bottom view

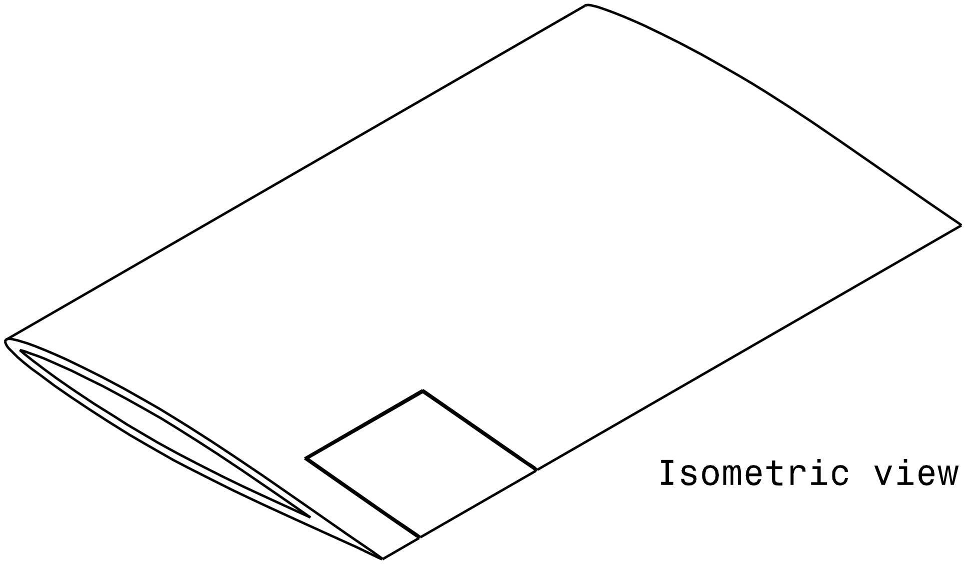

Isometric view

DESIGNED BY:
Dirk
DATE:
24/06/2013
CHECKED BY:
Virgilio
DATE:
24/06/2013

Model Planform

SIZE
A4

T-FLEX

SCALE
1:2
WEIGHT (kg)
0.409
DRAWING NUMBER
1
SHEET
1/1

Appendix C — Functional Flow Diagram

The FFD is meant to show the layout of the entire experiment as individual functions, with each of the functions ordered chronologically into several layers. The layout for the FFD for the T-FLEX experiment is shown in Figure C.1. Each individual function is explained below.

Design T-FLEX Wing The first step in the T-FLEX wing project is to design it. The preliminary design is described in this report.

Manufacture Model The second step is manufacturing the model. The manufacturing of the model has a direct relation to the performance and response of the model. Therefore this process must be performed with great accuracy and the tolerances must be met as specified.

Assemble Model After the model is manufactured, the model has to be assembled. Again, the assembling of the model has to be performed with high accuracy and must be performed within the specified tolerances.

Install Measurement Equipment The installation of the measurement equipment is assumed to occur before mounting the model in the wind tunnel. All the measurement equipment needs to be verified before installing them in the model.

Mount model in the Wind Tunnel The next step is placing the model in the wind tunnel. The mount clamps the wing into its position and at the same time fixes it to the wall of the wind tunnel.

Calibrate the Experiment The calibration of the experiment consists of finding the difference between current measurements and the actual information recorded. This is to ensure the accuracy of the measurements. Calibrating the experiment has several subfunctions. The first of these is setting the model into a position in which the measurement results are known. Then the wind tunnel is run and the measurements are taken, in the same way as during a normal measurement. Next, the measured data is compared to the known data. In case these two data sets are similar, the experiment can go on to the next step. In case the measured data is not satisfactory, the equipment needs to be calibrated. In which way this is done depends on which data does not match. The equipment calibration, at this point in the design process, consists of accounting for aliasing, ensuring equipment integrity, and modifying equipment settings such that the current measurements match the known measurements.

Perform the Experiment The experiment performance begins with setting the model position as desired, similarly to the calibration function. Then the wind tunnel is started and the measurements are taken. Two types of measurements are conducted concurrently, namely structural and aerodynamic measurements. The structural measurements consist of oscillation frequency and deformation. The aerodynamic measurements consist of measuring the boundary conditions, the pressure on the surface and the velocities in the flow field sheets. Next, a check is performed whether the recording of all the desired data was successful. If this however is not the case, an iteration is done starting with running the wind tunnel. If the recording of the data was successful, it is checked whether all the measurements that were planned to be performed are done. However, if this is not the case, an iteration is done

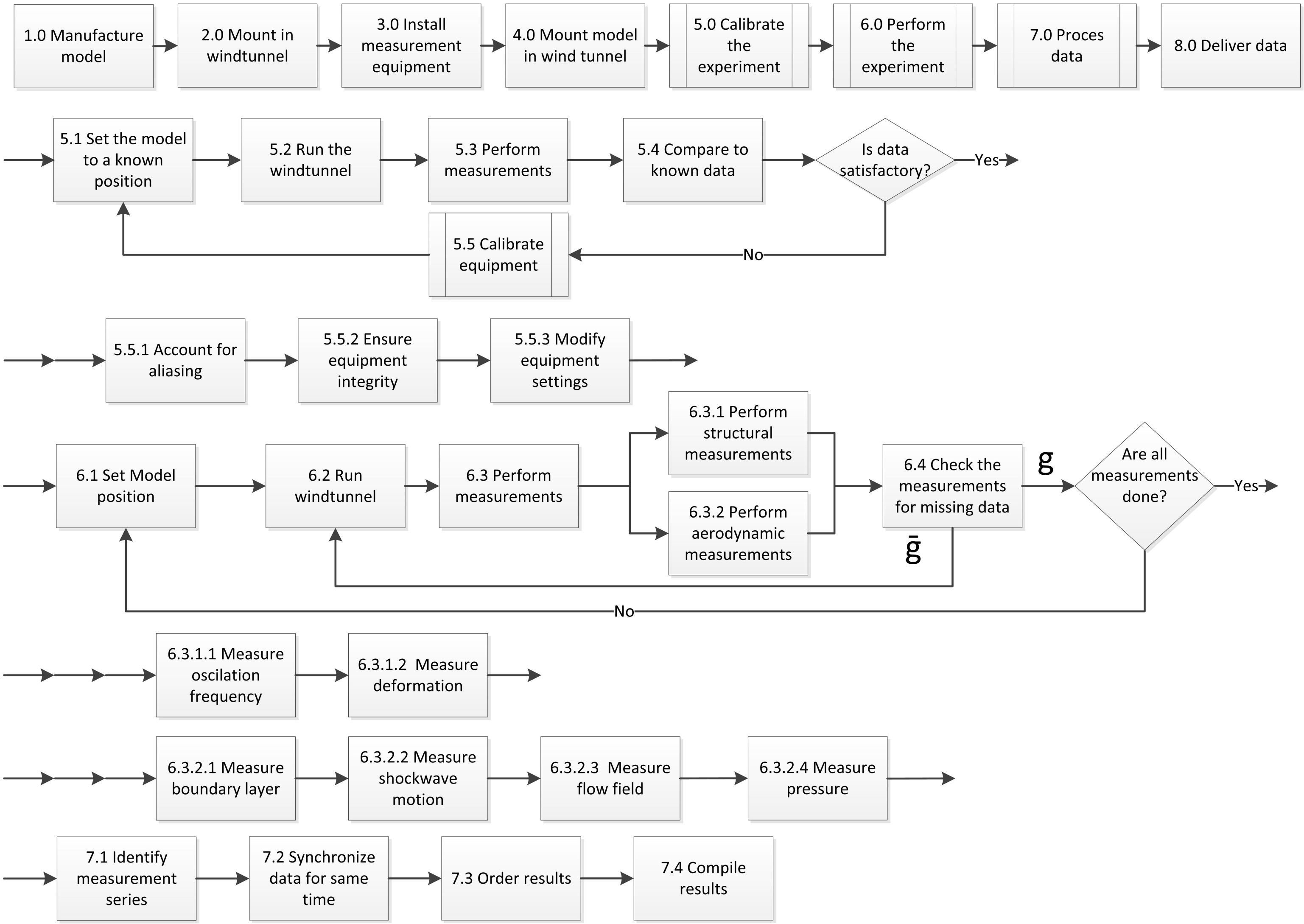

Figure C.1: Functional Flow Diagram

starting with setting the model position. If all the planned measurements are done, the performing of the experiment is done and the next step can be started.

Process the Data Once the experiment has been conducted, the data obtained needs to be processed. First, the data needs to be identified. Then the measurement data of all measurement devices must be synchronized for the same time. Next, the results need to be ordered in a way that is usable for model validation. The last step is compiling all the results so that they are easily available.

Report Data to Customer This last step depends on contacting the customer, whose model can be validated by the obtained measurement data. From here on, all data is provided to the customer and the T-FLEX project is completed.

Appendix D — Functional Breakdown Structure

All of the functions shown in the FFD were explained in Appendix C. The functional break down structure (FBS) in Figure D.1 shows the same functions as the FFD, grouped in categories as opposed to chronological grouping. The second until fifth functions in Figure C.1 are grouped in the category ”Prepare experiment” in Figure D.1. Moreover, in the functional breakdown structure at the end of each main function, a check is performed whether this function meet its requirements. Finally, if all checks are performed and meet the requirements, the data is reported to the customer.

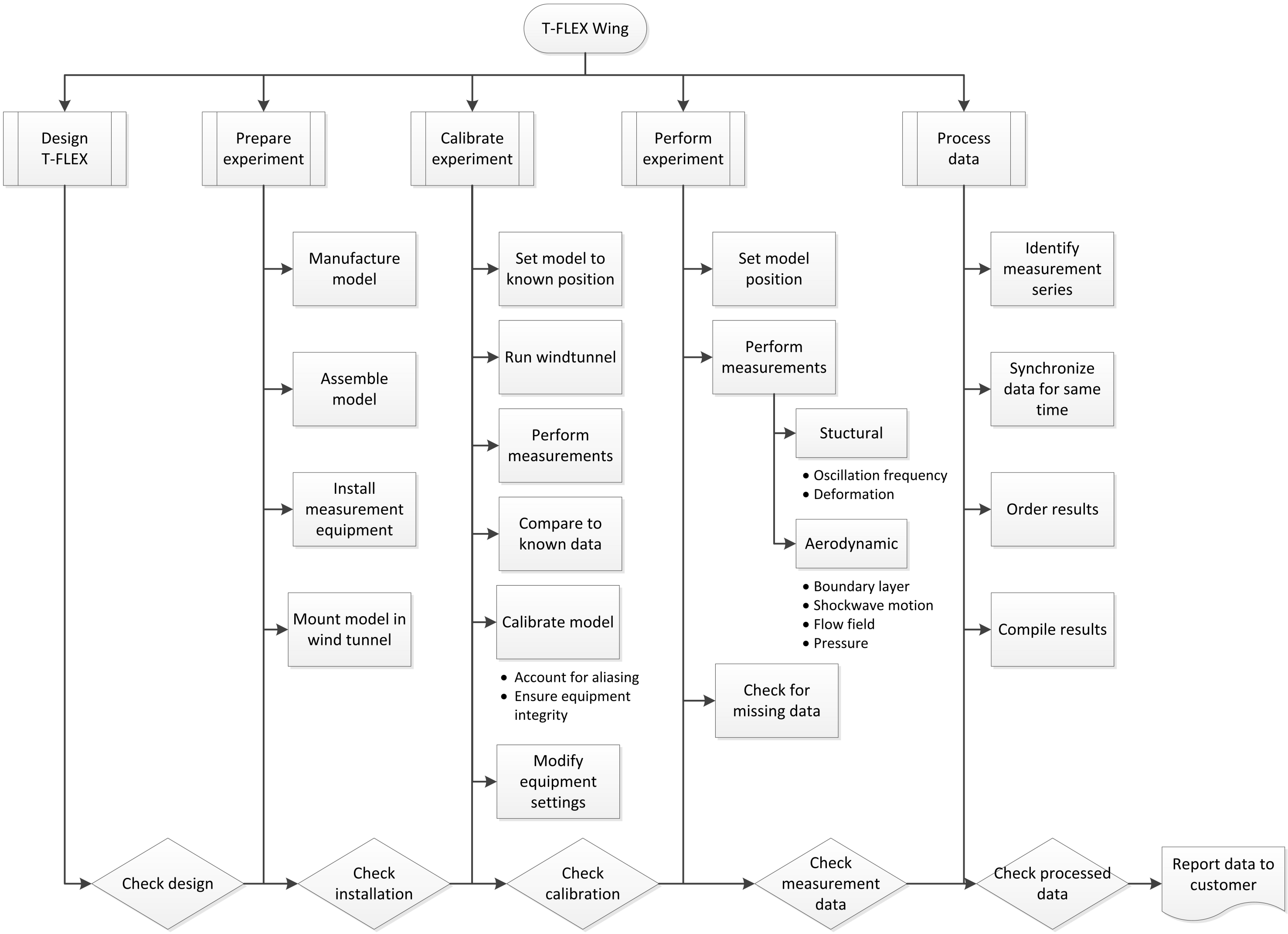

Figure D.1: Functional Breakdown structure

Appendix E — Time Planning

The time planning of the project is defined and maintained by means of a Gantt Chart, which is shown on the following two pages. It contains an overview of the process that lead to the final design contained in this report.

The first point of the Gantt chart are the project completion milestones, listed under Reporting and Deliverables along with their respective deadlines. This is followed by the Planning of the activities performed.

The first stage of the planned project work consists of the Team Organization and the Project Organization. Then, the initial Functional and Requirement Analysis of the project were performed. At this stage the first milestone, the Project Plan, was completed. This was followed by an extensive literature survey, listed under Research. Once that was completed, the Conceptual Design phase was started. The second milestone, the Baseline Report, was completed during this phase, after the Design Option Tree was completed. Once the conceptual design was finished and the options were traded off, the third milestone, the Midterm Report was completed. Then, the final phase was started: the Detailed Design. This phase extends over four weeks, and culminates in the fourth milestone, the Final Report corresponding to this document. Once this is completed the technical work is finished. The final three milestones correspond to the presentation of the work. The Project Logbook describes the work performed by the team members on a daily basis. The Final Presentation and the Symposium are formal presentations where the technical results of the project are displayed.

ID	Task Name	Duration	Start	Finish	Deadline	Predecesso
0	**DSE-T-Flex**	**55 days**	**Mon 22-4-13**	**Fri 5-7-13**	**NA**	
1	**Reporting and Deliverables**	**51 days**	**Wed 24-4-13**	**Thu 4-7-13**	**NA**	
2	Project Plan	0 days	Fri 26-4-13	Fri 26-4-13	Fri 26-4-13	19
3	Baseline Report	0 days	Mon 6-5-13	Mon 6-5-13	Mon 6-5-13	41
4	Midterm Report	0 days	Wed 29-5-13	Wed 29-5-13	Wed 29-5-13	38
5	Final Report	0 days	Wed 26-6-13	Wed 26-6-13	Wed 26-6-13	51
6	Project Logbook	46 days	Wed 24-4-13	Wed 26-6-13	Wed 26-6-13	
7	Final Presentation	0 days	Thu 27-6-13	Thu 27-6-13	Fri 28-6-13	86
8	Symposium	0 days	Thu 4-7-13	Thu 4-7-13	NA	85;88
9	**Planning**	**48 days**	**Mon 22-4-13**	**Wed 26-6-13**	**NA**	
10	**Organization**	**3 days**	**Mon 22-4-13**	**Wed 24-4-13**	**NA**	
11	**Team Organization**	**1,38 days**	**Mon 22-4-13**	**Tue 23-4-13**	**NA**	
12	Produce Organizational Breakdown Structure	2 hrs	Mon 22-4-13	Mon 22-4-13	NA	
13	Generate Communication Diagram	1 hr	Tue 23-4-13	Tue 23-4-13	NA	12
14	Alloocate Human Resources	2 hrs	Tue 23-4-13	Tue 23-4-13	NA	13
15	**Project Organization**	**3 days**	**Mon 22-4-13**	**Wed 24-4-13**	**NA**	
16	Generate Objective and Mission Need Statements	1 hr	Mon 22-4-13	Mon 22-4-13	NA	
17	Generate Work Flow Diagram and Breakdown Structure	4 hrs	Tue 23-4-13	Tue 23-4-13	NA	16
18	Define Work Packages	1 hr	Tue 23-4-13	Tue 23-4-13	NA	17
19	Produce Gantt Chart	4 hrs	Wed 24-4-13	Wed 24-4-13	Wed 24-4-13	18
20	Analyze Project Risk	1 hr	Wed 24-4-13	Wed 24-4-13	NA	
21	Plan Contingency Management	1 hr	Wed 24-4-13	Wed 24-4-13	NA	20
22	Allocate Resources and Budget	1 hr	Wed 24-4-13	Wed 24-4-13	NA	
23	**Functions and Requirements**	**47 days**	**Tue 23-4-13**	**Wed 26-6-13**	**NA**	
24	**Functional analysis**	**1,13 days**	**Tue 23-4-13**	**Wed 24-4-13**	**NA**	
25	Generate Functional Flow Diagram	2 hrs	Tue 23-4-13	Tue 23-4-13	NA	
26	Generate Functional Breakdown Structure	1 hr	Wed 24-4-13	Wed 24-4-13	NA	25
27	**Requirement Analysis**	**45 days**	**Thu 25-4-13**	**Wed 26-6-13**	**NA**	
28	Generate Requirement Discovery Tree	8 hrs	Thu 25-4-13	Thu 25-4-13	NA	32;26
29	Verify Requirements	4 hrs	Fri 26-4-13	Fri 26-4-13	NA	28
30	Update Requirements	45 days	Thu 25-4-13	Wed 26-6-13	NA	
31	**Research**	**1 day**	**Wed 24-4-13**	**Wed 24-4-13**	**NA**	
32	**Conduct Literature Study**	**1 day**	**Wed 24-4-13**	**Wed 24-4-13**	**NA**	
33	Experiment	8 hrs	Wed 24-4-13	Wed 24-4-13	NA	
34	Model Design	8 hrs	Wed 24-4-13	Wed 24-4-13	NA	
35	Wind tunnel	8 hrs	Wed 24-4-13	Wed 24-4-13	NA	
36	Perform Market Analysis	2 hrs	Wed 24-4-13	Wed 24-4-13	NA	
37	Perform Sustainability Analysis	1 hr	Wed 24-4-13	Wed 24-4-13	NA	
38	**Conceptual Design**	**21 days**	**Fri 26-4-13**	**Fri 24-5-13**	**NA**	
39	Define desired measurements	2 days	Wed 15-5-13	Thu 16-5-13	NA	
40	**Generate Concepts**	**21 days**	**Fri 26-4-13**	**Fri 24-5-13**	**NA**	
41	Produce Design Option tree	2 days	Fri 26-4-13	Wed 1-5-13	Fri 3-5-13	28
42	Research design options	6 days	Wed 8-5-13	Wed 15-5-13	NA	41
43	Combine options into concepts	3 days	Thu 16-5-13	Mon 20-5-13	NA	42
44	Detail concepts	2 days	Tue 21-5-13	Wed 22-5-13	NA	43
45	Analyze concept cost	2 days	Thu 23-5-13	Fri 24-5-13	NA	44
46	Analyze concept risk	2 days	Thu 23-5-13	Fri 24-5-13	NA	44
47	**Trade-offs**	**3 days**	**Tue 21-5-13**	**Thu 23-5-13**	**NA**	
48	Find criteria	1 day	Tue 21-5-13	Tue 21-5-13	NA	
49	Define weighting	1 day	Wed 22-5-13	Wed 22-5-13	NA	48
50	Perform trade-off	1 day	Thu 23-5-13	Thu 23-5-13	NA	49
51	**Detailed design**	**18 days**	**Wed 29-5-13**	**Fri 21-6-13**	**NA**	**38**
52	**Technical design**	**15 days**	**Wed 29-5-13**	**Tue 18-6-13**	**NA**	
53	**Model design**	**15 days**	**Wed 29-5-13**	**Tue 18-6-13**	**NA**	
54	Determine loads on model	2 days	Wed 29-5-13	Thu 30-5-13	NA	
55	Design for aeroelastic behaviour	10 days	Fri 31-5-13	Thu 13-6-13	NA	54
56	Design for failure behaviour	10 days	Fri 31-5-13	Thu 13-6-13	NA	54
57	Choose material	10 days	Fri 31-5-13	Thu 13-6-13	NA	54
58	Design actuation system	5 days	Mon 10-6-13	Fri 14-6-13	NA	

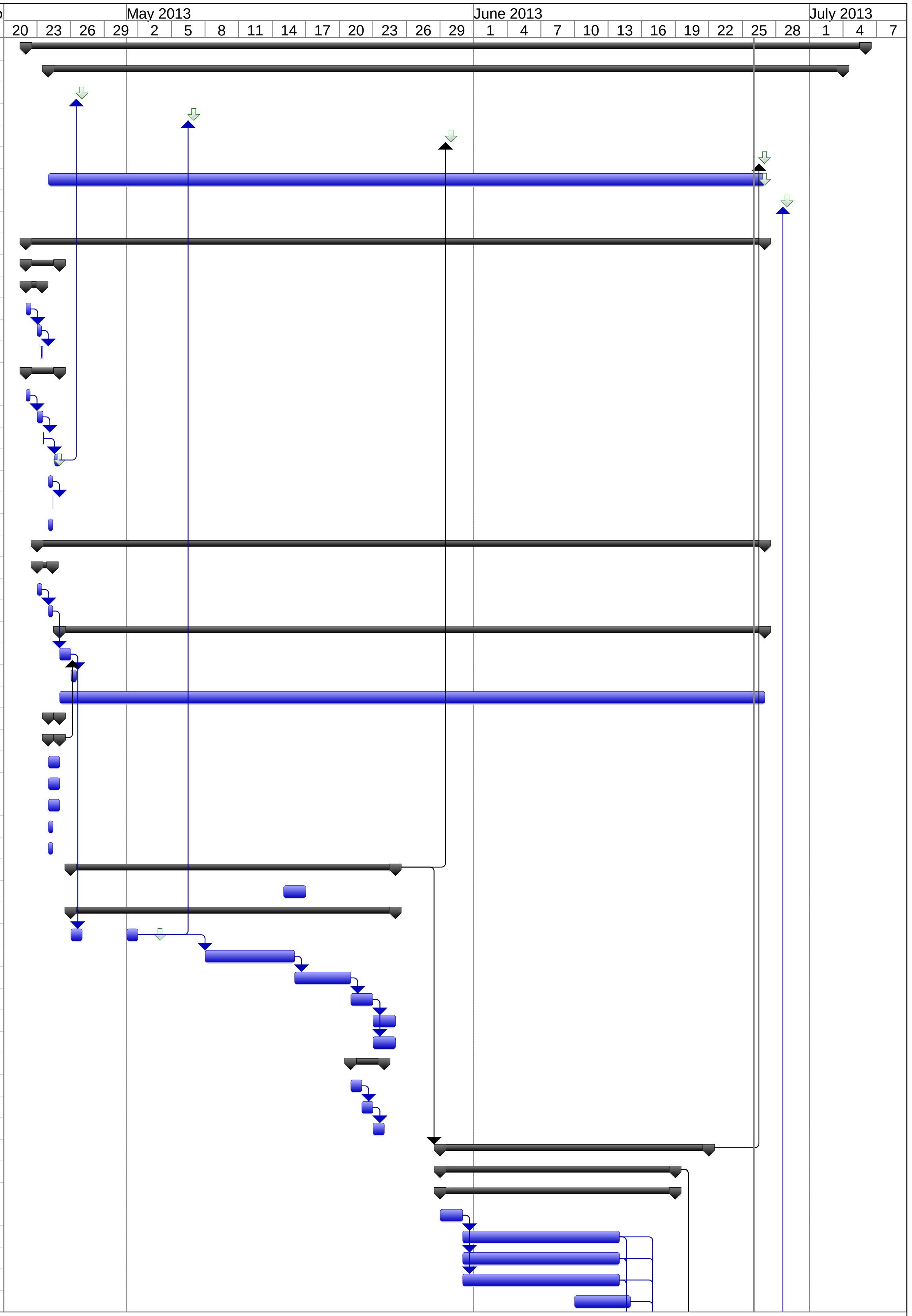

Project: DSE-T-Flex
Date: Wed 26-6-13

Work package ▬ Work package group ▬ Deadline ⇩

ID	Task Name	Duration	Start	Finish	Deadline	Predecesso
59	Elaborate manufacturing plan	1 day	Mon 17-6-13	Mon 17-6-13	NA	56;55;58;57
60	Perform performance analysis	3 days	Fri 14-6-13	Tue 18-6-13	NA	55;56;57
61	Perform sensitivity analysis	3 days	Fri 14-6-13	Tue 18-6-13	NA	55;56;57
62	**Mount design**	**14 days**	**Wed 29-5-13**	**Mon 17-6-13**	**NA**	
63	Detail options	10 days	Wed 29-5-13	Tue 11-6-13	NA	
64	Choose mount	2 days	Wed 12-6-13	Thu 13-6-13	NA	63
65	Define model/mount integration	2 days	Fri 14-6-13	Mon 17-6-13	NA	64
66	**Wind tunnel and measurements**	**15 days**	**Wed 29-5-13**	**Tue 18-6-13**	**NA**	
67	Detail VMD system	8 days	Wed 29-5-13	Fri 7-6-13	NA	
68	Detail PIV system	8 days	Wed 29-5-13	Fri 7-6-13	NA	
69	Detail PSP system	8 days	Wed 29-5-13	Fri 7-6-13	NA	
70	Define/find measurement uncertainties	5 days	Mon 10-6-13	Fri 14-6-13	NA	67;68;69
71	Determine placement/implemention of measurement equipment	5 days	Mon 10-6-13	Fri 14-6-13	NA	67;68;69
72	Perform sensitivity analysis	2 days	Mon 17-6-13	Tue 18-6-13	NA	70;71
73	**Experiment**	**14 days**	**Wed 29-5-13**	**Mon 17-6-13**	**NA**	
74	Detail variables of interest	3 days	Wed 29-5-13	Fri 31-5-13	NA	
75	Detail accuracy and resolution requirements	5 days	Mon 3-6-13	Fri 7-6-13	NA	74
76	Define testing procedure	5 days	Mon 10-6-13	Fri 14-6-13	NA	75
77	Elaborate test plan/manual	1 day	Mon 17-6-13	Mon 17-6-13	NA	76
78	Perform risk analysis	3 days	Wed 19-6-13	Fri 21-6-13	NA	52
79	Perform cost analysis	3 days	Wed 19-6-13	Fri 21-6-13	NA	52
80	Perform verification and validation	3 days	Wed 19-6-13	Fri 21-6-13	NA	52
81	**Quality Assurance**	**48 days**	**Mon 22-4-13**	**Wed 26-6-13**	**NA**	
82	Techical Quality	48 days	Mon 22-4-13	Wed 26-6-13	NA	
83	Reporting Quality	48 days	Mon 22-4-13	Wed 26-6-13	NA	
84	**Closure**	**13 days**	**Wed 19-6-13**	**Fri 5-7-13**	**NA**	
85	Design Poster	3 days	Wed 19-6-13	Fri 21-6-13	NA	
86	Prepare Final Presentation	2 days	Wed 26-6-13	Thu 27-6-13	NA	
87	Write Leonardo Times Article	1 day	Fri 5-7-13	Fri 5-7-13	NA	
88	Prepare for Symposium	3 days	Mon 1-7-13	Wed 3-7-13	NA	

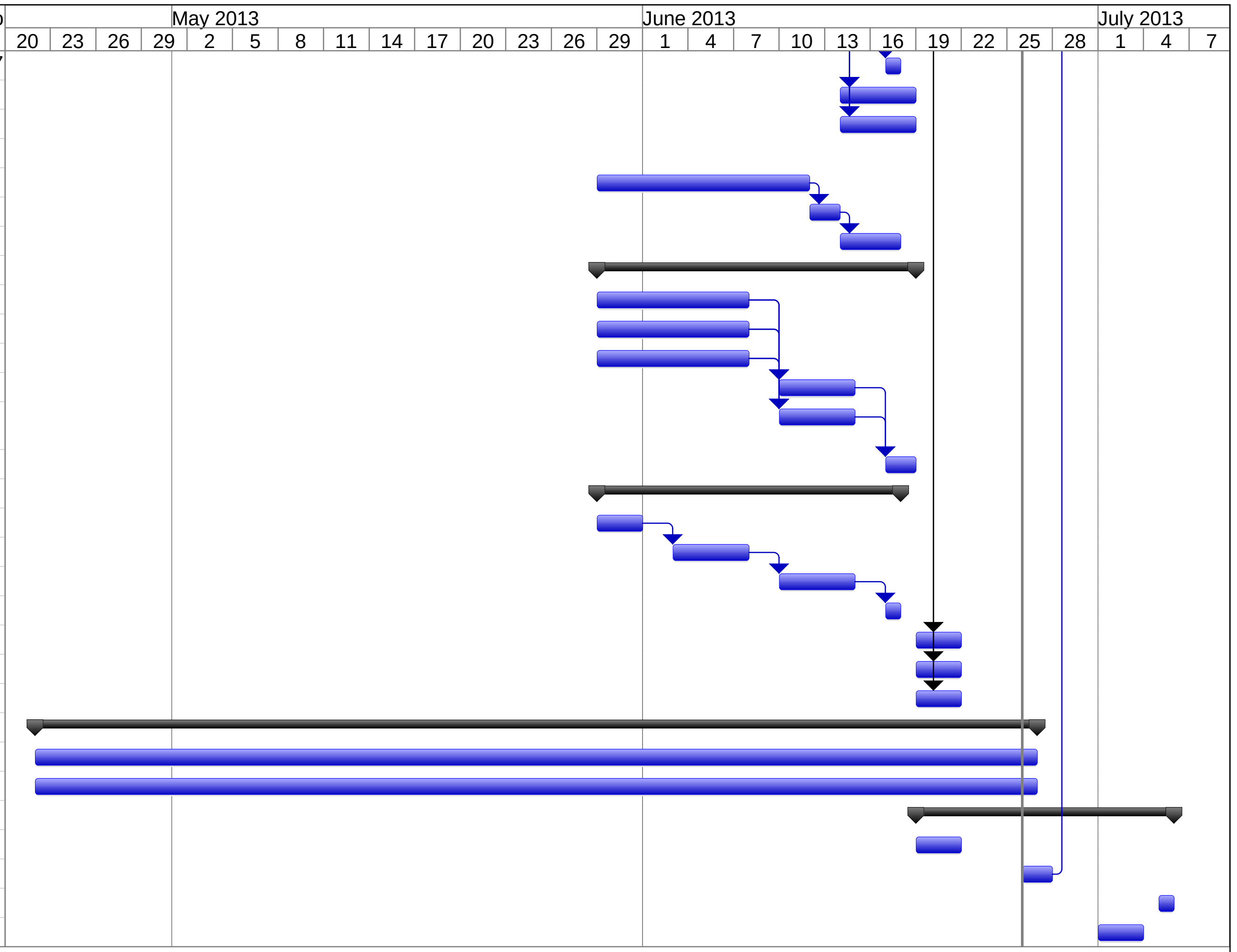

Project: DSE-T-Flex
Date: Wed 26-6-13

Work package ▬ Work package group ▬ Deadline ⇩

Bibliography

[1] D. Abraham, S. Matthews, and R. McIlhagger. A comparison of physical properties of glass fibre epoxy composites produced by wet lay-up with autoclave consolidation and resin transfer moulding. *Composites Part A: Applied Science and Manufacturing*.

[2] E. Baron, J.D.S Danielson, M. Gouterman, J. R. Wan, C.B James, and B. McLachlan. Submillisecond response times of oxygen-quenched luminescent coatings. *Review of Scientific Instruments*, 64(12):3394–3402, 1993.

[3] J.H. Bell and A.W. Burner. Data fusion in wind tunnel testing: Combined pressure paint and model deformation measurements. Technical report, National Aeronautics and Space Administration, June 1998.

[4] J.H. Bell, E.T. Schairer, L.A. Hand, and R.D. Mehta. Surface pressure measurements using luminescent coatings. *Annual Review of Fluid Mechanics*, 33(1):155–206, 2001.

[5] Oddvar O. Bendiksen. Transonic aeroelasticity: Theoretical and computational challenges. In *ICNPAA 2010 World Congress*, 2010.

[6] R.L. Bisplinghoff, H. Ashley, and R.L Halfman. *Aeroelasticity*. Courier Dover Publications, 1996.

[7] A.W. Burner and T. Liu. Videogrammetric model deformation measurement technique. *Journal of Aircraft*, 38(4):745–754, 2001.

[8] A.W. Burner, W.A. Lokos, and D.A. Barrows. In-flight aeroelastic measurement technique development. In *SPIE Proceedings Vol. 5191 Optical Diagnostics for Fluids, Solids, and Combustion II*, pages 186–199, November 2003.

[9] D-Sight. D-Sight Desktop. `http://www.d-sight.com/`, March 2010.

[10] Grantha Design. CES EduPack. `http://www.grantadesign.com/education/edupack2013.htm`, 2013. Provided via TU Delft Blackboard.

[11] K.J. Disotell and J.W. Gregory. Measurement of transient acoustic fields using a single-shot pressure-sensitive paint system. *Review of Scientific Instruments*, 82(7), 2011.

[12] Earl H Dowell and Kenneth C Hall. Modeling of fluid-structure interaction. *Annual Review of Fluid Mechanics*, 33(1):445–490, 2001.

[13] Dantec Dynamics. Stereo PIV (2D3C PIV). `http://www.dantecdynamics.com/Default.aspx?ID=657`. [Online; accessed 07-June-2013].

[14] G.E. Elsinga, B. Wieneke, F. Scarano, and A. Schröder. Tomographic 3D-PIV and applications. *Applied Physics*, 112:103–125, 2008.

[15] R.H. Engler. *Description and assessment of a new optical pressure measurement system (OPMS) demonstrated in the high speed wind tunnel of DLR in Göttingen: 5 tables*. Forschungsbericht. Wiss. Berichtswesen der DLR, 1992.

[16] S. Fang, K. J. Disotell, S.R. Long, and J.W. Gregory. Application of fast-responding pressure-sensitive paint to a hemispherical dome in unsteady transonic flow. *Experiments in fluids*, 50(6):1495–1505, 2011.

[17] G.A. Fleming, H.L. Soto, B.W. South, and S.M. Bartram. Advances in projection moiré interferometry development for large wind tunnel applications. *SAE Technical Paper 1999-01-5598*, 1999.

[18] J.P. Florance, P. Chwalowski, and C.D. Wieseman. Aeroelasticity benchmark assessment. Technical report, NASA Langley Research Center, 2010.

[19] Dietz G., Schewe G., and Mai H. Amplification and amplitude limitation of heave/pitch limit cycle oscillations close to the transonic dip. *Journal of Fluid and Structures 22*, 2006.

[20] C. Gao, S. Luo, S. Niu, K. Qu, , H.S Tang, and Z. Zhang. Determination of transonic wind tunnel geometry and studies on wall interference by numerical simulation. In *50th AIAA Aerospace Sciences Meeting, including the New Horizons Forum and Aerospace Exposition*. American Institute of Aeronautics and Astronautics, 2012.

[21] J.W. Gregory, K. Asai, M. Kameda, T. Liu, and J.P. Sullivan. A review of pressure-sensitive paint for high-speed and unsteady aerodynamics. *Proceedings of the Institution of Mechanical Engineers, Part G: Journal of Aerospace Engineering*, 222(2):249–290, 2008.

[22] M. Hepperle. JavaFoil. `http://www.mh-aerotools.de/airfoils/javafoil.htm`, 2008. [Online; accessed 20-May-2013].

[23] R.C. Hibbeler. *Mechanics of Materials*. Prentice Hall, 7th edition, 2011.

[24] K. Hoffmann. *An Introduction to Measurements using Strain Gages*. Hottinger Baldwin Messtechnik GmbH, 1989.

[25] R.S. Hughes.

[26] UL IDES. PrimoSpire PR-351 Data Sheet. `http://plastics.ides.com/datasheet/e135274/primospire-pr-351`, June 2013. "[Online; accessed 14-June-2013]".

[27] Innovative Schientific Solutions Inc. Planar doppler velocimetry. `http://www.psp-tsp.com/index.php?id=167`, 2010. [Online; accessed 06-June-2013].

[28] K. Isogai. Transonic flutter/divergence characteristics of aeroelastically tailored and non-tailored high-aspect-ratio forward-swept wings. *Journal of Fluids and Structures*, 6:525–537, 1992.

[29] H. Janoch. *Actuators Basics and Applications*. Springer-Verlag Berlin Heidelberg, 2004.

[30] G.L. Crouse Jr. and J.G. Leisman. Transonic aeroelasticity analysis using state-space unsteady aerodynamic modeling. *Journal of Aircraft*, 29:153–160, 1992.

[31] S. Koike, J. Osawa, K. Nakakita, H. Kato, and M. Kameda. Simultaneous pressure and velocity field measurement of pseudo-shock-wave using PSP and PIV. In *AIAA Aerospace Sciences Meeting including the New Horizons Forum and Aerospace Exposition*, 2012.

[32] H. Korsch, Dafnis A., and H.-G. Reimerdes. Dynamic qualification of the HIRENASD elastic wing model. *Aerospace Science and Technology*, 13:130–138, 2009.

[33] D.J. Kuik. Tomographic PIV investigation of a turbulent boundary layer. Master's thesis, Delft University of Technology, January 2007.

[34] J. Leishman and G.L. Crouse Jr. A state-space model of unsteady aerodynamics in a compressible flow for flutter analysis. *AIAA89-0022*, 1989.

[35] R. Lenz and D. Fritsch. Accuracy of videogrammetry with CCD sensors. *ISPRS Journal of Photogrammetry and Remote Sensing*, 45:90–110, 1990.

[36] B.T. Love. Particle size control for PIV seeding using dry ice. Master's thesis, Air Force Institute of Technology, March 2010.

[37] J.E.J Maseland, M. Laban, H. van der Ven, and J.W. Kooi. Development of CFD-based interference models for the DNW-HST transonic wind tunnel. Technical Report NLR-TP-2006-504, National Aerospace Laboratory NLR, 2007.

[38] S.K. Mazumdar. *Composites Manufacturing*. CRC Press, 2001.

[39] B.G. McLachlan and J.H. Bell. Pressure-sensitive paint in aerodynamic testing. *Experimental Thermal and Fluid Science*, 10(4):470 – 485, 1995.

[40] T.H.G. Megson. *Aircraft Structures for Engineering Students*. Elsevier Aerospace Engineering Series. Butterworth-Heinemann, 4th edition, 2007.

[41] H.M. Merklinger. Scheimpflug's patent. `http://www.trenholm.org/hmmerk/SHSPAT.pdf`. [Online; accessed 12-June-2013].

[42] Micro-Measurements. *Strain Gage Selection: Criteria, Procedures, Recommendations*. Vishay Precision Group.

[43] M. J. Morris, M. Sajben, and J. C. Kroutil. Experimental investigation of normal-shock/turbulent-boundary-layer interactions with and without mass removal. *AIAA Journal*, 30:359–366, 1992.

[44] J.J. Muncey and D.M. Pote. Design and construction of wind tunnel models. Technical Report 20, North Atlantic Treaty Organization Advisory Group for Aeronautical Research and Development, Rome, Italy, February 1956.

[45] J. Murphy. *Reinforced Plastics Handbook*. Elsevier Science, 1998.

[46] K. Nakakita and K. Asai. Pressure-sensitive paint application to a wing-body model in a hypersonic shock tunnel. In *22nd AIAA Aerodynamic Measurement Technology and Ground Testing Conference*, 2002.

[47] K. Nakakita, M. Kurita, and K. Mitsuo. Development of the pressure-sensitive paint measurement for large wind tunnels at japan aerospace exploration agency. In *24th Congress of the International Council of the Aeronautical Sciences*, 2004.

[48] M.C.H. Niu. *Airframe Structural Design*. Conmili Press, 1988.

[49] DLR Institute of Aerodynamics and Flow Technology. Image Pattern Correlation Technique (IPCT). `http://www.dlr.de/as/en/desktopdefault.aspx/tabid-183/251_read-13861/`. [Online; accessed 21-June-2013].

[50] DLR Institute of Aerodynamics and Flow Technology. Particle Image Velocimetry (PIV). `http://www.dlr.de/as/en/desktopdefault.aspx/tabid-183/251_read-12796/`. [Online; accessed 07-June-2013].

[51] DLR Institute of Propulsion Technology. DGV - Doppler Global Velocimetry. `http://www.dlr.de/at/en/desktopdefault.aspx/tabid-1657/2281_read-3723/`. [Online; accessed 06-June-2013].

[52] DLR Institute of Propulsion Technology. DGV system specifications. `http://www.dlr.de/at/en/DesktopDefault.aspx/tabid-1657/2281_read-4574/`. [Online; accessed 06-June-2013].

[53] Omega. Introduction to stepper motors and drives. `http://www.omega.com/prodinfo/stepper_motors.html`, 2013. [Online; accessed 14-June-2013].

[54] K. Patorski. Handbook of the moiré fringe technique. *Elsevier Science Publishers*, pages 372–373, 1993.

[55] Photron. FASTCAM SA1.1 Ultra High Video System. `http://www.photron.com/datasheet/Fastcam_SA1_Datasheet.pdf`, 2013. [Online; Accessed 11-06-2013].

[56] Physikinstrumente. Piezo bender actuators. `http://www.physikinstrumente.com/en/products/prdetail.php?sortnr=101780`, 2013. [Online; accessed 17-June-2013].

[57] A. Pizzi and K.L Mittal. *Handbook of Adhesive Technology*. Marcel Dekker, Inc., 2003.

[58] Modern Plastics. TECAMAX SRP. `http://www.modernplastics.com/april05/wdtecamax.html`, June 2013. "[Online; accessed 14-June-2013]".

[59] A.K. Prasad. Particle image velocimetry. *Current Science*, 79(1):51–60, 2000.

[60] M. Raffel, C.E. Willert, S.T. Wereley, and J. Kompenhans. *Particle Image Velocimetry*. Springer, 2 edition, 2007.

[61] B.C. Ray. Freeze-thaw response of glass-polyester composites at different loading rates. *Journal of Reinforced Plastics and Composites*, 2005.

[62] D.P. Raymer. *Aircraft Design: A Conceptual Approach*. American Institute of Aeronautics and Astronautics, Inc., 2nd edition, 1992.

[63] M.F. Reeder, J. W. Crafton, J. Estevadeordal, J. DeLapp, C. McNiel, D. Peltier, and T. Reynolds. Clean seeding for flow visualization and velocimetry measurements. *Experiments in fluids*, 48(5):889–900, 2010.

[64] H. Sakaue, T. Kakisako, and H. Ishikawa. Characterization and optimization of polymer-ceramic pressure-sensitive paint by controlling polymer content. *Sensors*, 11(7):6967–6977, 2011.

[65] H. Sakaue and J.P. Sullivan. Fast response time characteristics of anodized aluminum pressure sensitive paint. *AIAA paper*, 506:2000, 2000.

[66] F.J.J. Schrijer. *Compressible aerodynamics: Aerodynamics II (AE2110)*. Delft University of Technology, April 2011.

[67] R.C. Scott, S.T. Hoadley, C.D. Wieseman, and M.H. Durham. The benchmark active controls technology model: Aerodynamic data. Technical report, 1997.

[68] A.M. Scroggin, E.B. Slamovich, J.W. Crafton, N. Lachendro, and J.P. Sullivan. Porous polymer/ceramic composites for luminescence-based temperature and pressure measurement. In *MRS Proceedings*, volume 560, page 347. Cambridge Univ Press, 1999.

[69] W.A. Silva, T.W. Strganac, C.D. Wieseman, and M.R. Hajj. Higher-order spectral analysis of a nonlinear pitch and plunge apparatus. In *46th AIAA/ASME/ASCE/AHS/ASC Structures, Structural Dynamics and Materials Conference*.

[70] L. S. Stivers, Jr. Effects of subsonic Mach number on the forces and pressure distributions on four NACA 64A-series airfoil sections at angles of attack as high as 28°. Technical Report 3162, National Advisory Committee for Aeronautics, 1954.

[71] T. Sugimoto, S. Kitashima, D. Numata, H.Nagai, and K. Asai. Characterization of frequency response of pressure-sensitive paints. In *50th AIAA Aerospace Sciences Meeting including the New Horizons Forum and Aerospace Exposition*, 2012.

[72] J.P. Sullivan T. Liu. *Pressure-and Temperature-Sensitive Paints*. Wiley Online Library, 2005.

[73] T. Theodorsen. General theory of aerodynamic instability and the mechanism of flutter. Technical Report 496, National Advisory Committee for Aeronautics.

[74] Transportation Safety Board of Canada. Aircraft investigation report A05F0047. `http://www.tsb.gc.ca/eng/rapports-reports/aviation/2005/a05f0047/a05f0047.pdf`, 2005. [Online; accessed 02 May 2013].

[75] K. Ueda and A. Umeda. Dynamic response of strain gages up to 300kHz. *Experimental Mechanics*, 38:93–98, 1998.

[76] N. van Rijswijk. TST-27 Transonic Control. Technical report, Delft University of Technology, Faculty of Aerospace Engineering, May 2012.

[77] A. van Zuijlen and F. Schrijer. *Project Guide Design Synthesis Exercise, T-FLEX: Transonic flexible wing experiment*. TU Delft, Aerodynamics department, 2013.

[78] T.B. Vorburger, M.J. Mclay, F.E. Scire, D.E. Gilsinn, and C.H.W. Giauque. Surface roughness studies for wind tunnel models used in high reynolds number testing. *Journal of Aircraft*, 23(1):56–61, 1986.

[79] J.R. Wright and J.E. Cooper. *Introduction to Aircraft Aeroelasticity and Loads*. Aerospace Series (PEP). John Wiley & Sons, 2008.

[80] Q. Zhu. Determination of transonic wind tunnel geometry and studies on wall interference by numerical simulation. In *International Conference on Computer Application and System Modeling*. North University of China, Taiyuan, China, 2010.